

NUMERICAL STUDY OF
THE PROCESS PARAMETERS IN
SPARK PLASMA SINTERING (SPS)

By

REDWAN JAHID CHOWDHURY

Bachelor of Science in Mechanical Engineering

Bangladesh University of Engineering and Technology

Dhaka, Bangladesh

2011

Submitted to the Faculty of the
Graduate College of the
Oklahoma State University
in partial fulfillment of
the requirements for
the Degree of
MASTER OF SCIENCE
December, 2013

NUMERICAL STUDY OF
THE PROCESS PARAMETERS IN
SPARK PLASMA SINTERING (SPS)

Thesis Approved:

Dr. Sandip P. Harimkar

Thesis Adviser

Dr. Kaan Kalkan

Dr. Matthew Klopstein

Name: Redwan Jahid Chowdhury

Date of Degree: DECEMBER, 2013

Title of Study: NUMERICAL STUDY OF THE PROCESS PARAMETERS IN SPARK
PLASMA SINTERING (SPS)

Major Field: Mechanical and Aerospace Engineering

Abstract:

Spark plasma sintering (SPS) is one of the most widely used sintering techniques that utilizes pulsed direct current together with uniaxial pressure to consolidate a wide variety of materials. The unique mechanisms of SPS enable it to sinter powder compacts at a lower temperature and in a shorter time than the conventional hot pressing, hot isostatic pressing and vacuum sintering process. One of the limitations of SPS is the presence of temperature gradients inside the sample, which could result in non-uniform physical and microstructural properties. Detailed study of the temperature and current distributions inside the sintered sample is necessary to minimize the temperature gradients and achieve desired properties. In the present study, a coupled thermal-electric model was developed using finite element codes in ABAQUS software to investigate the temperature and current distributions inside the conductive and non-conductive samples. An integrated experimental-numerical methodology was implemented to determine the system contact resistances accurately. The developed sintering model was validated by a series of experiments, which showed good agreements with simulation results. The temperature distribution inside the sample depends on some process parameters such as sample and tool geometry, punch and die position, applied current and thermal insulation around the die. The role of these parameters on sample temperature distribution was systematically analyzed. The findings of this research could prove very useful for the reliable production of large size sintered samples with controlled and tailored properties.

TABLE OF CONTENTS

Chapter	Page
I. INTRODUCTION.....	1
1.1 Introduction.....	1
1.2 Literature review.....	5
1.2.1 Experimental background.....	5
1.2.2 Computational background.....	11
1.3 Scope of this thesis.....	15
II. COUPLED THERMAL-ELECTRIC FINITE ELEMENT MODEL.....	18
2.1 Introduction.....	18
2.2 Finite element modeling details.....	19
2.2.1 Theory.....	19
2.2.2 Model set up.....	20
2.2.3 Contact resistance.....	24
2.3 Experimental procedure.....	27
2.3.1 Contact resistance calibration experiment.....	30
2.3.2 SPS experiment.....	34
2.4 Results and discussion.....	39
2.4.1 Contact resistance calibration for the SPS setup.....	39
2.4.2 Experimental validation of the model.....	50
2.4.3 Temperature and current distribution.....	58
2.5 Conclusion.....	67
III. IMPORTANCE OF THE PROCESS PARAMETERS IN SPS.....	68
3.1 Introduction.....	68
3.2 Method.....	69
3.3 Results and discussion.....	70
3.3.1 Effect of sample diameter.....	70
3.3.2 Effect of sample thickness.....	76
3.3.3 Effect of die thickness.....	83

Chapter	Page
3.3.4 Effect of die height.....	89
3.3.5 Effect of punch length.....	95
3.3.6 Effect of asymmetric punch-die position.....	100
3.3.7 Effect of using unequal punch length.....	107
3.3.8 Effect of input current (set temperature).....	113
3.3.9 Effect of using insulating layer around the die.....	119
3.4 Conclusion.....	125
IV. CONCLUSION.....	127
V. FUTURE WORK.....	130
REFERENCES.....	132
APPENDIX.....	140

LIST OF TABLES

Table No.	Table caption	Page
2.1	Dimensions of all the SPS tools used in the study.....	22
2.2	Single punch simulation system resistance for different guessed horizontal electrical contact conductance.....	41
2.3	Double punch simulation system resistance for different guessed horizontal electrical contact conductance.....	44
2.4	Dummy test simulation system resistance for different guessed vertical electrical contact conductance.....	48
2.5	Simulated die surface temperature for different guessed thermal contact conductances in the dummy test.....	49
2.6	Percentage difference between experimentally measured and simulated temperature at three studied points for three temperatures.....	57
2.7	Average of relative densities of the alumina samples sintered at different temperatures.....	57
3.1	Studied parameters influencing temperature and current distribution.....	70
3.2	System resistance for different die thicknesses.....	88
3.3	System resistance for different die heights.....	94
3.4	System resistance for different punch lengths.....	96

LIST OF FIGURES

Fig. No.	Figure caption	Page
1.1	Schematic of a typical SPS apparatus.....	3
2.1	Schematic of the SPS setup used in the model: (a) 3d view and (b) axisymmetric cut view.....	21
2.2	Change in voltage and temperature through imperfect contacts.....	25
2.3	Spark plasma sintering setup.....	29
2.4	Die-punch-sample assembly inside the furnace of SPS setup.....	29
2.5	Algorithm to determine system contact conductances (or resistances)...	31
2.6	Schematic of the single punch test.....	32
2.7	Schematic of the double punch test.....	33
2.8	Schematic of the dummy test.....	34
2.9	Schematic of the SPS apparatus showing the three points where the thermocouples were positioned.....	36
2.10	Hydraulic press equipment.....	37
2.11	Some of the graphite cylinders used for experimental validation.....	37
2.12	Some of the alumina compacts sintered at 1100° C temperature and under 70 MPa pressure	38
2.13	Mettler Toledo (Delta Range XD204) balance.....	38
2.14	Experimental data from single punch test – 1 st run.....	40

2.15	Experimental data from single punch test – 2 nd run.....	40
2.16	Experimental data from single punch test – 3 rd t run.....	41
2.17	Convergence of simulation system resistance to experimental system resistance in the single punch test.....	42
2.18	Experimental data from double punch test – 1 st run.....	43
2.19	Experimental data from double punch test – 2 nd run.....	43
2.20	Experimental data from double punch test – 3 rd run.....	44
2.21	Convergence of simulation system resistance to experimental system resistance in the double punch test.....	45
2.22	Experimental data from dummy test – 1 st run.....	46
2.23	Experimental data from dummy test – 2 nd run.....	47
2.24	Experimental data from dummy test – 3 rd run.....	47
2.25	Convergence of simulation system resistance to experimental system resistance in the dummy test.....	48
2.26	Convergence of simulated die surface temperature to experimental die surface temperature in the dummy test.....	49
2.27	Experimental and simulated temperature history data for sintering alumina sample at a set temperature of 1100° C on the die surface.....	52
2.28	Comparison between experimental and simulated die surface temperature at point A for the test with graphite cylinder.....	52
2.29	Comparison between experimental and simulated punch surface temperature at point B for the test with graphite cylinder.....	53
2.30	Comparison between experimental and simulated temperature at point C (inside the die, 2mm from sample surface) for the test with graphite cylinder.....	53
2.31	Comparison between experimental and simulated die surface temperature at point A for the test with alumina sample.....	55
2.32	Comparison between experimental and simulated punch surface temperature at point B for the test with alumina sample.....	55

2.33	Comparison between experimental and simulated temperature at point C (inside the die, 2mm from sample surface) for the test with alumina sample.....	56
2.34	Temperature contour plot in the whole SPS system in a 3d view: (a) alumina and (b) copper	59
2.35	Temperature contour plot in the SPS system in an axisymmetric cut view: (a) alumina and (b) copper	60
2.36	ECD contour plot in the SPS system: (a) alumina and (b) copper.....	60
2.37	Heat flux vector distribution in the SPS setup: (a) alumina and (b) copper	61
2.38	Electric potential distribution in the SPS system: (a) alumina and (b) copper	62
2.39	Temperature distribution inside the sample respectively after 1 sec and steady state: (a), (b) alumina and (c), (d) copper	64
2.40	Temperature distribution in alumina and copper: (a) axial and (b) radial direction	65
2.41	(a) Temperature and (b) ECD distribution in sample-die for alumina and copper.....	66
2.42	(a) Temperature and (b) ECD distribution in punch-sample-punch for alumina and copper	66
3.1	Temperature distribution in axial direction in the sample as a function of sample diameter: (a) alumina and (b) copper	73
3.2	Temperature distribution in radial direction in the sample as a function of sample diameter: (a) alumina and (b) copper	73
3.3	Temperature distribution in sample-die as a function of sample diameter: (a) alumina and (b) copper	74
3.4	Electric current density distribution in sample-die as a function of sample diameter: (a) alumina and (b) copper	74
3.5	Temperature distribution in punch-sample-punch as a function of sample diameter: (a) alumina and (b) copper	75
3.6	Electric current density distribution in punch-sample-punch as a	

	function of sample diameter: (a) alumina and (b) copper	75
3.7	Temperature contour plot in samples as a function of sample thickness: (a-c) alumina, and (d-f) copper	79
3.8	Temperature distribution in axial direction in the sample as a function of sample thickness: (a) alumina and (b) copper	80
3.9	Temperature distribution in radial direction in the sample as a function of sample thickness: (a) alumina and (b) copper	80
3.10	Temperature distribution in sample-die as a function of sample thickness: (a) alumina and (b) copper.....	81
3.11	Electric current density distribution in sample-die as a function of sample thickness: (a) alumina and (b) copper	81
3.12	Temperature distribution in punch-sample-punch as a function of sample thickness: (a) alumina and (b) copper	82
3.13	Electric current density distribution in punch-sample-punch as a function of sample thickness: (a) alumina and (b) copper	82
3.14	Temperature distribution in axial direction in the sample as a function of die thickness: (a) alumina and (b) copper	85
3.15	Temperature distribution in radial direction in the sample as a function of die thickness: (a) alumina and (b) copper	85
3.16	Temperature distribution in sample-die as a function of die thickness: (a) alumina and (b) copper	86
3.17	Electric current density distribution in sample-die as a function of die thickness: (a) alumina and (b) copper.....	86
3.18	Temperature difference between sample center and die outer surface as a function of die thickness.....	87
3.19	Temperature distribution in punch-sample-punch as a function of die thickness: (a) alumina and (b) copper	87
3.20	Electric current density distribution in punch-sample-punch as a function of die thickness: (a) alumina and (b) copper	88
3.21	Temperature distribution in axial direction in the sample as a function of die height: (a) alumina and (b) copper	91

3.22	Temperature distribution in radial direction in the sample as a function of die height: (a) alumina and (b) copper	91
3.23	Temperature distribution in sample-die as a function of die height: (a) alumina and (b) copper	92
3.24	Electric current density distribution in sample-die as a function of die height: (a) alumina and (b) copper	92
3.25	Temperature difference between sample center and die outer surface as a function of die height.....	93
3.26	Temperature distribution in punch-sample-punch as a function of die height: (a) alumina and (b) copper	93
3.27	Electric current density distribution in punch-sample-punch as a function of die height: (a) alumina and (b) copper	94
3.28	Temperature distribution in axial direction in the sample as a function of punch length: (a) alumina and (b) copper	97
3.29	Temperature distribution in radial direction in the sample as a function of punch length: (a) alumina and (b) copper	97
3.30	Temperature distribution in sample-die as a function of punch length: (a) alumina and (b) copper	98
3.31	Electric current density distribution in sample-die as a function of punch length: (a) alumina and (b) copper	98
3.32	Temperature distribution in punch-sample-punch as a function of punch length: (a) alumina and (b) copper	99
3.33	Electric current density distribution in punch-sample-punch as a function of punch length: (a) alumina and (b) copper	99
3.34	Temperature contour plot in the SPS systems for different die positions: (a-c) alumina, and (d-f) copper	102
3.35	Temperature contour plot of the samples for different die positions: (a-c) alumina, and (d-f) copper	103
3.36	Temperature distribution in axial direction in the sample for different die positions: (a) alumina and (b) copper	104
3.37	Temperature distribution in radial direction in the sample for different	

	die positions: (a) alumina and (b) copper	104
3.38	Temperature difference between the sample top and bottom surfaces as a function of axial shift of die.....	105
3.39	Temperature distribution in sample-die for different die positions: (a) alumina and (b) copper.....	105
3.40	Electric current density distribution in sample-die for different die positions: (a) alumina and (b) copper	106
3.41	Temperature distribution in punch-sample-punch for different die positions: (a) alumina and (b) copper	106
3.42	Electric current density distribution in punch-sample-punch for different die positions: (a) alumina and (b) copper.....	107
3.43	Temperature contour plot in the sample for different lengths of upper punch: (a-c) alumina, and (d-f) copper	109
3.44	Temperature distribution in axial direction in the sample for different lengths of upper punch: (a) alumina and (b) copper	110
3.45	Temperature distribution in radial direction in the sample for different lengths of upper punch: (a) alumina and (b) copper	110
3.46	Temperature distribution in sample-die for different lengths of upper punch: (a) alumina and (b) copper	111
3.47	Electric current density distribution in sample-die for different length of upper punch: (a) alumina and (b) copper.....	111
3.48	Temperature distribution in punch-sample-punch for different lengths of upper punch: (a) alumina and (b) copper.....	112
3.49	Electric current density distribution in punch-sample-punch for different lengths of upper punch: (a) alumina and (b) copper.....	112
3.50	Temperature distribution in axial direction in the sample as a function of input current: (a) alumina and (b) copper	114
3.51	Temperature distribution in radial direction in the sample as a function of input current: (a) alumina and (b) copper	115
3.52	Temperature distribution in sample-die as a function of input current: (a) alumina and (b) copper	115

3.53	Electric current density distribution in sample-die as a function of input current: (a) alumina and (b) copper.....	116
3.54	Temperature distribution in punch-sample-punch as a function of input current: (a) alumina and (b) copper.....	116
3.55	Electric current density distribution in punch-sample-punch as a function of input current: (a) alumina and (b) copper.....	117
3.56	Temperature distribution in the alumina sample as a function of input current (1000 A and 1800 A): (a) axial and (b) radial direction.....	117
3.57	Temperature distribution for the alumina sample as a function of input current (1000 A and 1800 A): (a) sample-die and (b) punch-sample-punch.....	118
3.58	Temperature difference between sample center and sample edge for different input currents.....	118
3.59	Temperature difference between sample center and die outer surface for different input currents.....	119
3.60	Temperature contour plot in the whole SPS system with insulating layer around the die: (a) alumina and (b) copper	122
3.61	Temperature distribution in axial direction in the sample with and without the insulating layer around the die: (a) alumina and (b) copper.....	122
3.62	Temperature distribution in radial direction in the sample with and without the insulating layer around the die: (a) alumina and (b) copper.....	123
3.63	Temperature distribution in sample-die with and without insulating layer around the die: (a) alumina and (b) copper.....	123
3.64	Electric current density distribution in sample-die with and without the insulating layer around the die: (a) alumina and (b) copper.....	124
3.65	Temperature distribution in punch-sample-punch with and without the insulating layer around the die: (a) alumina and (b) copper.....	124
3.66	Electric current density distribution in punch-sample-punch with and without the insulating layer around the die: (a) alumina and (b) copper...	125

CHAPTER I

INTRODUCTION

1.1 Introduction

Sintering as a material processing method has been used since the ancient times. The Mesopotamians were the first to utilize this method to produce bricks by heating clay bodies in open pit fire way back in 6000 BC [1]. Metals and ceramics were sintered by the Egyptians as early as 3000 BC [2]. Although this manufacturing process has been used for thousands of years, there was hardly any scientific experiment or advancement done to improve this process before 1920. The basic mechanisms of consolidation by mass transport were explored by Frenkel, Kuczynski, Lenel, Coble, Kingery, German, and others in the next few decades [3-5]. Understanding the basic phenomena of sintering led to the activation and development of this process by different means. Electric current was used as one of the ways to activate the sintering process. This idea was developed by Taylor in 1933 for hot pressing of cemented carbides [6]. Subsequent work was done by researchers all over the world, especially in Japan, which led to the development of many current activated sintering techniques. Spark plasma sintering (SPS) is one of the most widely used activated sintering techniques that utilizes pulsed direct current (DC) together with uniaxial pressure to consolidate a wide variety of materials to high density in near net shapes. It has gained great popularity as an alternative to conventional sintering processes such as hot pressing, hot isostatic pressing and vacuum pressing. In these sintering processes, the

powder compact is heated externally by radiation from the furnace, which could take several hours for sintering; resulting in grain coarsening and segregation of phases at grain boundaries. Unlike these processes, there is no external heat source in SPS. High density electric current passing through the spacers, punches, die, and the conductive sample causes intense localized joule heating at the particle contacts. The extremely high heating rate, which could be as high as $1000^{\circ}\text{C}/\text{min}$, enables this process to sinter variety of materials at a relatively short time with significant grain growth control and improved physical, mechanical, and microstructural properties. Restriction of grain growth in SPS makes it a potential method for producing bulk nanocrystalline materials. Moreover, its ability to sinter at lower temperature makes it suitable for fabricating non-equilibrium and metastable phases without unwanted phase transformation [2, 6-11].

The SPS setup is capable of applying extremely high current in the range of 1,000 A to 10,000 A under a high load of 50 kN to 250 kN on the powder sample. The current and load capabilities limit the maximum size of the sample that can be sintered by SPS. Fig. 1.1 shows the schematic of a typical SPS apparatus. It primarily consists of a vertical single-axis pressurization mechanism, specially designed punches and die, and DC-pulse power generator unit. The die and punches are most often made from high purity graphite because of its high thermal and electrical conductivity and outstanding mechanical strength at high temperatures. The sample inside the die is usually in a powder form, which could be a single-phase material undergoing pure densification or mixture of powders undergoing simultaneous synthesis and densification. Large variety of materials ranging from metals, polymers, ceramics, intermetallic compounds to composites have been successfully sintered so far with excellent properties that were unattainable with other processing techniques. The SPS process typically consists of three stages: (a) heating stage when heat and pressure are applied at predefined rate, (b) holding stage when the pressure

and temperature are kept constant; and (c) cooling stage when pressure is taken off and the system is cooled down.

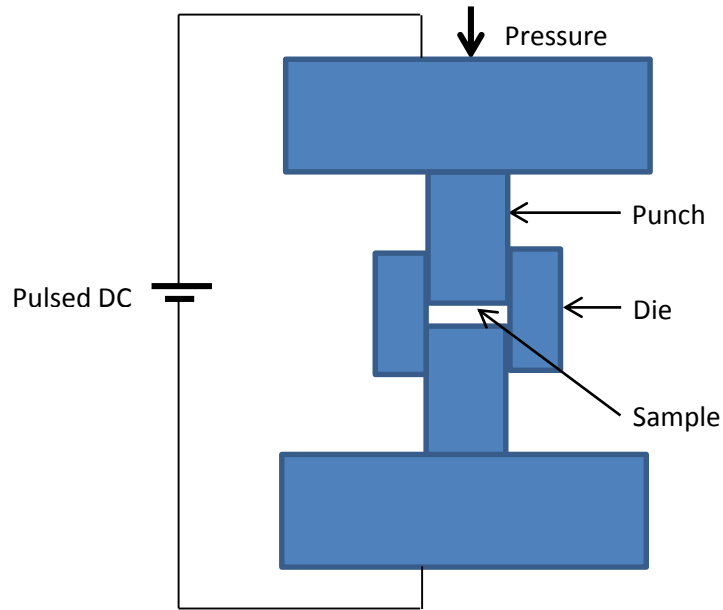


Fig. 1.1: Schematic of a typical SPS apparatus

High heating rate of the SPS system is attributed to the way the sample is heated. Joule heating inside the punches, die, and the conductive sample is an internal heating process, which can produce extremely high temperatures without the need of any other heating source. The ON-OFF DC pulsing was believed to be responsible for producing spark plasma between the pores in the sample powder and that is how the name spark plasma sintering came. However, the existence of spark during the SPS process was never proved experimentally. Other underlying phenomena contributing to the superiority of SPS are enhancement of surface diffusion by applied stress and current, local melting and evaporation, *in-situ* cleaning of particle surfaces and high density electric field causing fast mass diffusion.

Temperature variation inside the sample is quite small in SPS compared with that in hot pressing [12]. Moreover, the heating power in the SPS process is dissipated exactly at the

locations where the energy is required for the sintering, namely at the contact points of the powder particles. This results in insignificant grain growth and suppressed powder decomposition, which are important conditions for fabricating nano-materials. The conventional sintering techniques have not been a great success in producing nano-materials because of rapid grain growth and particulate effect. SPS technology can now open a new door to the production of bulk nano-materials.

SPS can produce compacts of nearly 100% theoretical density in almost any metallurgical or ceramic materials. Many difficult to sinter materials have been synthesized using SPS. Moreover, SPS allows sintering without undesirable phase changes due to shorter processing times. It has been successfully employed for producing composites and functionally graded materials (FGM).

Failure of the samples due to internal stress and micro cracks are quite often experienced in conventional sintering processes. This problem is also alleviated in the SPS process. Rapid mass diffusion and relatively consistent heating throughout the sample in SPS produces very little internal stress. As the SPS process can produce the finished part from the powder in a single step, it is possible to manufacture “net” and “near-net” shape with this process. Currently, SPS has succeeded in producing “net” shape products for symmetrical and simple shapes only.

The SPS process has many technological and economic advantages over conventional sintering processes. According to Thermal Technology LLC [13], the operational costs in SPS are consistently 50 to 80% less than conventional sintering technologies. In few cases, SPS technology was found to be 20 times faster than other sintering techniques. SPS applications most of the times require only minutes in comparison to the hours needed with other methods. The notable advantages of SPS in short are [14-18] :

- shorter sintering time

- lower sintering temperature and pressure
- no need of cold compaction
- finer and relatively more homogeneous microstructure
- higher density and densification rate
- near net shape capability
- less sensitivity to initial powder composition

Materials synthesized by SPS methods often show significantly improved physical and mechanical properties compared with those obtained by other conventional methods. Some of the improvements in material properties achieved by the SPS are:

- cleaner grain boundaries in sintered materials [19-22]
- improved thermoelectric properties [23-25]
- higher permittivity of ferroelectric materials [26-29]
- superior magnetic properties of magnetic materials [30-33]
- increased superelasticity of ultrafine ceramics [34, 35]
- remarkable increase in the bonding quality [36]

1.2 Literature Review

1.2.1 Experimental Background

As mentioned earlier, the idea of utilizing electric current as a sintering aid was first proposed by Taylor [37, 38] in 1933. He integrated the idea of resistance sintering into hot pressing of cemented carbides. In 1944, Cramer [39] invented a new resistance sintering method to consolidate copper, brass and bronze in a spot welding machine. Resistance sintering uses DC current through conductive powders under a constant pressure. However, very little progress was

made on this type of sintering process in the next few decades because of lack of fundamental understanding of its mechanism, poor controlling system, energy supply etc. The interest was renewed in 1960's when Inoue [40-42] successfully compacted metallic materials to a very high relative density (> 90 % of theoretical density) by an electric discharge process. Inoue applied pulsed DC current for sintering some low melting point metals (e.g. bismuth, cadmium, lead ,tin) as well as some high melting point metals (e.g. chromium, molybdenum, tungsten). Using single discharge from a capacitor bank rather than continuous pulse proposed by Inoue, a new resistance sintering technique called Electric Discharge Compaction (EDC) or Electric Discharge Sintering (EDS) was developed in the 1970's. Clyens *et al.* [43], Raichenko *et al.* [44] , Geguzin *et al.* [45] compacted various metallic powders using this method. However, the density obtained by this method was relatively low. Different other forms of electric current such as low frequency AC, high frequency AC, pulsed DC etc. were experimented for the development of a commercially viable sintering method. Finally in the 1990s, the first commercial spark plasma sintering machine was produced in Japan by Summito Heavy Industries Ltd. based on the design of Inoue. One of the differences of this machine with earlier ones was the die material. Earlier the die was made from an insulating material (e.g. glass, mica, bakelite, porcelain etc.) or had an insulated interior surface to confine the electric current within the powder. The SPS machine made by Summito Heavy Industries Ltd. had punches and the die made from electrically conductive graphite. It used a pulsed DC current (36 ms on and 6 ms off pulses) from the beginning till the end of the sintering cycle. This machine succeeded in compacting conductive as well as non-conductive materials to very high relative density. After the arrival of this new SPS machine, hundreds of research papers came out of Japan claiming successful sintering of variety of materials with improved properties in a shorter sintering time and at lower temperature than other available sintering methods [46, 47]. This method of sintering was referred in the literature by different names such as Field Activated Sintering (FAST) [48], Pulsed Electric Current Sintering (PECS) [49], Plasma Assisted Sintering (PAS) [50], Plasma Pressure Compaction (P²C) [51],

spark plasma sintering (SPS) etc. However, in this thesis, SPS designation will be used as it is the most commonly used rubric by the researchers (nearly 66.2%) [6].

Many explanations have been proposed about the fundamental mechanisms of spark plasma sintering. One of the major differences between the conventional sintering methods and SPS is the high heating rate obtained in the SPS which can be as high as 1000° C/min [7]. This feature of SPS is attributed to the way the system is heated. In SPS method, high density electric current passes through the punch, die and sample if it is conductive. Current passes through the tiny contact points between particles and experiences resistance at the contacts. When the electric charge carriers (electrons) collide with the atomic ions that make up the body of the conductors (punch, die or sample), electric energy is converted to heat energy in the microscale through resistive losses and conducted to the conductors (punch, die and sample). According to Joule's first law, the amount of heat energy generated is equal to the square of the current multiplied by the resistance of the conductor ($Q = I^2R$). As the current applied is very high, extremely high heating rate is achieved in SPS. This is an internal heating mechanism with no need of any external heating aid. Joule heat generated during this process helps welding of the particles under mechanical pressure. On the other hand, the conventional sintering methods like hot pressing heats the sample indirectly in an enclosed furnace and so the heating rate is limited by the radiation, convection and conduction. Heating rates in conventional sintering are usually <50-80° C/min. The high heating rate in SPS was believed to have an important role in enhancing densification and limiting grain growth.

The effect of heating rate on sintering has been investigated for different materials. However, there have been contradictory results and the effect of heating rate on densification and grain size is yet not obvious. Salamon *et al.*[52] investigated the effect of heating rate in consolidating alumina by pressureless sintering method. Higher heating rate resulted in enhanced densification by bypassing the non-densifying mechanism of surface diffusion and by creating an

additional driving force to particle sintering due to the large thermal gradients[53]. Stanciu *et al.*[54] studied the effect of heating rate on densification and grain size by SPS for two different types of material- non-conducting Al_2O_3 and conducting MoSi_2 with three different heating rates- $50^\circ\text{C}/\text{min}$, $250^\circ\text{C}/\text{min}$, and $700^\circ\text{C}/\text{min}$ respectively. They found that the heating rate had hardly any effect on densification for both materials. However, the grain size of Al_2O_3 decreased with increasing heating rate while the grain size of MoSi_2 showed no dependence on heating rate. Shen *et al.*[55] studied Al_2O_3 sample with six different heating rates ranging from $50^\circ\text{C}/\text{min}$ to $600^\circ\text{C}/\text{min}$ and found that the heating rate had no effect on relative density up to $350^\circ\text{C}/\text{min}$ and then the density decreased slightly for high heating rate of $600^\circ\text{C}/\text{min}$. On the other hand, the grain size decreased with the increase of heating rate up to $350^\circ\text{C}/\text{min}$; but for higher heating rate, there was negligible change in grain size. Wang *et al.*[56] found that relative density of sintered Al_2O_3 sample increased from a slower heating rate of $20^\circ\text{C}/\text{min}$ to $50^\circ\text{C}/\text{min}$ and then the density had no dependence on heating rate for higher heating rates. Zhou *et al.*[57] showed no influence of heating rate on the final density of Al_2O_3 sample for both higher ($50^\circ\text{C}/\text{min}$) and lower ($300^\circ\text{C}/\text{min}$) heating rates. Investigations on different other samples revealed that the heating rate had little to no influence on samples' relative density while the grain size had significant dependence on heating rate [58-61]. The contradiction in different research results could be because of faulty temperature measurements or different sintering parameters used in different cases. Another reason could be the change of densification mechanism at different heating rates. However, high heating rates of SPS can have a negative effect. It can result in significant temperature gradients, which will lead to inhomogeneous mechanical properties and microstructure in large samples [61-65].

Applied pressure in the sintering process plays an important role in densification both mechanically and intrinsically. Mechanically the pressure breaks the agglomerates and helps in particle rearrangement. Anselmi *et al.*[58] claimed that there is also an increment in the

densification driving force due to the application of pressure. An increase in pressure also leads to a decrease in the sintering temperature [66]. The effect of pressure on the relative density has been investigated for different samples such as, Al [67], Al_2O_3 [55], MgO [68], ZrO_2 [58]. With an increase in pressure a significant increase in relative densities were observed for all the materials. However, the effect of pressure on the relative density was larger in Al than the ceramics. This can be explained by the assumption that the metals undergo more mechanical deformation mechanism such as plastic deformation. Skandan *et al.* [69] claimed that the effect of pressure could be dependent on the particle size. According to them, the contribution of pressure is small when the particle size is small, but becomes significant for larger particles. There is a threshold particle size above which the pressure effect would be beneficial. Munir *et al.* [2] found that while the pressure had significant influence on the relative density, it had no effect on the grain size. There is a limit on the maximum pressure that can be applied during sintering process, which is determined by the strength of the die material. The most commonly used die material is high quality graphite, which can be used for a maximum sample pressure of around 140 MPa [9].

Raichenko [70] studied the effect of electric current on the plasticity of metals. He claimed that the electric current generated electron wind that could enhance the diffusion and dislocation motion. Xie *et al.* [71] investigated the effect of pulse frequency on the properties of sintered pure Aluminum compact. It was revealed that the relative density, electrical resistivity, and tensile properties had no significant dependence on pulse frequency. It was also found by calculating activation energy and observing SEM & TEM images that there was no obvious dependence of densification, deformation, and microstructure of the sintered sample on pulse frequency. The effect of pulsed DC current on the solid-state reactivity between Si and Mo layers in the spark plasma sintering apparatus was also studied by Anselmi-Tamburini *et al.* [72, 73]. They found that the direction of the pulsed DC current had no noticeable effect on the growth rate of the MoSi_2 layer. However, the growth rate of the layers was significantly higher in the

presence of the current than without it. Conrad [74] investigated the effect of electric current pulses on the flow stress and tensile strain for metals and fine-grained oxides in general. He explored that the high density electric current (10^3 - 10^6 A/cm²- very similar to SPS current density) pulses increased the strain rate of metals significantly while the flow stress of fine-grained oxides was substantially reduced under a modest electric field of 100-300 V/cm – much higher than the field experienced in SPS.

It was initially believed that the pulsed current caused the generation of sparks and even plasma discharges at the gaps between the powder particles [40, 46, 47]. When sparks are formed in the gap between the particles, an extremely high local temperature state of many thousand degrees Celsius is generated momentarily. This leads to evaporation and melting of the surface of the powder particles and necks are formed at the contact surfaces of the particles. Tokito [8, 47] claimed that spark impact pressure generated due to the formation of spark discharge facilitated surface activation and high-speed material transfer. It was also suggested that the current pulsing had a cleaning effect on the particle surfaces by removing impurities and absorptive gas existing in the pores between the particles. Anderson *et al.* [21] supported this claim after observing grain boundaries without oxidation between powder particles. Nagae *et al.* [75] claimed that the sparks generated during the early stage of sintering process removed trapped gases and destroyed the oxide layers present in Aluminum powders. However, the generation of spark discharge or plasma was never confirmed experimentally. Therefore, the effect of plasma generation in SPS system has always been debated.

Recently, Hulbert *et al.* [76,77] investigated the existence of spark plasma during the SPS process through a series of experiments. In-situ atomic emission spectroscopy, direct visual observations, and ultrafast in-situ voltage measurements were done for different types of powders and SPS conditions; no existence of plasma, sparking or arcing were found during the sintering process.

1.2.1 Computational Background

Although there have been numerous experimental research works on SPS, numerical simulation works to discover the underlying physical phenomena and evolution of temperature, current and stress during this process is limited due to the complex nature of various phenomena involved in SPS. The usual convention in SPS experiments is to control the system by setting a fixed temperature on the die surface. Measuring the temperature inside the sample is difficult because of the difficulties in properly focusing the pyrometer into the sample and placing the thermocouple inside the powder sample. Die surface temperature is not the exact representation of sample temperature. Difference between the temperatures inside the sample and that of die surface has been reported in the literature. Tomino *et al.*[78] observed a significant temperature difference (100°-200° C) between sample center and die surface for both conductive (Cu) and non-conductive (Al_2O_3) material. Inhomogeneous microstructures in the sample have also been reported in the literature [79, 80]. This is an indication that there might be temperature and/or stress gradients inside the sample. Numerical simulations can provide reliable data on these gradients inside the sample and other parts of the SPS system and thus, help optimize the production of different types of samples with controlled properties.

Raichenko *et al.*[81] made the first attempt to analyze resistance sintering numerically. He made a very simple mathematical model that accounted for the heat generation and heat transfer in a punch-specimen-punch system without a die. It was a 1D model showing the temperature variation only in the axial direction with large errors compared with experimental results. In the next 12 years, there was no noticeable numerical work done in the field of SPS. In 2001, Yoneya *et al.*[82] developed a model coupling the Fourier Transformation method with the method of Fundamental Solutions and solved partial differential equations to find the temperature and voltage distribution in some part of the punch, sample and die assembly. Their model was not the exact representation of the SPS system and was basically a simple representation of a partial

SPS assembly. However, their model gave a generalized idea about joule heat generation, temperature distribution, and voltage distribution in the system. Yucheng *et al.*[83] presented a mathematical model using one-dimensional Fourier equation to study the temperature field in spark plasma sintering. Steady state analytical solution was obtained since constant thermoelectrical properties were considered. Large temperature difference of 350° C was found between TiB₂/BN composite solid sample center and sample edge for a sintering temperature of 1700° C; however, the experimental results showed even higher temperature difference (450° C) between the two studied points. However, thermophysical parameters and the boundary conditions used in their study were not clearly stated and their simulation results were contradictory with others. Using finite element method (FEM), Jeon *et al.* [84] studied temperature distributions in Al₂O₃ sample by making thermal balance with conduction and joule heat generation. Grain growth of the sintered sample was also analyzed via Monte Carlo simulations by moving grain boundaries and peak points of a fine cell structure. Some other numerical models were proposed around the same time by Mori *et al.*[85] , Fessler *et al.* [86] , Heian *et al.* [87] and Matsugi *et al.*[88-90]. None of these models represented the SPS system properly as the boundary conditions used were not very realistic, only a small part of the SPS apparatus was considered, and a majority of the underlying mechanisms of SPS were neglected. Mori *et al.*[85] considered that all the electric current flowed through the sample and nothing through the die. Fessler *et al.* [86] decoupled the thermal and electrical analyses considering that the electrical properties were not dependent on temperature. Finite Difference Method was used by Heian *et al.* [87] and Matsugi *et al.* [88-90] which are not very suitable for a complex system like SPS. Moreover, their model was limited to steady-state temperature analysis and comprised of punch, sample, and die only.

A reliable thermal-electric sintering coupling model for the entire SPS system was first made by Zhang [91] and Zavaliangos [92] using ABAQUS software. They developed a new procedure to find the contact resistances of the SPS system by performing a series of experiments and incorporated contact resistances in their numerical model. They also showed the importance of electrical and thermal conductivity of the sample on the current and temperature distributions in the system by comparing results from graphite and Al_2O_3 samples. Based on the voltage prediction from his model, Zavaliangos [92] claimed that local field densities in SPS system was too low for the generation of spark plasma. Vanmessel *et al.* [93] made a similar type of model to find the temperature distribution in TiN and ZrO_2 samples using ANSYS software; however, they followed a different procedure to find contact resistances in the system. Yocheng *et al.* [94] modified his earlier model [83] and developed a coupled thermal-electric model to study the temperature field during sintering of TiB_2 -BN samples. Anselmi *et al.* [95] studied the temperature and current evolution during sintering of conductive and non-conductive materials without considering contact resistance using CFD-ACE+ code. He also studied the effect of current in sintering Si and Mo layers in a series of experiments [72, 73]. It was found in his study that although the presence of current was significant, the DC current direction and pulsing had no effect on the solid state reactivity in spark plasma sintering. This later became a common assumption in simulation of SPS for simplifying numerical computation. Olevsky *et al.* [96] proposed a new constitutive model that considered electromigration as a contributor to mass transfer during sintering. He also considered grain boundary diffusion and power law creep densification mechanisms. However, the validity of this model was questionable and not used by others later. McWilliams [97-99] improved the model developed by Zhang [88] by adding the densification effect in Tungsten sample to study the temperature and current field. The simulation results were compared with empirical data from a parallel experimental study and showed consistent agreement with that. He also studied the temperature field in non-cylindrical compacts. Around the same time, similar types of coupled thermal-electric models were developed by

Rathel *et al.*[100] , Cai *et al.*[101], Junting *et al.* [102], Molenat *et al.* [103] and Cura *et al.* [104] for different type of materials. All of them primarily tried to study the temperature fields of samples with different conductivities without considering the contact resistances at the interfaces. Tiwari *et al.* [105] used an empirical equation to find the contact resistances at the interfaces for their model developed by ABAQUS finite element software. The importance of considering the RMS value of experimental pulsed DC current as simulation input was discussed by Cincotti *et al.* [106]. They also proposed a methodology to determine temperature and load dependent horizontal contact resistances. Maizza *et al.* [107, 108] developed a numerical model that coupled electrothermal field with displacement field and determined all the sets of sliding contact resistances using a moving mesh technique in COMSOL software.

The mechanical aspect of the sintering process such as stress distribution was not considered in all the models discussed so far. Wang X. *et al.*[109] first presented a coupled thermal-electrical-mechanical finite element model for sintering alumina and copper samples at low temperatures and found significant stress gradients in the sample. Antou *et al.* [110] made another model capable of simulating stress distribution in sintered zirconium oxycarbide based on the work done by Wang X . However, Antou considered pure slip without mechanical friction at the part interfaces as the samples were sintered at high temperatures. Wang Cao *et al.*[111] implemented a fully coupled thermal-electrical-mechanical finite element model to find temperature and stress distribution in sample using COMSOL that used a Proportional-Integral-Derivative (PID) program to control the simulation against a set temperature. Song *et al.* [112] recently introduced a constitutive coupled electric-thermal-mechanical model while considering the effect of displacement field and local density distribution on sintering using MARC finite element software. Olevsky *et al.* [113] modified his earlier sintering model for quantitative prediction of densification behavior and grain growth in powder specimens using COMSOL.

Most of the numerical studies aimed at building a reliable modeling framework that can be applied in SPS system considering the maximum number of the internal underlying thermal-electrical-mechanical factors. Very little attention has been given to the importance of different process parameters on the temperature distributions in the SPS system. Recently, Munoz *et al.* [114] and Giuntini *et al.* [115] did some parametric investigation on temperature distribution in the SPS system. However, they did not substantially emphasize on the contact resistances. Giuntini *et al.* [115] considered all the surfaces to be ideal and totally neglected contact resistance effect whereas Munoz *et al.* [114] assumed the contact resistance values without doing experiments.

1.3 Scope of this thesis

As discussed earlier, SPS has many advantages over the conventional sintering processes such as hot pressing, hot isostatic pressing, and vacuum sintering process. Many of these advantages are attributed to the mechanism of heating the sample, shorter sintering, time and higher heating rates during the sintering process. However, there exist temperature gradients in the sample, which could result in non-uniform microstructure and physical properties of the sample. This could be a handicap for further advancement of this process especially for the production of large or net shaped samples. That is why it is very important to know the cause of these temperature gradients in the sample. The system tool design can significantly affect the temperature distributions in the sample. The effect of tool design has been discussed sporadically in the literature, but a detailed study on the importance of tool geometry has always been neglected. Different process parameters such as sintering temperature, input current, insulation around the die, etc. can play an important role in the temperature distributions in the sintered sample

In the present study, a coupled thermal-electric finite element model capable of simulating current, voltage, heat generation, and temperature distributions in the whole SPS system is developed using the commercially available ABAQUS software for the purpose of obtaining precise insight to the potential causes of temperature and current gradients in the sample. Two samples with totally different thermal and electrical properties – conductive copper and non-conductive alumina – were used for this simulation. All the contact resistances of the entire system were determined by an integrated experimental-numerical methodology. The developed model was then utilized to study the importance of tool geometry and process parameters in SPS process. Different sizes (both height and diameter) of samples, punches, and dies were studied. The importance of the position of the punch and die on sample temperature distribution was also determined. In addition to that, how the different process parameters, such as sintering temperature, input current and insulation around the die, can influence the system were also discussed. The results of this study can be used for SPS system design and process optimization for different kinds of materials according to the needs. This study could prove very useful for the production of large size sintered samples with controlled and tailored properties.

The remaining parts of this thesis are arranged as follows:

- In Chapter 2, a coupled thermal-electric finite element modeling framework for SPS process is proposed and implemented using the commercial ABAQUS software. A series of experiments followed by systemic numerical simulations are preformed to find the system contact resistance. Evolution and distribution of current and temperature in two different samples (alumina and copper) during the SPS process is discussed.
- In Chapter 3, the developed sintering model is utilized for determining the importance of tool geometry and different process parameters. The height as well as the diameter of the

sample, punch, and die is varied and different positions of punch-die are considered. Then, the effect of different sintering temperatures, input currents, and insulation around the die are discussed.

CHAPTER II

COUPLED THERMAL-ELECTRIC FINITE ELEMENT MODEL

2.1 Introduction

The first goal of this thesis is to build up a fully coupled thermal-electric model for our SPS setup. Thermal and electrical phenomena in the SPS process are closely related and dictate the temperature distribution in the system. In this chapter, we first address the underlying theories in the SPS process and build up a finite element model based on those theories. A detailed description of the contact resistance calibration test is given. The validation of the coupled thermal-electric model by a set of experiments is also presented. This modeling framework provides the framework for parametric study done in next chapter, which could be used for the production of large size sintered sample with controlled and tailored properties. Finally, we have discussed the evolution and distribution of current and temperature in two different samples (alumina and copper) during the SPS process based on our simulation results.

2.2 Finite element modeling details

2.2.1 Theory

When the pulsed DC current flows through the SPS tools and the sample (conductive), joule heating occurs due to the high resistance to current flow generated at the tiny contact surface areas between adjacent particles. Thermal as well as the electrical properties of the material are again dependent on temperature. Thus, thermal and electrical transfers in the system vary with temperature. All these result in a thermal-electric coupling in the SPS system.

The numerical model is built based on a set of Partial Differential Equations (PDE), which are coupled and solved using commercial ABAQUS finite element codes [91]. The current distribution is governed by the following Maxwells's equation –

$$\nabla \cdot \mathbf{J} = 0 \quad (2.1)$$

where $\mathbf{J} = \sigma \mathbf{E}$ is the current density, \mathbf{E} being the electric field and σ being the electrical conductivity. Again, $\mathbf{E} = -\nabla V$ where V is electric potential. So the equation (1) can be rewritten as –

$$\nabla \cdot \mathbf{J} = \nabla \cdot (-\sigma \nabla V) = 0 \quad (2.2)$$

The temperature distribution is governed by the following energy balance equation –

$$\rho C_p \frac{\partial \theta}{\partial t} = \nabla \cdot (k \nabla \theta) + \dot{q}_e + \dot{q}_c + \dot{q}_{conv} + \dot{q}_r + \dot{q}_{ec} \quad (2.3)$$

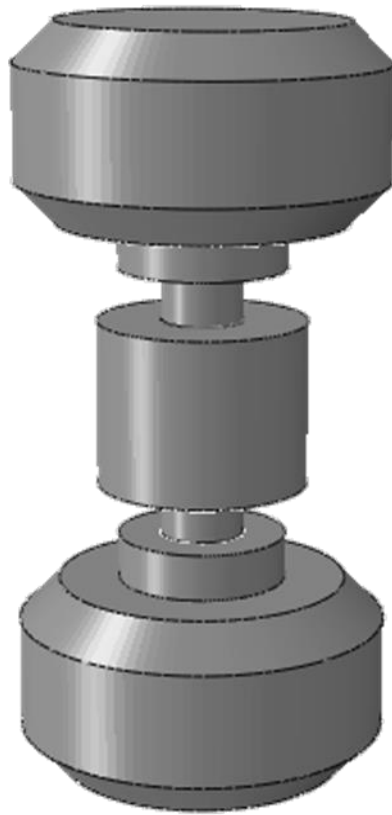
where ρ is the density, C_p the specific heat, θ the temperature, k the thermal conductivity and t the time. The terms \dot{q}_e , \dot{q}_c , \dot{q}_{conv} , \dot{q}_r and \dot{q}_{ec} represent heat generation by joule heating, heat transfer by conduction, heat transfer by convection, heat transfer by radiation and interfacial heating effects. Again, heat generation by joule heating can be expressed as –

$$q_e = JE = \mathbf{J} \cdot \mathbf{E} \quad (2.4)$$

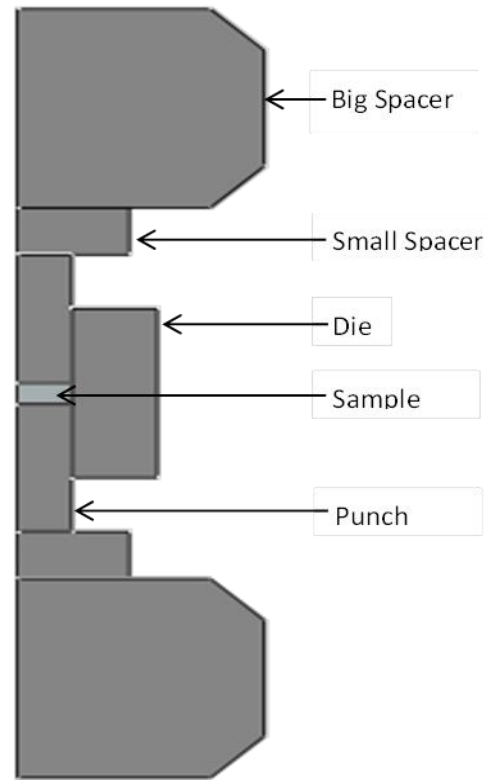
which couples equations (2.2) and (2.3). The modeling is done solving these two governing equations (Equation 2.2 and 2.3) simultaneously.

2.2.2 Model set up

The schematic of the SPS apparatus used in our model is shown in Fig. 2.1 and all the necessary dimensions of different tools are shown in Table 2.1. As all the parts in our SPS setup are cylindrical with axial symmetry, axisymmetric model was considered in our study. Axisymmetric model is computationally economic, as it requires much less time and memory. The spacers, punches, and die were made of Graphite. The electrodes in the SPS setup were not considered in this model. Two samples with different thermoelectrical properties were chosen for our study – (a) Non-conductive alumina and (b) Conductive copper. The thermoelectrical properties of Graphite, copper, and alumina used in this study are given in the Appendix. Material properties were considered to be isotropic i.e. no spatial variation of the properties. However, the sample as well as the tool materials show strong dependence on temperature. Hence, the temperature dependence of the properties was taken into consideration. Densification of the sample was not considered in this model. Both the alumina and copper samples were treated as fully dense. The sample's thermal and electrical properties are supposed to change with densification; however, this change will not cause significant difference in the temperature and electrical field of the sample at the end of heating cycle as the sintered sample's density is closed to the density considered in simulation (theoretical density).



(a)



(b)

Fig. 2.1: Schematic of the SPS apparatus used in the model: (a) 3d View and (b) axisymmetric cut view

Table 2.1: Dimensions of all the SPS tools used in the study

Name of the part	Dimension
Big Spacer	
a) Outside Diameter	90.1 mm
b) Inside Diameter	70.1 mm
c) Height	47.2 mm
Small Spacer	
a) Diameter	41 mm
b) Height	10 mm
Punch Length	30 mm
Die	
a) Height	40 mm
b) Thickness	15 mm
Sample	
a) Diameter	20 mm
b) Thickness	3 mm

The initial and boundary conditions used in this model were - (a) the initial temperature in the whole set-up was 27° C; (b) the temperature of the topmost and bottommost surface of the model (surfaces contacting the electrode) was constant at 27° C throughout the process as they are water cooled ; (c) all the lateral surfaces were considered to be electrically insulated; (d) the electric potential in the bottommost spacer surface was zero since it was grounded. (e) since the experiments were done in a vacuum chamber, convection heat transfers from the outer surfaces were neglected and only radiation from these surfaces were considered. Cavity radiation was approximated in the simulation for a cavity temperature of 27° C. The default geometric view

factor algorithm in ABAQUS was considered for this cavity radiation. Heat transfer by radiation is governed by the following equation –

$$\dot{q}_r = \sigma_s \varepsilon [(\theta_1)^4 - (\theta_2)^4] \quad (2.5)$$

where σ_s is the Stefan-Boltzman constant which has a value of $5.67 \times 10^{-8} \text{ W/m}^2\text{K}^4$, ε is the surface emissivity of graphite and, θ_1 and θ_2 are the temperatures of the emitting and absorbing surfaces respectively. For this study, $\varepsilon = 0.8$ was considered which was also used by other researchers [92,97,116].

The input load for this simulation was constant DC. The use of constant DC in this type of simulation has been justified by Anselmi *et al.* [95]. They proved by doing some Fourier Transform analysis that heating effect similar to the heating effect of pulsed DC, could be produced by constant DC in simulation. They also found that there should be no skin effect in all the conducting parts of the SPS setup for the entire range of DC pulsing frequencies used typically. That is why constant DC current is usually used as the input load in SPS simulation. The reference current was taken as 1000 A; however for some parametric study this current was also changed to 1100 A and 1200A also. The pressure applied on the top spacer was 5.7 MPa which translated a pressure of 70 MPa on the sample. All the contact resistance values used in this study were determined for 70 MPa pressure on sample. The total duration of the heating cycle was 600s with a heating rate of 100° C/min . Steady state temperatures and currents at the end of the heating cycle were considered for this study.

ABAQUS 6.12 commercial FEM software was used for simulation. All the governing partial differential equations with necessary boundary and initial conditions were solved in ABAQUS Standard using transient analysis. A total of 16,858 DCAX8E (8 node quadratic coupled thermal-electric quadrilateral) elements were used for meshing the model. The sample, die, and punch were meshed with smaller elements as these are the parts of significant interest An

initial time increment of 0.001 sec was considered. Maximum allowable temperature change in one increment was set as 10° C. The simulation took around 52 minutes to complete the analysis in a Pentium IV 3.2 GHz, 3.5 GB RAM desktop computer.

2.2.3 Contact resistance

Interface between two real surfaces is never continuous rather it has lot of discontinuities in the micro scale because of surface roughness, non-flatness, insulating layers and surface deposits [117, 118]. If heat and electric flux are imposed across the interface, the heat and current will flow only through the contact points, which are very small, compared to the apparent contact area. Electric current lines bundle together to pass only through the contact points. However, heat flux will flow through the contact points by conduction mainly and a very limited amount of heat can pass through convection or radiation. Constriction of the current and heat flow through the contact points causes a reduction of the volume of the material used for conduction and thus increases the resistance. This resistance is called contact resistance.

The temperature and current across the interface will not be a continuous function rather there will be a sharp change in temperature and current distribution across the interface due to the contact resistances (2.2). The thermal and electrical fluxes across the interface are respectively –

$$q_c = h_g(\theta_1 - \theta_2) \quad (2.6)$$

and

$$J_c = \sigma_g(V_1 - V_2) \quad (2.7)$$

where h_g and σ_g are thermal and electrical contact conductance coefficients respectively; θ_1, θ_2 are temperatures and V_1, V_2 are electric potentials of the contacting surfaces. The thermal and electrical contact resistances R_c^{th} and R_c^{el} are respectively defined as –

$$R_c^{th} = \frac{1}{\sigma_g S_A} \quad (2.8)$$

and

$$R_c^{el} = \frac{1}{h_g S_A} \quad (2.9)$$

where S_A is the apparent contact area. Joule heat is also generated at the interface because of contact resistances and thus the heat flux is also discontinuous across the interface which can be found from this equation –

$$\dot{q}_{ec} = J_c (V_1 - V_2) = \sigma_g (V_1 - V_2)^2 \quad (2.10)$$

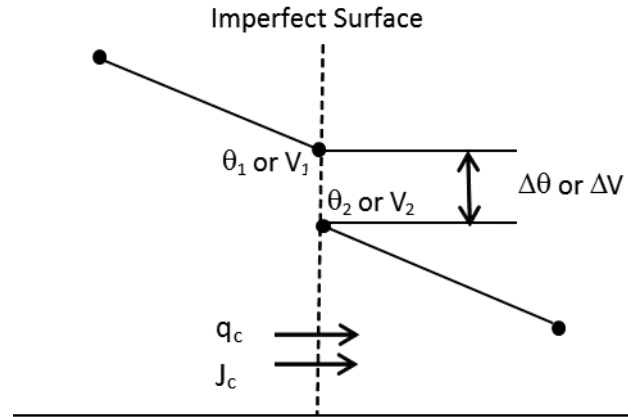


Fig. 2.2: Change in voltage and temperature through imperfect contacts

In the SPS setup, there are many contacting surfaces- both horizontal and vertical. The horizontal interfaces are - spacer-spacer interface, spacer-punch interface and punch-sample interface; whereas the vertical interfaces are sample-die interface and punch-die interface. All these interfaces have their own contact resistances that affect the current and temperature distribution of contacting surfaces. Simulation of SPS without considering the contact resistances under predicts the system resistance and as a result, the simulated temperatures would be lower. The difference between experimental and numerical temperature could be more than 200° C when contact resistances are not considered [95].

Contact resistance depends on many factors, of which contact surface area and temperature are the most important ones. Again, with the increase in pressure, the surface irregularities tend to disappear which increases the surface contact conductance; in other words, decreases the contact resistance. Thus, the two main factors that can affect the contact resistance in SPS system are pressure and temperature. Contact resistance for different pressures would be different and the model needs to be calibrated for different pressures. There have been some study on the dependence of contact resistance in SPS system on pressure [92, 119], however, its relation with temperature is not investigated thoroughly. It has been found that axial contact resistances are more significant than vertical contact resistances [92, 106, 108]. Vertical contact resistance is believed to be one of the causes for temperature difference between the sample center and the die outer surface.

However, all the experiments in this study were done at 70 MPa and the contact resistances were also determined for that pressure. 1100° C temperature at the die surface was taken as the reference temperature and the contact resistances were determined for that temperature. The contact resistances could be different for other temperatures. By assuming that the dependence of electrical and thermal contact resistance on temperature is same as the

dependence of thermal and electrical conductance of the bulk parts on temperature, the estimation of the contact resistances of the model for different temperatures can be avoided.

2.3 Experimental procedure

The spark plasma sintering equipment used for sintering in this study was SPS model 10-3 manufactured by Thermal Technologies LLC (Santa Rosa, CA, USA). Fig. 2.3 shows this SPS setup with all the necessary parts. This setup consists of three main units – the power supply unit, furnace with water cooling system and the vacuum control unit. Power supply unit has three individual 1000 amps units and thus the maximum current input of this setup is 3000 amps. The maximum voltage difference that can be maintained between the top and bottom electrode is 5V and thus this setup can provide a maximum input power of 15 kw. Having three individual power units is advantageous as no downtime is required if one unit fails. The input power can be programmed using the Dynatronix software which can program straight DC or pulsating DC with on time ranging from 4 to 900 ms and off time from 0 to 9 ms. As mentioned earlier, pulsed DC is typically used in SPS process. The power supply unit has the ability to change the pulse pattern during the run to attain maximum benefit in terms of densification. This SPS setup can achieve heating rates greater than 600°C per minute and it can reach a temperature of 2500°C in less than 5 minutes. The furnace has a water-cooled stainless steel chamber and the electrodes are also water cooled. The vacuum pump can achieve a high vacuum of 0.002 to 0.003 Torr, which is necessary to maintain purity of the samples. Digital servo valve controlled hydraulic system can produce a high compressive force, which can go up to 100 kN. The setup can achieve a high cooling rate inside the chamber by purging liquid nitrogen or liquid argon gas into it.

The target temperature and pressure profile can be programmed using a software named iTools. Temperatures are measured by either C/K type thermocouples or single color optical

pyrometer (Raytek, RAYMM1MHVF1V). The pyrometer can be moved on the X, Y and Z axis for focusing at the right point. During the sintering process, all the parameters – temperature, current, voltage, pressure and displacement can be monitored and recorded by a computer software named Specview. Various interlock safety system units equipped with alarms ensure safe sintering operation.

Once all the parameters needed for sintering are set, a known quantity of sample powder is placed in the die and then the die, punch, and spacers are positioned between the electrodes as shown in Fig. 2.4. The electrodes are made of stainless steel. The selection of materials for spacer, die, and punches depend on the sintering pressure. Graphite is the most commonly used material for these parts due to its high conductivity, ease of machining, availability, and low cost. However, graphite can be used for high pressure sintering and maximum sintering pressure achieved with graphite was reported to be 140 MPa. Typically, graphite is not used when the pressure goes above 100 MPa. Stainless steel, low carbon steel, tungsten carbide etc. can be selected as the material for spacers, die and punches when the pressure goes above that limit.

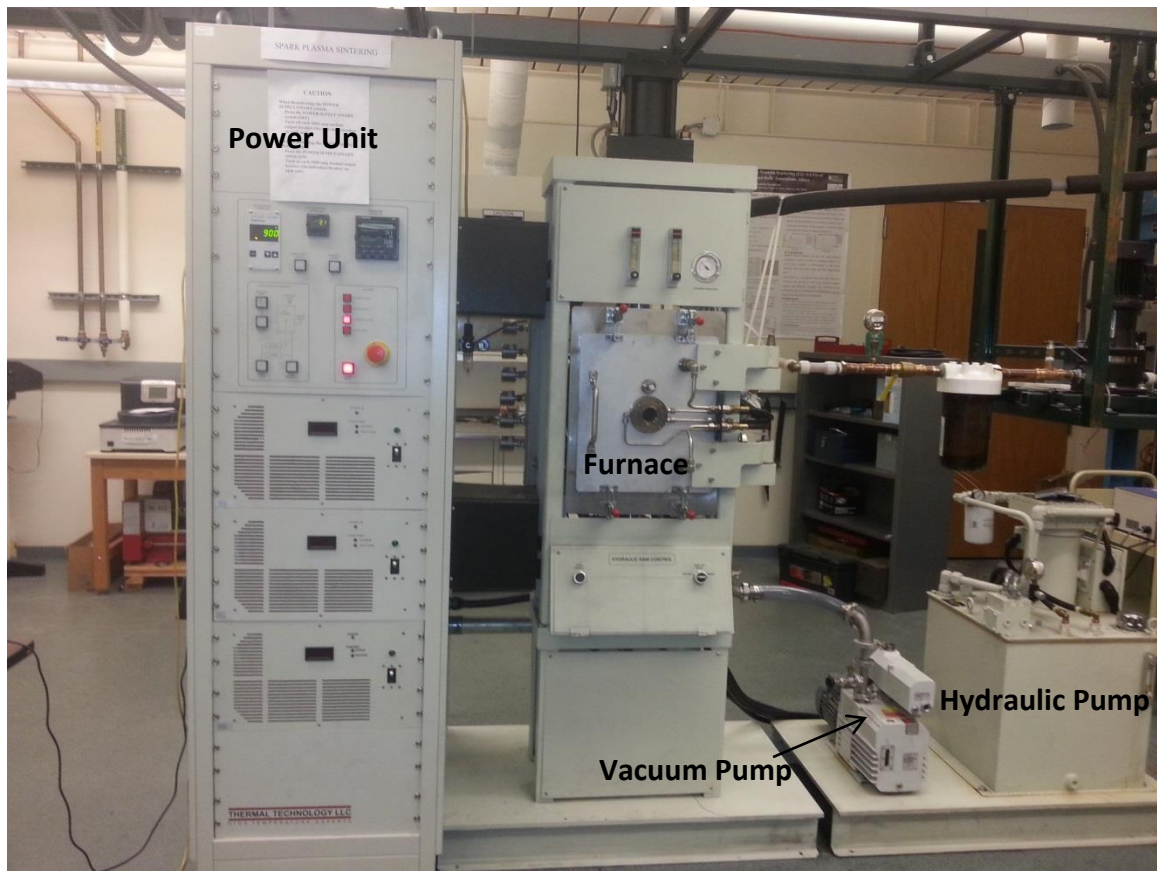


Fig. 2.3: Spark plasma sintering setup

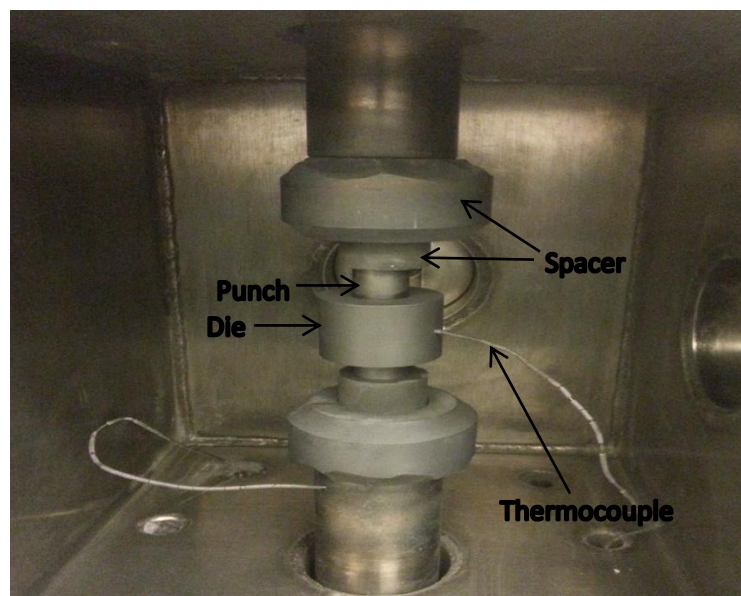


Fig. 2.4: Die-punch-sample assembly inside the furnace of SPS setup

2.3.1 Contact resistance calibration experiment

Before doing any simulation work, we first determined the contact resistances of our SPS setup. Determining the actual thermal and electrical contact resistance and calibrating the model for these properties are very important for accurate simulation result. Zhang *et al.*[92] were the first to address the importance of contact resistances in numerical modeling for SPS process. They proposed a calibration method to account for the contact resistances in the SPS model. The thermal and electrical contact resistances (or conductances) for our experimental setup were determined by following and modifying the procedure described by Zhang *et al.* [92] . Fig. 2.5 shows the basic algorithm used in this study to find the contact resistances in the system. By this integrated experimental-numerical methodology, we determined all the known contact resistances of our model. Three sets of experiments – (a) single punch test, (b) double punch test and (c) dummy run test, were performed to determine the electrical and thermal contact resistances. All the experiments were repeated three times and average values were taken. As mentioned earlier, contact resistances were found for a applied pressure of 70 MPa as all the sintering experiments in this study were done for a sintering pressure of 70 MPa. In all these experiments, our target was to find the overall system resistance for all the different configurations considered in these three tests. Then, simulations for the same configuration and process parameters were run without considering the contact resistances (or conductances) and the overall system resistance for that simulation was found. Obviously, there was difference between the experimental system resistance and simulation system resistance. Then, by adding some guessed contact resistances (or conductances) in the simulation, we slowly approached closer to the system resistance. This way the contact resistances for the whole system were determined.

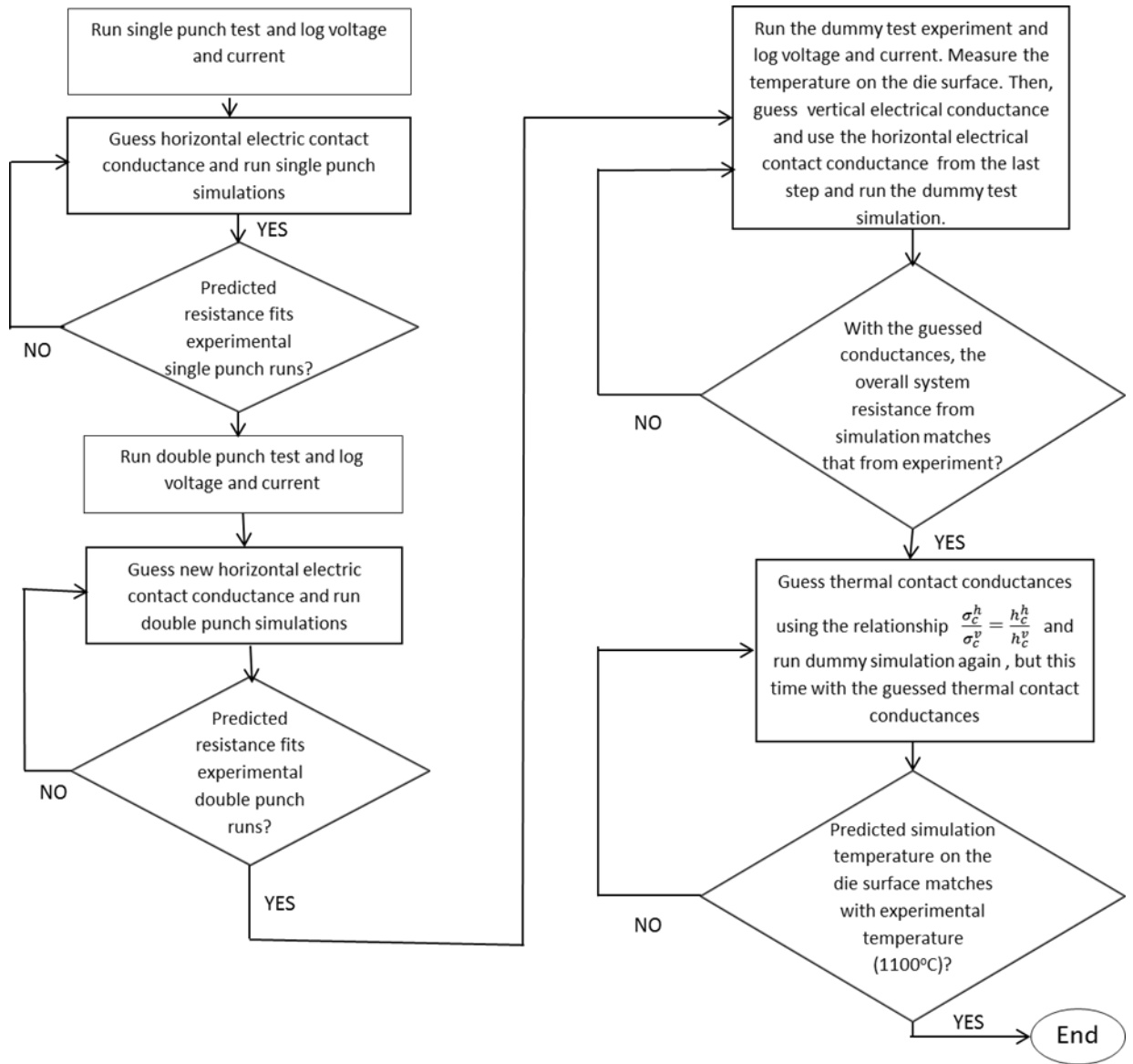


Fig. 2.5: Algorithm to determine system contact conductances (or resistances)

In the single punch test, the sintering experiment was done with the spacers and only one punch; no sample or die was used (Fig. 2.6). The experiment was run against a set temperature of 1100° C at a point vertically centered on the punch surface. The electrical contact resistances in effect for this experiment were the horizontal electrical contact resistances between the spacers and spacer-punch. The voltage (across the two exterior electrodes) and the current during the holding period were logged. In the first and the last 50 seconds of the holding period, there could be slight inconsistency or fluctuation in the current/voltage reading and hence, readings were taken after the first 50 seconds of holding period till the 550 seconds of holding period (total holding period was 600 seconds). The experimental overall system resistance was compared with the overall system resistance found from the simulation run without any contact resistance. The difference between the two results was due to the horizontal contact resistances between the spacers and between spacer and punch.

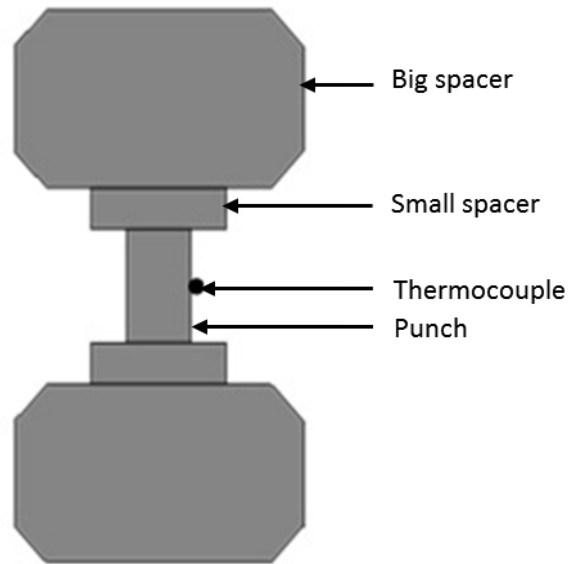


Fig. 2.6: Schematic of the single punch test

In the double punch test (Fig. 2.7), one more punch was added to the single punch test tools. Similarly, the experiment was run against a set temperature of 1100° C at a point on the upper punch surface and very close to the interface between the two punches. This time we had one more contact resistance in effect in our configuration; that was punch-punch contact resistance. This way we considered all the electrical horizontal contact resistances of our SPS setup.

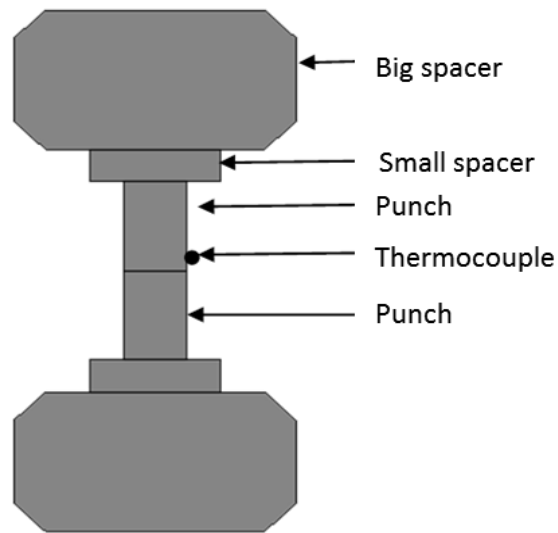


Fig. 2.7: Schematic of the double punch test

The third experiment was run with both of the punches and the die, but without any sample. This test has been referred as ‘dummy’ test (Fig. 2.8). The experiment was run against a set temperature of 1100° C at a point vertically centered on the die surface. This test was done for determining the vertical electrical contact resistance and also the thermal contact resistances. As we added the die to our double punch setup, we added the vertical contact surfaces and thus, vertical contact resistances to our system. The change in the overall system resistance was due to the addition of vertical contact surfaces. The system resistance from this test was compared with simulation system resistance with same configuration to find the vertical electrical contact

resistances. Temperatures from the test and simulation were also compared. The difference between the experimentally set temperature on die surface and the simulation temperature prediction at the same point was due to the thermal contact resistance at the punch-die interface.

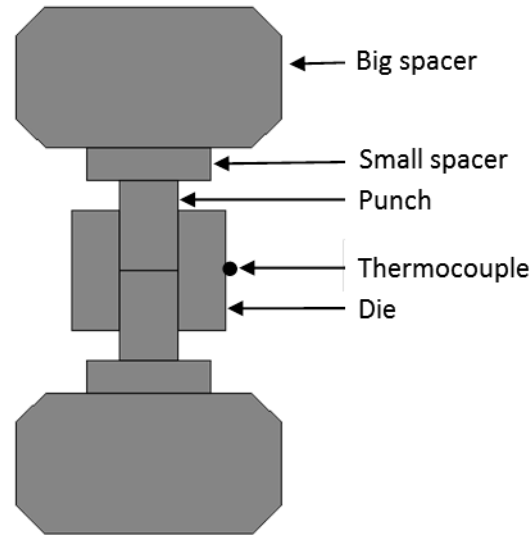


Fig. 2.8: Schematic of the dummy test

2.3.2 Spark plasma sintering (SPS) experiment

Experimental validations were first done with graphite cylinder and then with alumina powder samples. All the samples (both graphite cylinder and alumina) had a thickness of 3 mm and diameter of 20 mm. The graphite cylinders were cut in required dimensions using a cutter. The alumina samples were made from ultrapure 99.99% Alpha alumina nano powder (Inframat Advanced Materials) with an average particle size of 150 nm. Approximately 2.85 grams of this powder was weighed in a digital weighing machine and then placed inside the die between the punches as shown in Fig. 2.9. Sintering was done for three different temperatures – 1000° C, 1050° C, and 1100° C. The temperatures were measured in three different positions as shown in

Fig. 2.9 – (a) Point A - on the die surface, (b) Point B - on the punch surface and (c) Point C – inside the die and 2mm away from the sample surface. All the temperatures were measured using K- type thermocouples. Thermocouples were inserted in the holes drilled at the desired positions of the die and punch. Since in our SPS setup we could measure only one temperature at a time, we had to run separate sintering experiments for each of the three points. Again, three experiments were done for each temperature. This way we had to run 27 sintering experiments for alumina sample and 27 experiments for graphite cylinder. Inserting the thermocouple inside the sample is very difficult and more often damages the thermocouple. Hence, point C was rather chosen as an alternative point to measure temperature on sample surface. All the sintering operation consisted of a heating cycle with 100° C / min heating rate, followed by a holding period of 10 min, and then cooling in the same rate as heating. Sintering pressure was 70 MPa in all the cases. After sintering, the samples were taken out from the die using a hydraulic press (Fig. 2.10). Fig. 2.11 and 2.12 show the some of the graphite cylinders and sintered alumina compacts, respectively, used for the validation of our model. The density of the sintered alumina samples were determined using the Archimedes principle employing Mettler Toledo (Delta Range XD204) balance (Fig. 2.13). The formula used for determining the density was:

$$\rho = \frac{x}{x-y} (\rho_o - \rho_l) + \rho_l \quad (2.11)$$

where ρ is density of the sintered alumina sample, ρ_o is the density of water (0.99804 g/cm³ at room temperature) , ρ_l is the density of air (0.0012 g/cm³ at 25 °C), x and y are weight of the sample in air and water respectively . The relative density of the sintered samples was then found using the following formula:

$$Relative\ density = \frac{Density\ of\ the\ sintered\ sample}{Theoretical\ density\ of\ Alumina} \times 100\% \quad (2.12)$$

The theoretical density of alumina sample was 3.97 g/cm³ [120].

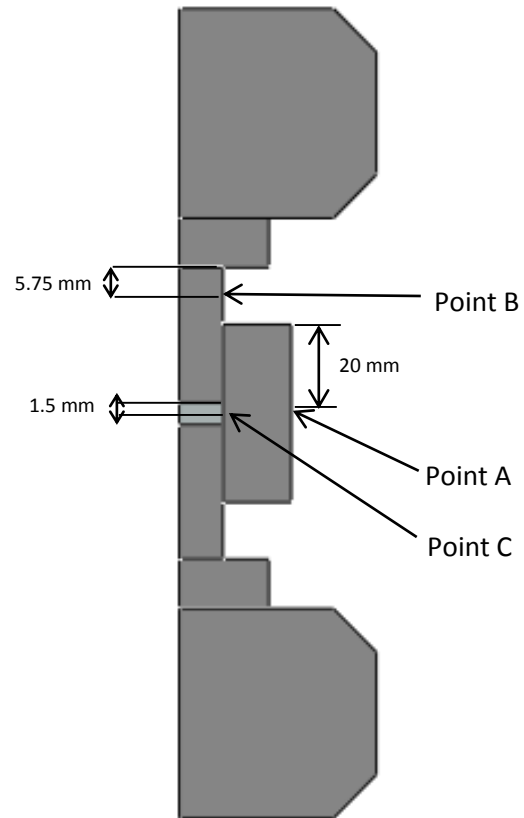


Fig. 2.9: Schematic of the SPS apparatus showing the three points where the thermocouples were positioned

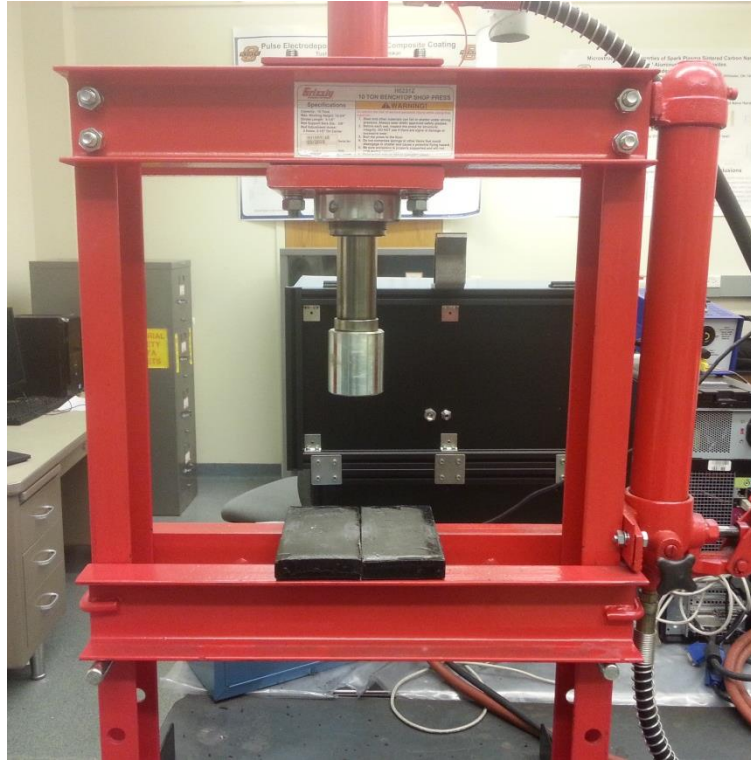


Fig. 2.10: Hydraulic press equipment

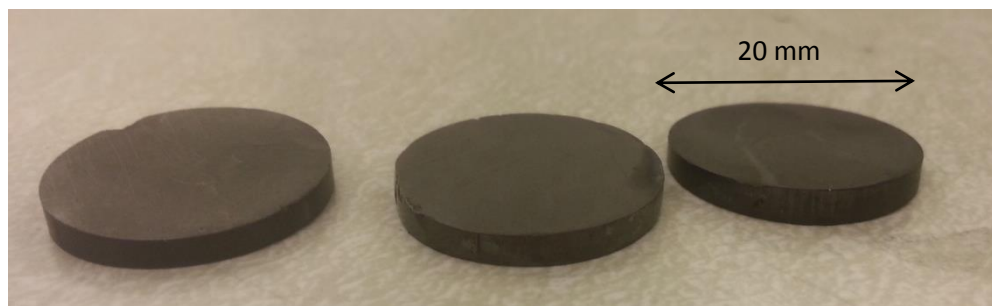


Fig. 2.11: Some of the graphite cylinders used for experimental validation

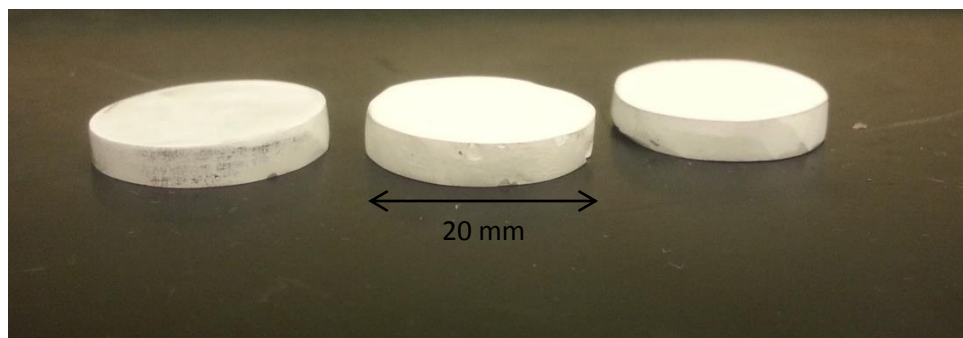


Fig. 2.12: Some of the alumina compacts sintered at 1100° C temperature and under 70 MPa pressure

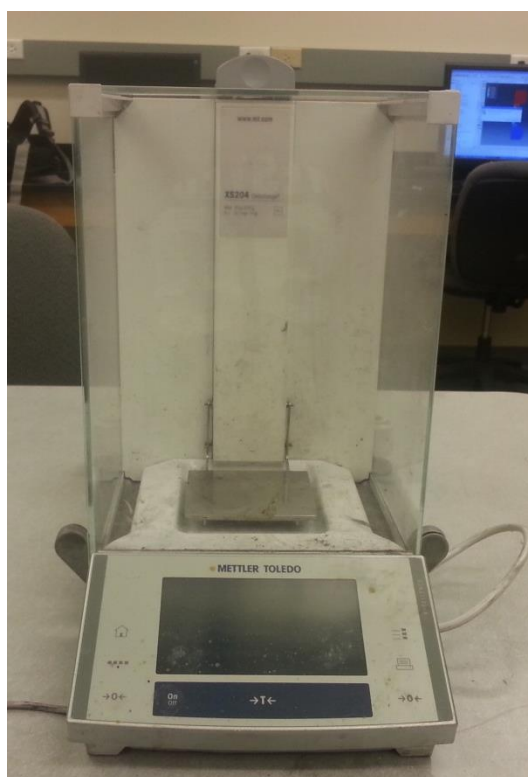


Fig. 2.13: Mettler Toledo (Delta Range XD204) balance

2.4 Results and discussion

2.4.1 Contact resistance calibration for the SPS setup

The result from the single punch experiment was compared with the single punch simulation to determine the model's horizontal contact resistances between the two spacers and between the spacer and punch interfaces. Thermal and electrical contact resistances were implemented in our simulation using the gap thermal and electrical gap conductances in ABAQUS 6.12. Fig. 2.14-2.16 show all the voltage, current, and resistance readings obtained from the three single punch experiments. Table-2.2 shows the overall system resistance from simulations for different guessed value of horizontal contact conductance. A contact conductance of $1 \times 10^{10} \Omega^{-1} \text{m}^{-2}$ was considered as infinite contact conductance and thus, its corresponding resistance is considered as zero contact resistance. Vertical electrical gap conductances and both of the thermal contact conductances were considered infinity in this test. It was also assumed that the electrical field is a weak function of thermal contact conductance (or resistance). Fig. 2.17 shows the comparison between the experimental and simulation system resistance for different values of horizontal electrical contact conductances. Simulation without any contact resistance under predicted the system resistance by 20%. Multiple simulations were run until we reached a good agreement between experimental and simulation result. Finally, a horizontal electrical contact conductance of $1.5 \times 10^7 \Omega^{-1} \text{m}^{-2}$ was found to be a good match for our single punch configuration.

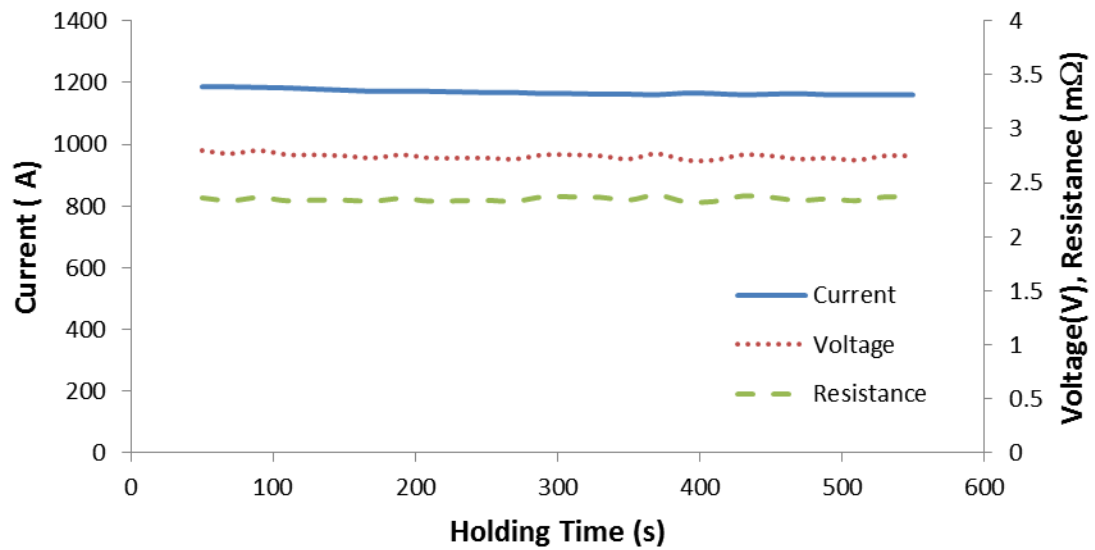


Fig. 2.14: Experimental data from single punch test – 1st run

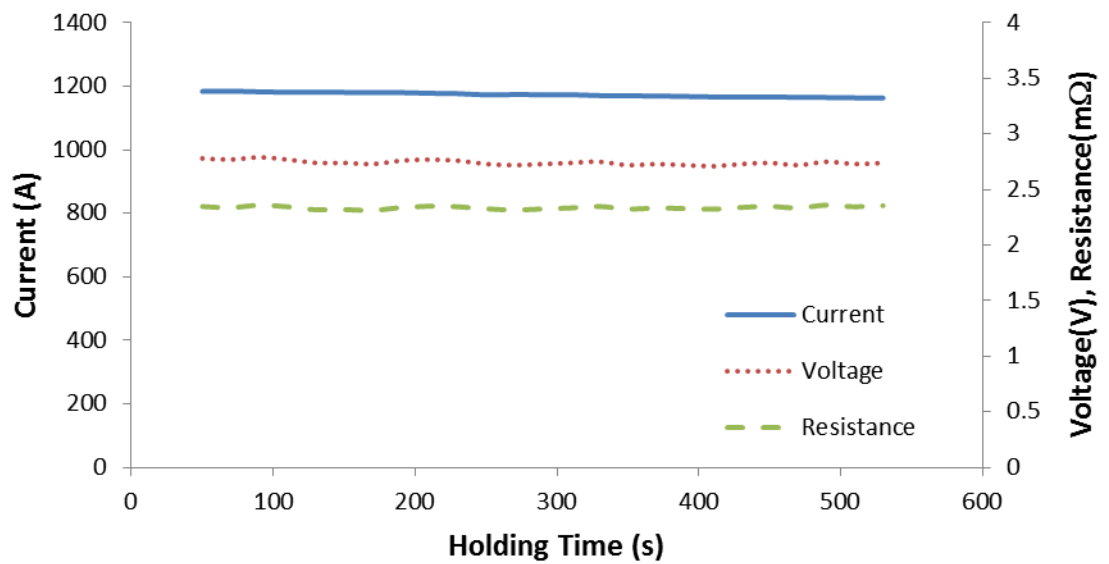


Fig. 2.15: Experimental data from single punch test – 2nd run

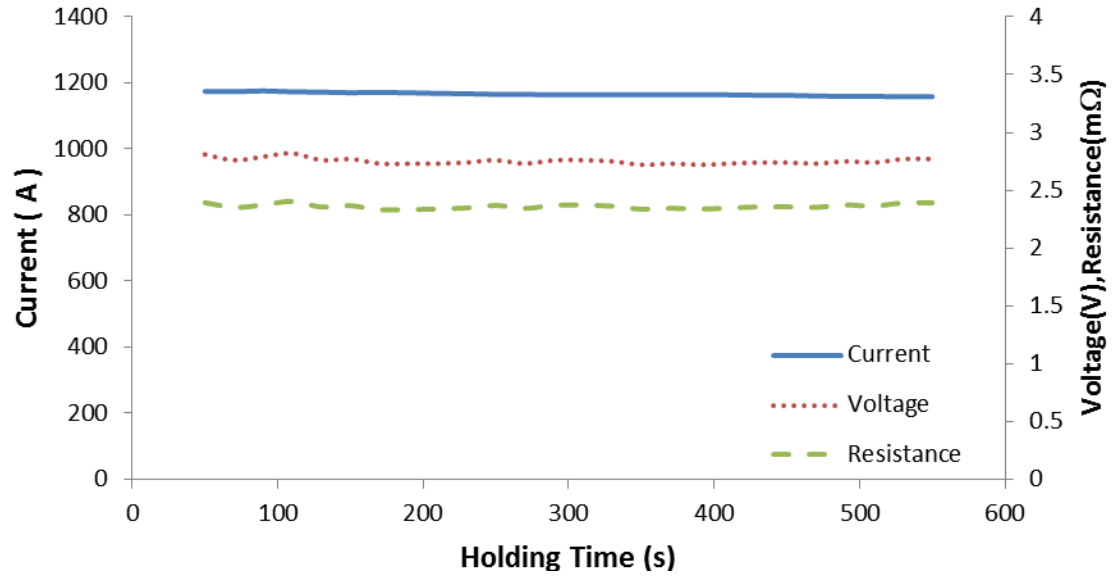


Fig. 2.16: Experimental data from single punch test – 3rd run

Table 2.2: Single punch simulation system resistance for different guessed horizontal electrical contact conductance

Gussed horizontal electrical contact conductance ($\Omega^{-1}\text{m}^{-2}$)	System resistance (mΩ)
1.0×10^{10}	1.88
1.0×10^9	1.93
1.0×10^8	1.99
9.0×10^7	2.01
8.0×10^7	2.03
6.0×10^7	2.06
5.0×10^7	2.07
4.0×10^7	2.09
3.0×10^7	2.15
2.5×10^7	2.21
2.0×10^7	2.25
1.5×10^7	2.35

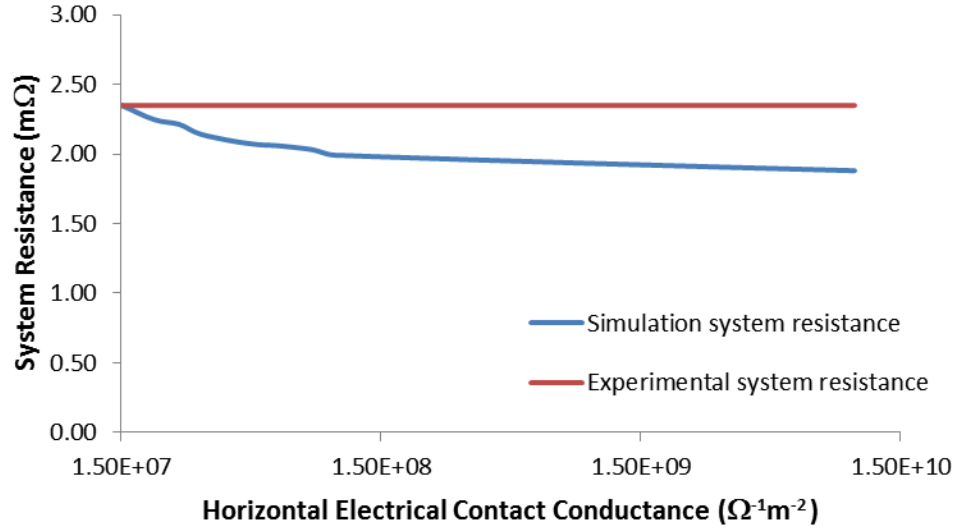


Fig. 2.17: Convergence of simulation system resistance to experimental system resistance in the single punch test

Next, the double punch experiment and simulation were done, and results were compared. Fig. 2.18-2.20 show all the voltage, current, and resistance readings obtained from the three double punch experiments. The total contact resistance in the double punch setup is equal to the contact resistance from the single punch test plus the contact resistance between the punches. Table- 2.3 shows the overall system resistance for double punch simulations for different guessed values of horizontal contact conductance. Fig. 2.21 shows the comparison between the experimental and simulation system resistance for different values of horizontal gap conductances in the double punch test. The best assumption for horizontal electrical contact conductance in the double punch test was found to be $5.5 \times 10^6 \Omega^{-1}\text{m}^{-2}$. We also assumed that the contact resistance between the sample-punch is same as the contact resistance between punch-punch and thus, eliminated the need for doing more experiments to find sample-punch electrical contact conductance.

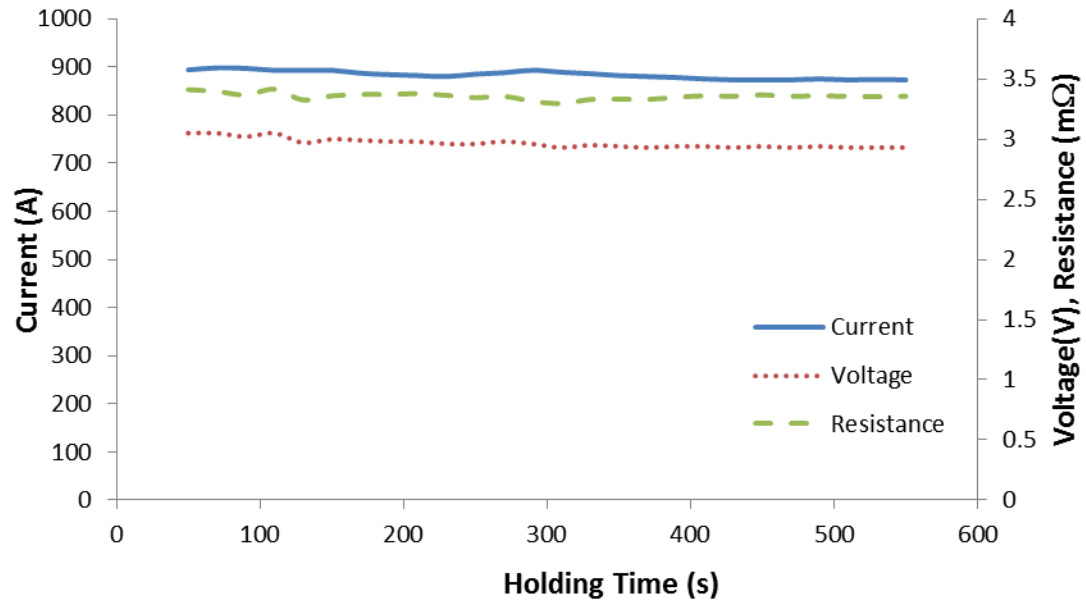


Fig. 2.18: Experimental data from double punch test – 1st run

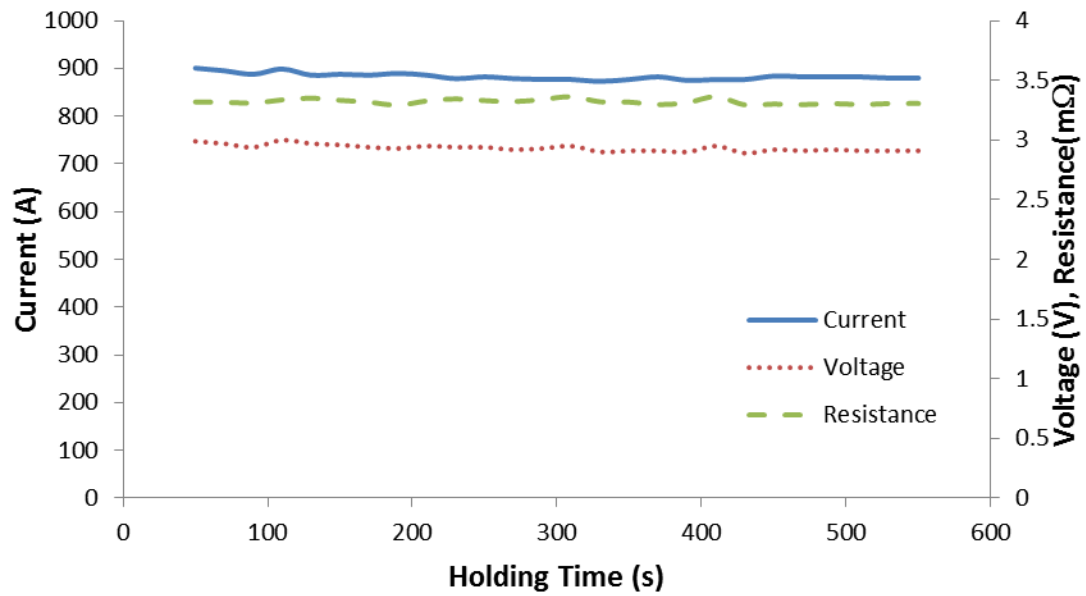


Fig. 2.19: Experimental data from double Punch test – 2nd run

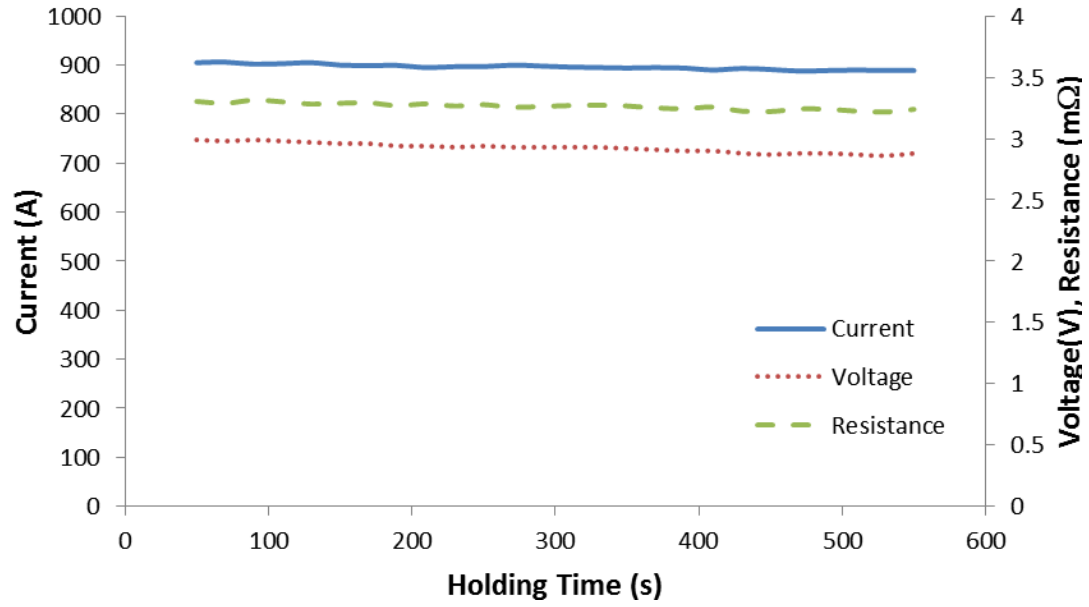


Fig. 2.20: Experimental data from double punch test – 3rd run

Table 2.3: Double punch simulation system resistance for different guessed horizontal electrical contact conductance

Guessed horizontal electrical contact conductance ($\Omega^{-1}\text{m}^{-2}$)	System resistance (mΩ)
1.5x10 ⁷	2.72
1.0x10 ⁷	2.88
9.0x10 ⁶	2.97
8.0x10 ⁶	2.99
7.0x10 ⁶	3.03
6.6x10 ⁶	3.05
6.4x10 ⁶	3.08
6.1x10 ⁶	3.11
5.9x10 ⁶	3.18
5.8x10 ⁶	3.22
5.7x10 ⁶	3.27
5.6x10 ⁶	3.29
5.5x10 ⁶	3.31

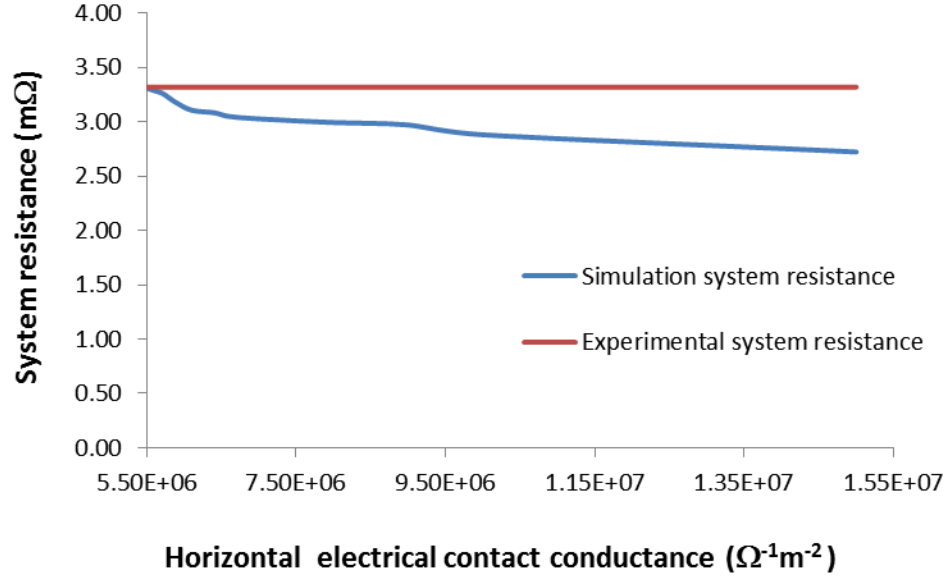


Fig. 2.21: Convergence of simulation system resistance to experimental system resistance in the double punch test

The calibration was then done for dummy test. The only unknown electrical contact conductance (or resistance) is now the vertical electrical contact conductance between the punch and die. The dummy experiment data are shown in Fig. 2.22-2.24. Table 2.4 shows the overall system resistance for dummy simulations for different guessed values of vertical electrical contact conductance. A vertical electrical contact conductance of $4 \times 10^6 \Omega^{-1}\text{m}^{-2}$ calibrated the model most closely as shown in Fig. 2.25. After finding all the electrical contact conductances, we needed to find the thermal contact conductances. There was a difference between the experimentally set temperature on die surface and the simulation temperature prediction at the same point. This was due to the thermal contact resistance at the punch-die interface. Simulations were then run with different guessed thermal gap conductances based on the following relationship -

$$\frac{\sigma_c^h}{\sigma_c^v} = \frac{h_c^h}{h_c^v} \quad (2.13)$$

where σ_c^h and σ_c^v are horizontal and vertical electrical contact conductances and h_c^h and h_c^v are horizontal and vertical thermal contact conductances. Same relationship was considered by other researchers in the past [92, 116].

Table 2.5 shows the simulated die surface temperature for different guessed thermal contact conductances and Fig. 2.26 shows how the simulated die surface temperature converged to experimental die surface temperature for those guessed thermal contact conductances. Eventually, the derived contact conductances for this study were as follows–

$$\sigma_c^h = 5.5 \times 10^6 (\Omega\text{m}^2)^{-1} \quad \sigma_c^v = 4 \times 10^6 (\Omega\text{m}^2)^{-1}$$

$$h_c^h = 5.5 \times 10^3 \text{ W/m}^2\text{K} \quad h_c^v = 4 \times 10^3 \text{ W/m}^2\text{K}$$

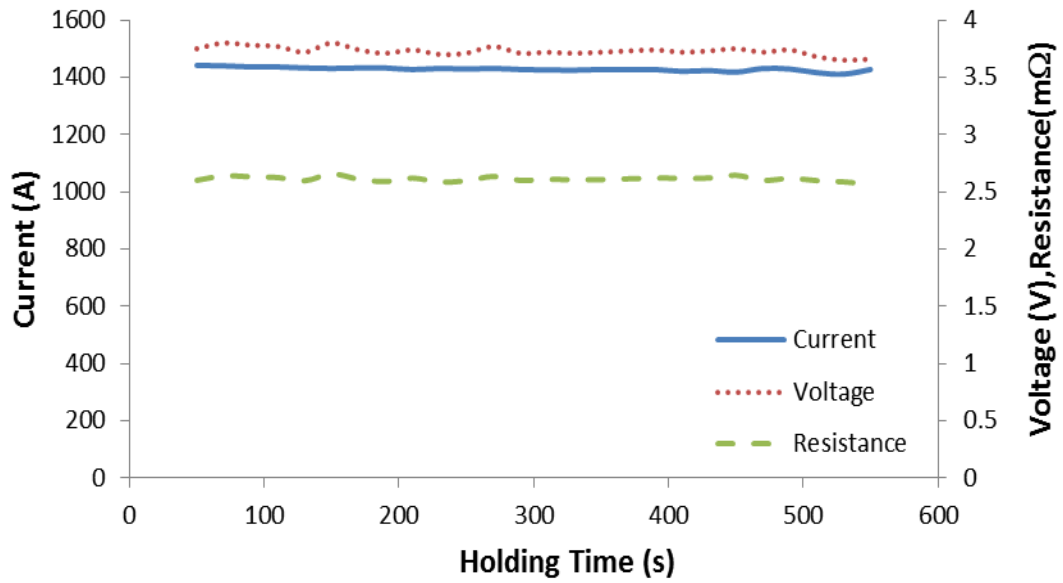


Fig. 2.22: Experimental data from dummy test – 1st run

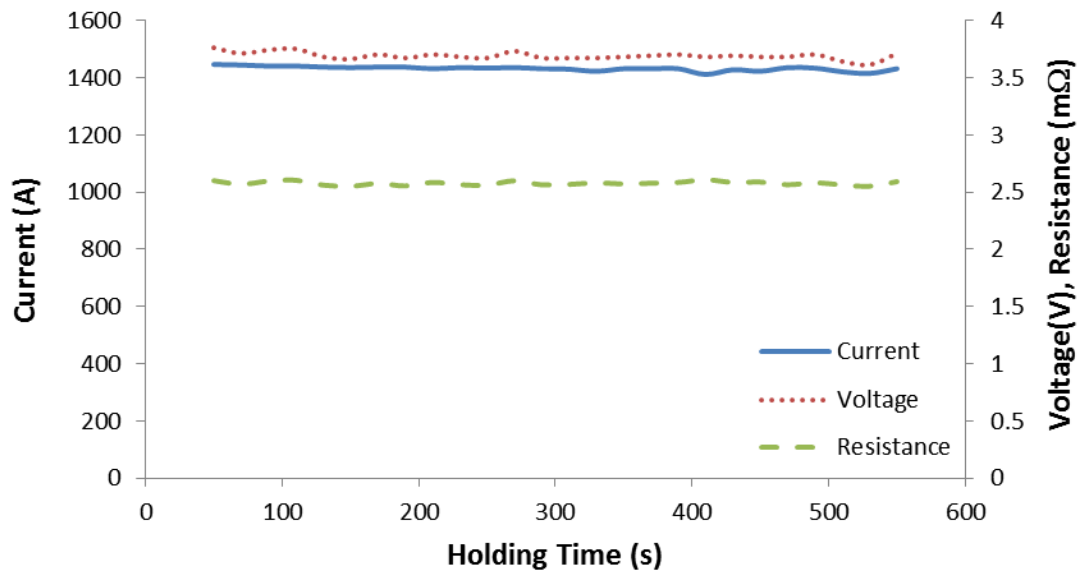


Fig. 2.23: Experimental data from dummy test – 2nd run

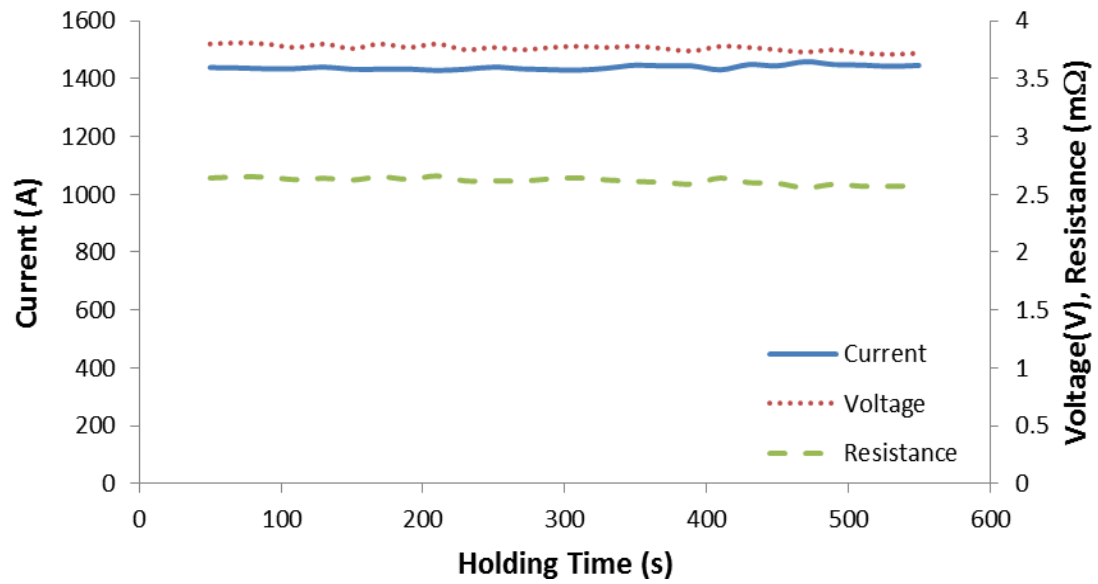


Fig. 2.24: Experimental data from dummy test – 3rd run

Table 2.4: Dummy test simulation system resistances for different guessed vertical electrical contact conductances

Guessed vertical electrical contact conductance ($\Omega^{-1}\text{m}^{-2}$)	System resistance (m Ω)
1.0×10^{10}	2.29
1.0×10^9	2.31
1.0×10^8	2.33
1.0×10^7	2.36
9.0×10^6	2.38
8.0×10^6	2.38
7.0×10^6	2.40
6.5×10^6	2.41
6.0×10^6	2.42
5.0×10^6	2.43
4.8×10^6	2.45
4.6×10^6	2.49
4.5×10^6	2.53
4.3×10^6	2.56
4.2×10^6	2.58
4.0×10^6	2.60

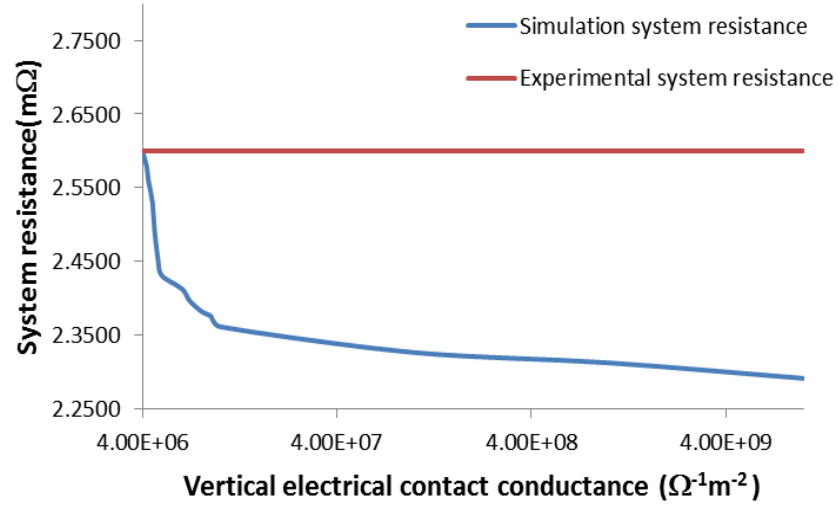


Fig. 2.25: Convergence of simulation system resistance to experimental system resistance in the dummy test

Table 2.5: Simulated die surface temperature for different guessed thermal contact conductances in the dummy test

Vertical thermal contact conductance (W/m ² K)	Horizontal thermal contact conductance (W/m ² K)	Simulated die surface temperature (°C)
10000	13750	1068
9500	13063	1072
9000	12375	1074
8500	11688	1076
8000	11000	1077
7500	10313	1079
7000	9625	1082
6500	8938	1084
6000	8250	1086
5500	7563	1089
5000	6875	1092
4500	6188	1096
4000	5500	1100

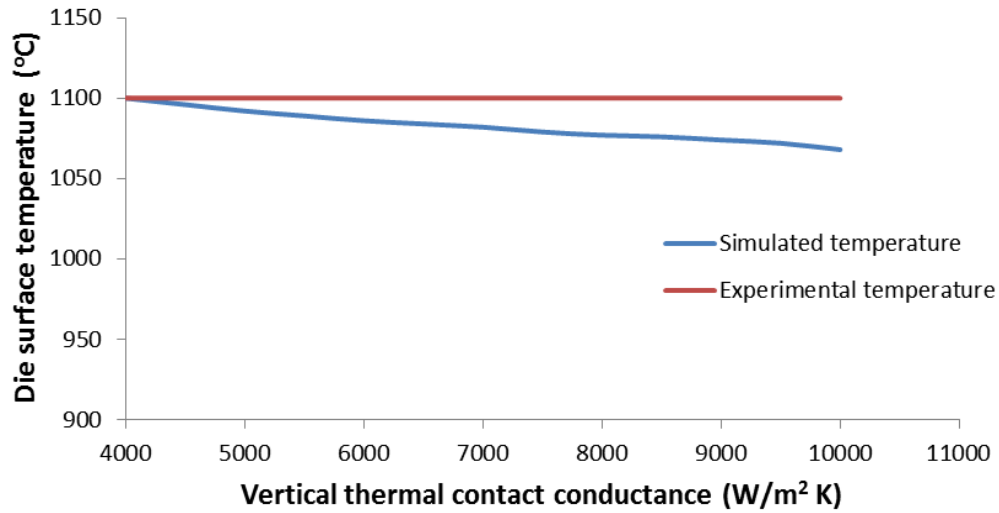


Fig. 2.26: Convergence of simulated die surface temperature to experimental die surface temperature in the dummy test

2.4.2 Experimental validation of the model

After determining the contact resistances, sintering experiments were first done with 3 mm thick and 20 mm diameter graphite cylinders for the three studied temperatures and points. Simulations with same sample and tool geometry, and process parameters were run and compared with the experimental results. Experimental temperature and current at the holding period were compared with simulation results at the end of heating cycle. In our SPS setup, a target temperature with specific heating rate at a reference point is set before the experiment. Necessary amount of current is applied by the system to attain that target temperature at the end of the preset time. At the holding period, the target temperature is held constant at the reference point and the corresponding current is varied slightly by the system to maintain that target temperature constant. The similar condition is found in the simulation at the end of heating cycle as the temperature becomes steady for a specific input current then. This similarity between the two cases is the basis of our comparison. However, a constant DC current was used in our simulation whereas the experimentally applied current was pulsed DC. Moreover, resistive heating occurring in a pulsed DC driven circuit is proportional to the RMS value of the pulsed DC current [93, 106]. On the other hand, the display in our SPS setup shows the peak values of the pulsed DC current, not the RMS value of the pulsed DC current. Therefore, the experimentally applied pulsed DC current had to be converted so that it could be used properly as the simulation input. This conversion was done according to the formula provided by the manufacturer of our SPS apparatus [13] which are as follows:

$$\text{Average Current} = \text{Peak Current} \times \text{Duty Cycle of the pulsed DC} \quad (2.14)$$

$$\text{RMS current} = \sqrt{\text{Peak current} \times \text{Average current}} \quad (2.15)$$

$$\text{Duty Cycle of pulsed DC} = \frac{\text{ON time}}{\text{ON time} + \text{OFF time}} \quad (2.16)$$

In our SPS setup, we used a pulsed DC current with 85ms of ON time and 6ms of OFF time and thus had a duty cycle of 0.934. Thus, we found for our SPS setup,

$$RMS\ current = 0.966 \times Peak\ current$$

All the peak current readings from the experiments were converted into the RMS current using the aforementioned equation to apply in the simulation.

A transient analysis was done in ABAQUS 6.12. However, the simulated temperatures matched well with the experimental temperatures only in the steady state after 600 seconds. This happened because the input current at this stage was same for both experiments and simulations. The experimental and simulation temperature history for sintering alumina sample at a set temperature of 1100° C on the die surface is shown in Fig. 2.27.

The comparison between experimental and simulation temperature at points A, B and C for graphite cylinder test is shown in Fig. 2.28-2.30. In the SPS experiment, three readings were taken at each point (Point A, B, and C) for one particular temperature and the average reading was considered to have more confidence in the result. Three different experimental set temperatures (1000° C, 1050° C, 1100° C) at three points (Point A, B, C) were compared with simulation result. The experimental temperatures were always slightly higher than the simulated temperatures. The maximum variation between the two results at the three points (points A, B, and C) were respectively 15° C, 17° C, and 17° C respectively. The reason for this small variation could be because of some of the assumptions we used in our simulation. Temperatures at the three points were not measured simultaneously due to the limitation of our SPS setup. Only one temperature reading can be taken at a time in our SPS setup and hence, we had to run three separate experiments to determine temperatures at three different points. Since the experiments were done at different times, the power supply condition could have altered which could consequently affect the input current in the SPS setup. Thermocouple positions could also change

during the experiments could be another reason for variations. However, this variation of simulation result from experiments is acceptable comparing to results from other research in the literature [95, 106, 108, 110, 116].

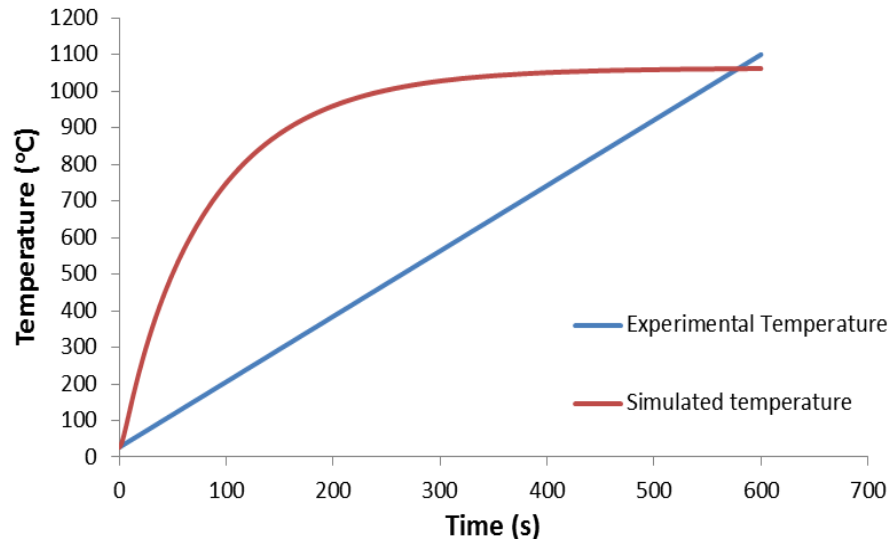


Fig. 2.27: Experimental and simulated temperature history data for sintering alumina sample at a set temperature of 1100° C on the die surface

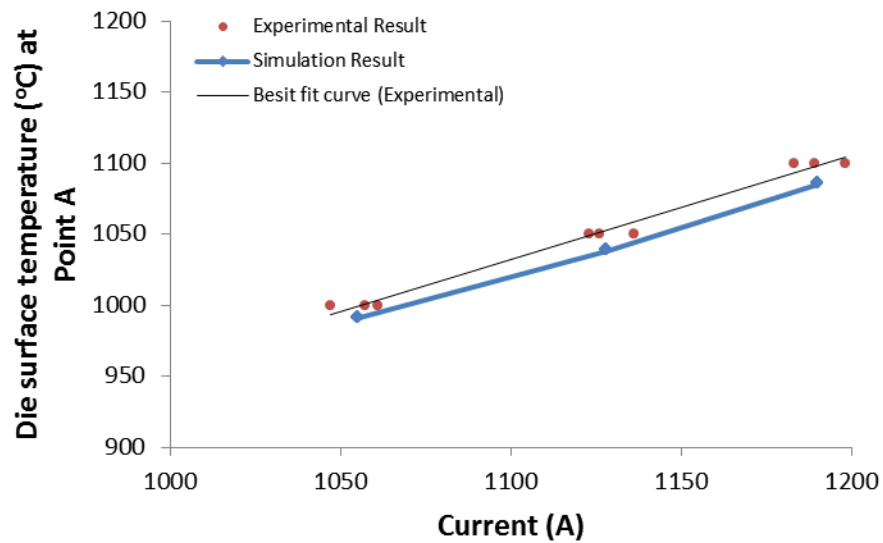


Fig. 2.28: Comparison between experimental and simulated die surface temperature at point A for test with graphite cylinder

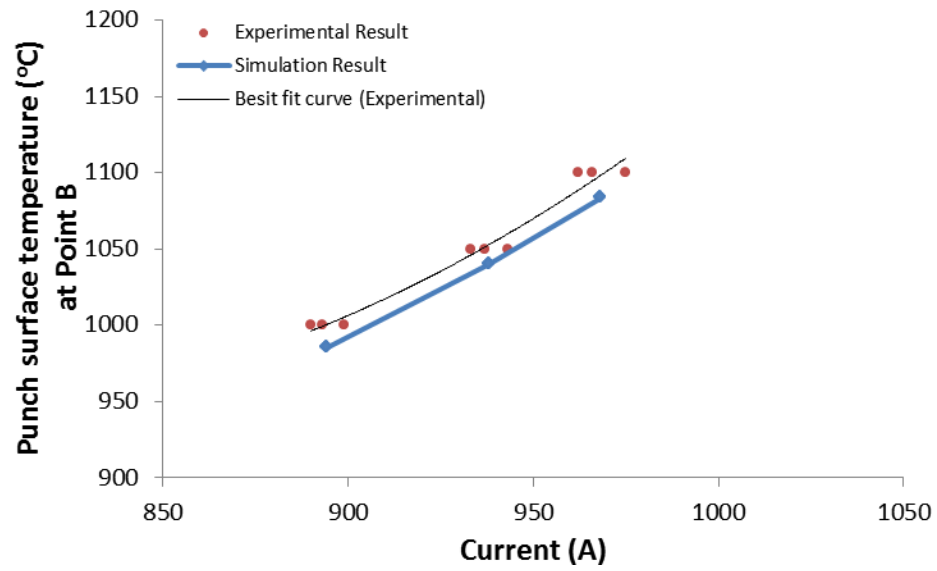


Fig. 2.29: Comparison between experimental and simulated punch surface temperature at point B for test with graphite cylinder

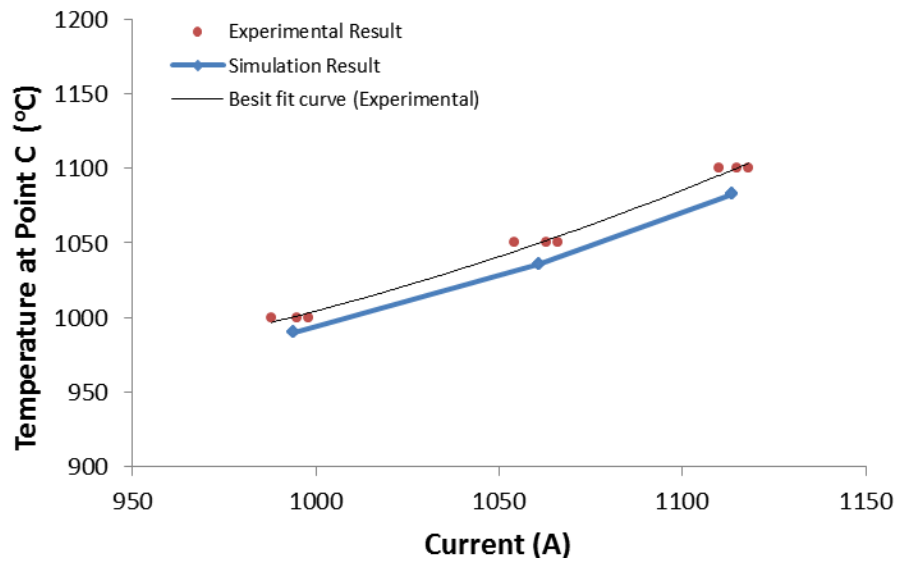


Fig. 2.30: Comparison between experimental and simulated temperature at point C (inside the die, 2mm from the sample surface) for test with graphite cylinder

After the model showed satisfactory results for the graphite cylinder, we applied this model for alumina samples. The comparison between simulation and experimental results for alumina samples are shown in Fig. 2.31-2.33. The maximum variations in temperature between the two cases for the three points studied here (Point A, Point B, and Point C) are 34° C, 47° C and 33° C respectively. At lower temperature (1000° C), the variation between experimental and simulation results were small; minimum variation being only 17° C at point C. With the increase in temperature the variations increased slightly, however, the deviation of the simulated temperature from experimental temperature was always less than 5%, which is very satisfactory. Table 2.6 shows the percentage deviation of the simulated temperature from experimental temperature for graphite cylinder and alumina sample at all the temperatures and all the points. The reasons for differences between simulated and experimentally measured temperatures in the case of alumina sample could be same as discussed above for graphite cylinder case. One more reason for discrepancies in the case of alumina sample is the different state of the sample used in experiment and simulation. In the simulation, we considered fully dense alumina as our sample. On the other hand, we started our sintering experiments with alumina powder. However, the sample reaches close to its theoretical density at the end of heating cycle. Table 2.7 shows the relative density of the sintered alumina samples for three different temperatures. The sample's thermal and electrical properties are supposed to change with densification; however, this change will not cause significant difference in the temperature and electrical field of the sample at the end of heating cycle as the sintered sample's density becomes close to the density considered in simulation (theoretical density) at the end. Despite considering some assumptions and differences between theoretical and experimental conditions, the steady state simulation temperature showed very good agreement with experimentally measured temperature.

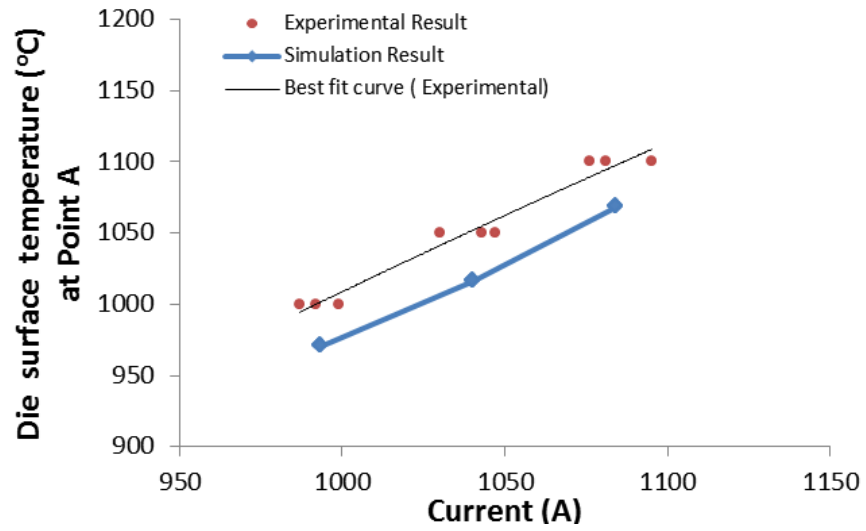


Fig. 2.31: Comparison between experimental and simulated die surface temperature at point A for test with alumina sample

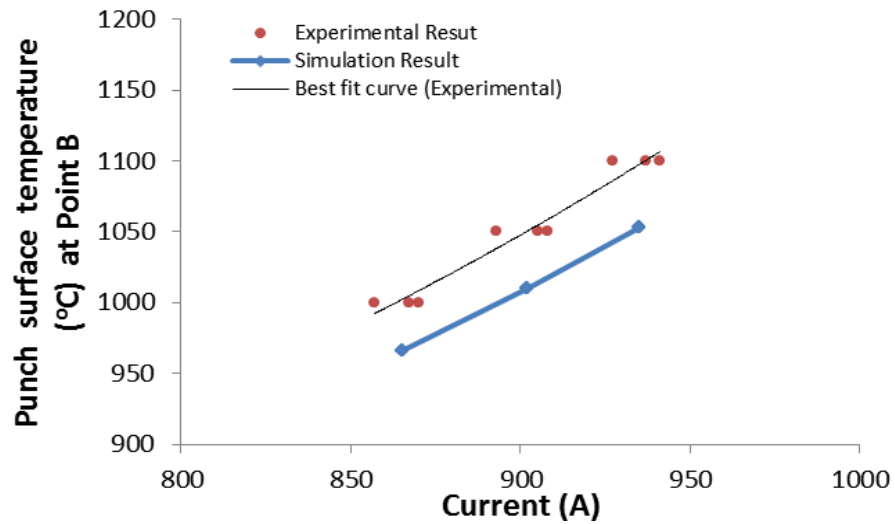


Fig. 2.32: Comparison between experimental and simulated punch surface temperature at point B for test with alumina sample

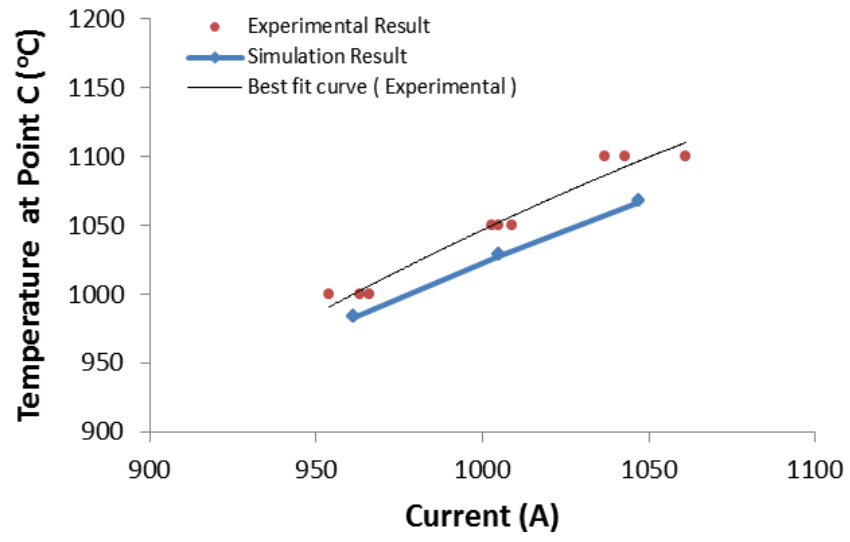


Fig. 2.33: Comparison between experimental and simulated temperature at point C (inside the die, 2mm from sample surface) for test with alumina sample

Table 2.6: Percentage difference between experimentally measured and simulated temperature at three studied points for three temperatures considered

Studied points	Experimental temperature	Percentage difference between experimental and simulated temperature	
		Graphite cylinder	Alumina sample
Point A (Die surface)	1000° C	0.9	3
	1050° C	1.1	3.2
	1100° C	1.4	2.9
Point B (Punch surface)	1000° C	1	3.4
	1050° C	1.3	3.8
	1110° C	1.5	4.3
Point C (Inside die, 2mm from sample surface)	1000° C	1.5	1.7
	1050° C	1	2.1
	1100° C	1.7	3

Table 2.7: Average of relative densities of the alumina samples sintered at different temperatures

Temperature (°C)	Relative density (%)
1000	73.1
1050	79.3
1100	86.8

2.4.3 Temperature and current distribution

Spatial temperature and current distributions and their evolution in the SPS setup for the alumina and copper samples are discussed in this section. Investigating the temperature distribution in the SPS sample is important as the temperature gradient in the sample can affect the sample uniformity. Again, the temperature distribution is related to the current distribution due to the fact that heat generated in the system is totally resistive and is the only heat generation process in the setup. The temperature, electric current density (ECD), heat flux vector and electric potential distribution at different parts of the SPS system at the end of 600 seconds of heating cycle for both the conductive (copper) and non-conductive (alumina) samples are discussed here. 1000A current was taken as the reference input current. The sample and tool geometry considered in this study have the reference dimensions as indicated in Table 2.1.

Fig. 2.34 shows the temperature contour plot in the whole SPS system for the both alumina and copper samples in a 3d cut view and Fig. 2.35 shows the temperature contour plot in the punch-sample-die-small spacer assembly in an axisymmetric cut view. In the remaining part of this thesis, we will show temperature and current contour plots in axisymmetric cut view, as it is easy to understand and analyze. The maximum temperature in the setup was generated in the punch; more specifically the portion of the punch that is not enclosed by the die (Fig. 2.34-2.35). This area has the smallest cross section in the setup and consequently, the highest resistance. ECD in this portion of the punch was also the highest as all the current had to pass through this small section (Fig. 2.36). This high resistance area produced maximum resistive heating which was partially diffused into the sample-die and partially lost into the upper and lower spacers, which are water-cooled. In addition, heat was also lost by radiation from the exposed punch surfaces to the vacuum. That is why the highest temperature can only appear in the punch at the center of axial symmetry. On the other hand, the temperature in the spacers was quite low compared with punch and they mainly acted as heat sinks that took away heat from the punch.

The heat flux vector distribution contour (Fig. 2.37) shows the direction of heat flow from punch to sample-die and spacers.

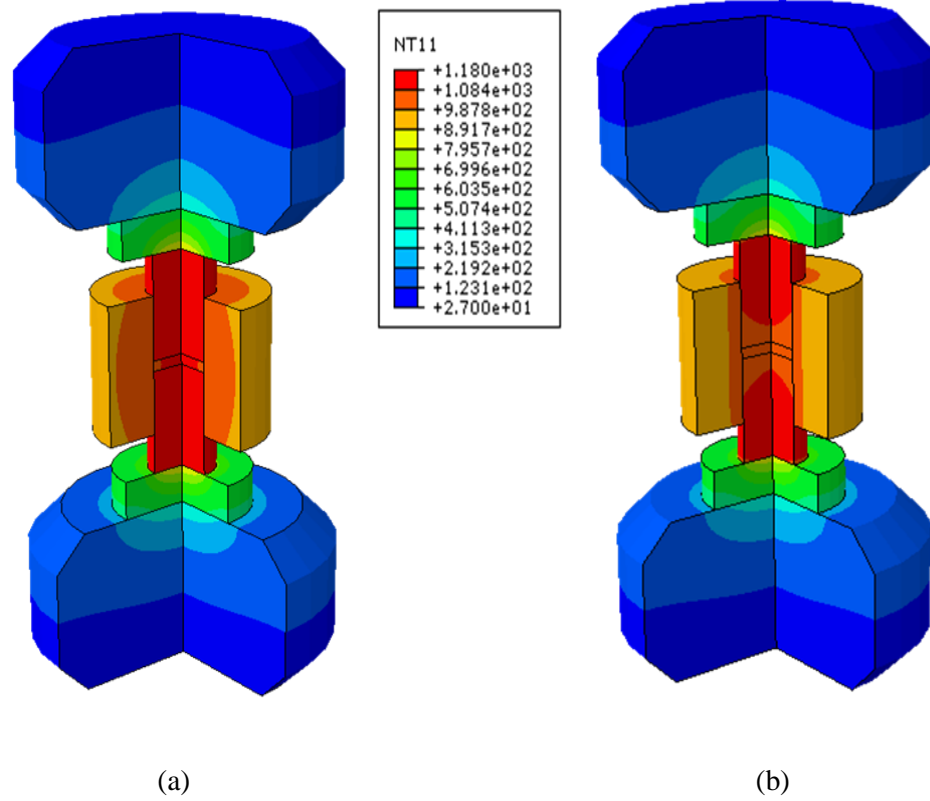


Fig. 2.34: Temperature contour plot in the whole SPS system in a 3d view: (a) alumina and (b) copper

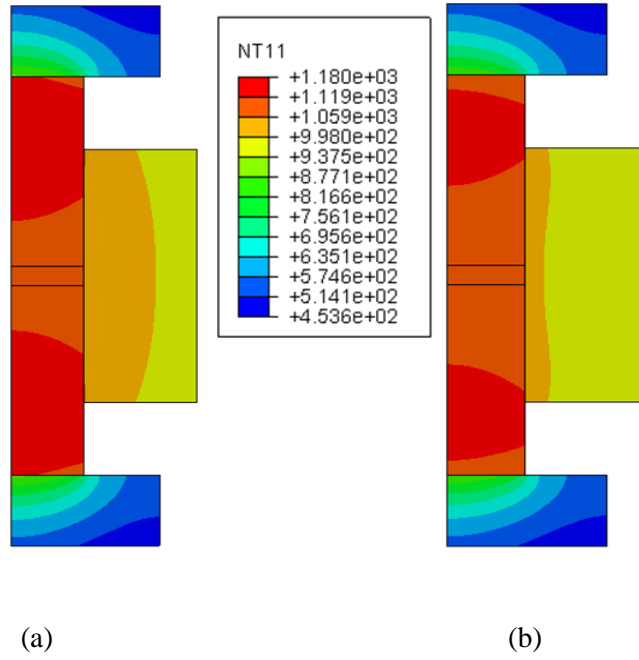


Fig. 2.35: Temperature contour plot in the SPS system in an axisymmetric cut view: (a) alumina and (b) copper

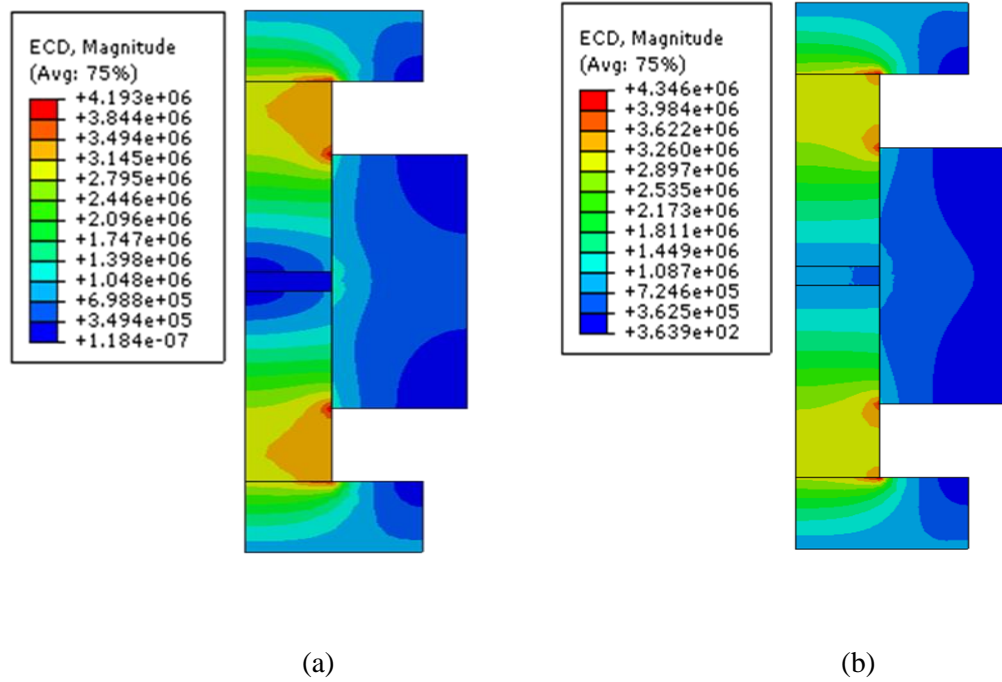


Fig. 2.36: ECD contour plot in the SPS system: (a) alumina and (b) copper

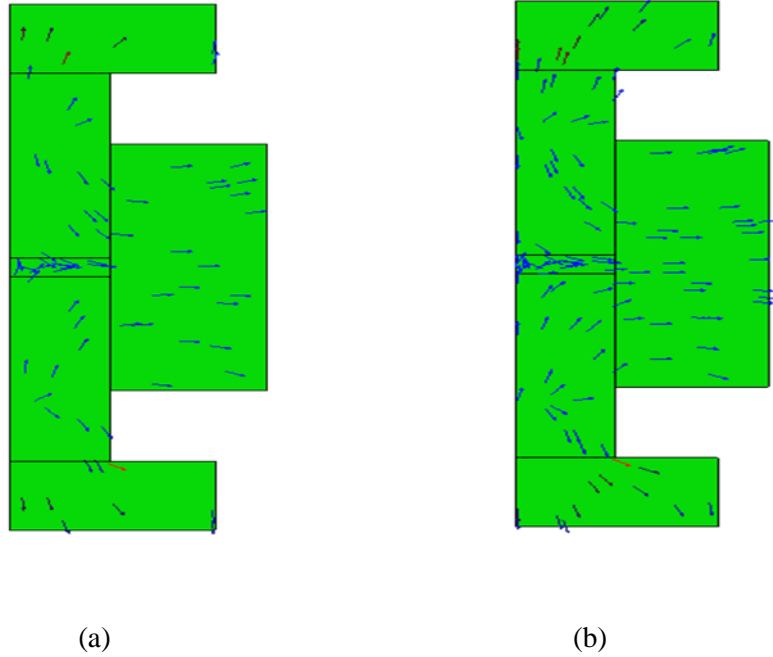


Fig. 2.37: Heat flux vector distribution in the SPS setup: (a) alumina and (b) copper

There are differences in temperature distribution for the alumina and copper samples. It happens due to the difference in current flow mechanism in two samples. In case of the non-conductive alumina sample, current cannot pass through it. The current is rather forced to pass through the die in a tortuous path to complete the current circuit. Fig. 2.36 confirms it showing an ECD of only 10^{-7} A/m² inside alumina sample which is negligible. It suggests that heating in non-conductive sample is not due to joule heating inside the sample rather heat conduction from punch. On the other hand, current flows very easily through the conductive copper sample. The ECD in copper was quite high; in fact higher than the die (Fig. 2.36). As the conductivity of copper is very high, the current hardly experiences any resistance on its path. There was hardly any potential drop across the copper sample. This means resistive heating inside copper sample is not also significant. Even in case of conductive sample, the major portion of the heat came from conduction from the punch.

The SPS system with alumina sample generated higher temperature than system with copper sample. Maximum temperature in the alumina and copper sample were 1095.6° C and 1066.4° C respectively. Temperatures in punch and die surface in the SPS system with alumina were higher than those temperatures in SPS system with copper sample. Higher heat generation in the nonconductive sample system can be explained in terms of overall system resistance. The electric potential distribution in the system for two samples is shown in Fig. 2.38. It is seen that the overall potential drop across the system's two end surfaces for copper sample is less than that for alumina sample. Higher potential drop refers to higher overall system resistance. Because of higher system resistance, higher temperature is found in alumina sample system. The ECD inside the die was higher in case of alumina sample as all the current passed through the die and nothing through the sample. Higher ECD in die resulted in higher joule heat generation and consequently higher temperature in die. Higher heat capacity of alumina could be another reason for higher temperature in alumina sample than copper sample.

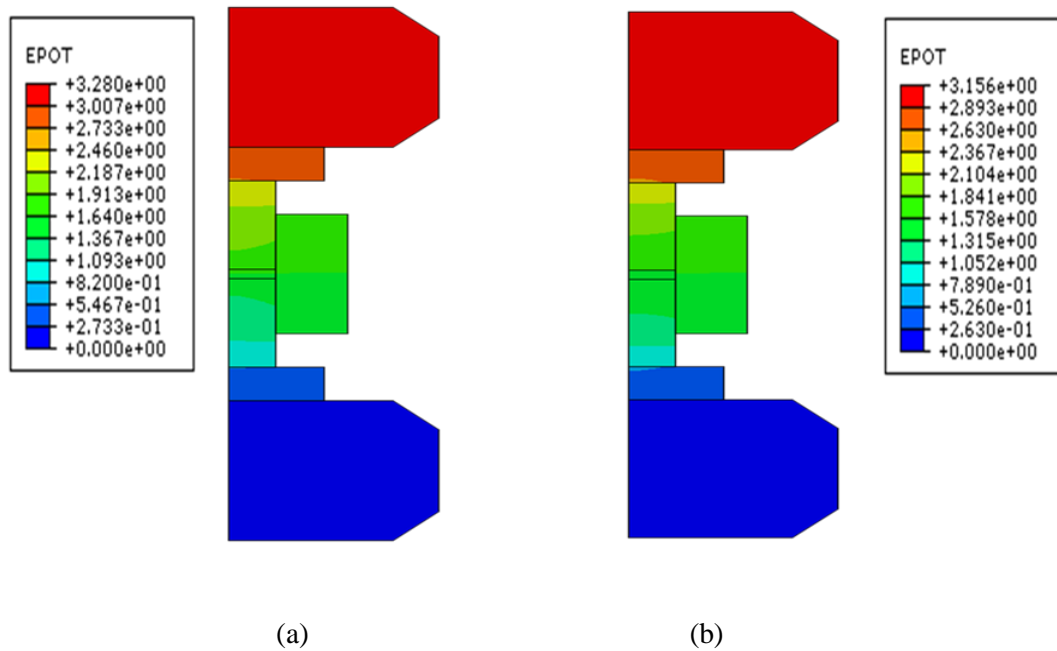


Fig. 2.38: Electric potential distribution in the SPS system: (a) alumina and (b) copper

Fig. 2.39 shows the temperature contours only in the alumina and copper samples at the beginning (1s) and at the end (600s) of heating cycle. In the case of non-conductive alumina sample, at the beginning, heat comes into the sample from the punch-sample-die corner section through conduction. It happens because at that section some current crowding occurs, as the current passing through the punch cannot pass through non-conductive sample and suddenly needs to follow a tortuous path through the die. The heat generated in the exposed punch area takes some time to be conducted to the sample, and before that can happen the heat generated in the site of current crowding reaches the sample through the corner. This results in a temperature distribution as depicted in Fig. 2.39. That is why the center is cooler than the sides in the alumina sample at the beginning. After the initial few seconds, heat from the punch conducts into the sample through sample top and bottom surfaces and makes the sample center hotter than the sides. In the case of copper sample, it is seen that at the beginning (1s) the top and bottom sample surface gets heated first rather than the sides unlike the alumina sample. Most of the current in the copper sample passes straight through the sample and current crowding effect at the corners is less. With the increase of time, the sample (both alumina and copper) temperature gets higher than the die and heat starts to flow from sample to die.

Temperature distributions in axial and radial direction inside the samples are shown in Fig. 2.40. There was hardly any temperature gradient in the axial direction for both the samples. The difference in temperature between sample top and center were 0.9°C and 0.17°C for alumina and copper respectively. Temperature gradient in the radial direction was more significant than in the axial direction for both alumina and copper sample. However, there were some differences in radial temperature distribution between the conductive and non-conductive samples. A radial temperature gradient of 27.5°C was found in the alumina sample, which was only 2.9°C in the copper sample. Heat is conducted away from the sample to the die in the radial direction, which causes temperature gradient in radial direction. This radial temperature gradient in alumina

sample can cause non-uniformity in microstructure and properties. The difference in temperature gradient between the two samples comes from their difference in thermal property and current distribution. High thermal conductivity and low specific heat of copper sample enables it to conduct heat away to the die quickly which results in smaller temperature gradient in radial direction. The opposite is true for alumina. Being a poor conductor the alumina sample loses heat slowly and its high specific heat enables it to store heat energy longer than copper. This results in higher temperature and larger radial temperature gradient in alumina sample.

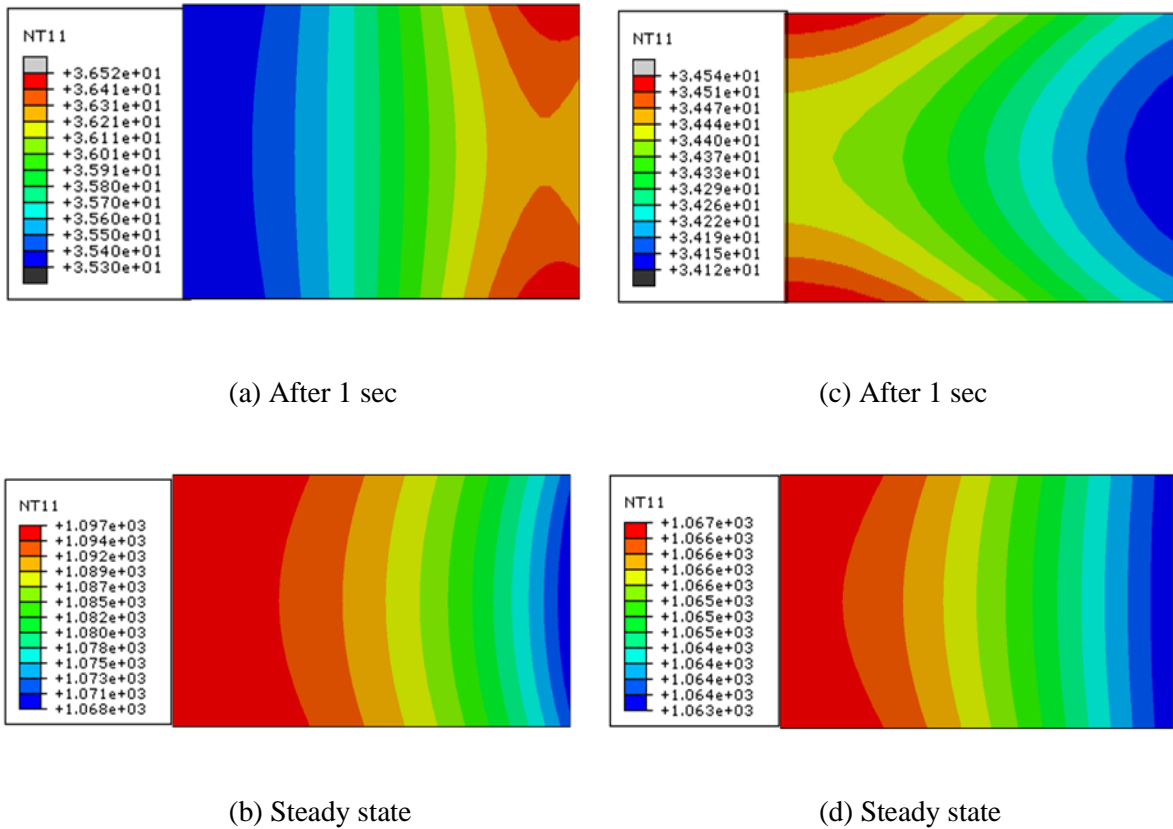


Fig. 2.39: Temperature distribution inside the sample respectively after 1 sec and steady state: (a), (b) alumina and (c), (d) copper

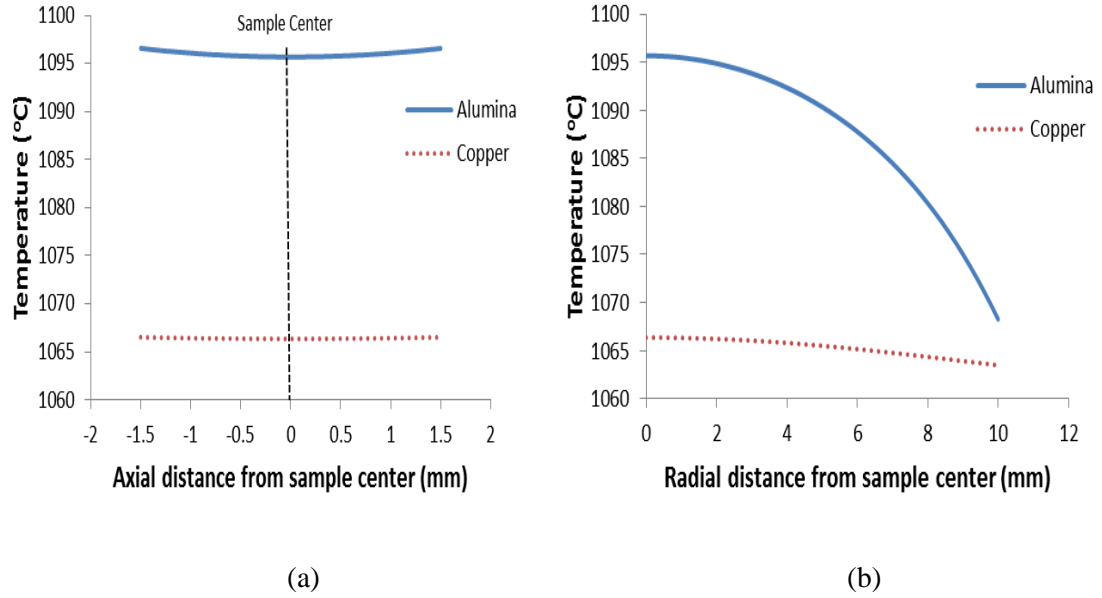


Fig. 2.40: Temperature distribution in alumina and copper sample: (a) axial and (b) radial direction

Fig. 2.41 shows the temperature and electric current density (ECD) distribution in sample-die assembly for the alumina and copper samples. Temperature at the sample center was higher than the die surface. It was seen that, for the copper sample, ECD was higher in the sample than in the die, as more current passed through the sample. Since ECD in the die was lower in this case as compared with the alumina sample system, the die surface temperature for the copper sample was lower than that for alumina sample (Fig. 2.41 (a)). However, the temperature difference between sample center and die surface was found to be almost the same for both the alumina and copper samples for the sample and tool dimensions considered here. The difference was 114.31°C for the alumina and 114.1°C for the copper sample. Fig. 2.42 shows the ECD and temperature distributions in punch-sample-punch assembly for the alumina and copper samples. The maximum temperature was found in the middle section of the exposed portion of the punch whereas the maximum ECD was found close to the spacer-punch interface because of high

current crowding near the interface. Maximum temperature in the punch was higher for alumina sample (1179° C) than in copper sample (1147° C).

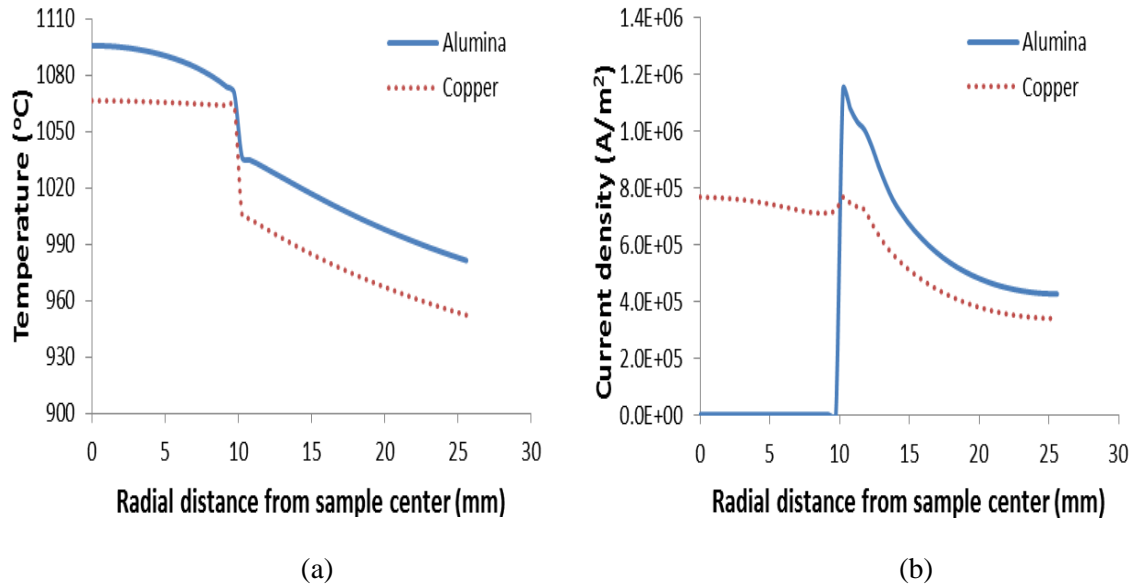


Fig. 2.41: (a) Temperature and (b) ECD distribution in sample-die for alumina and copper

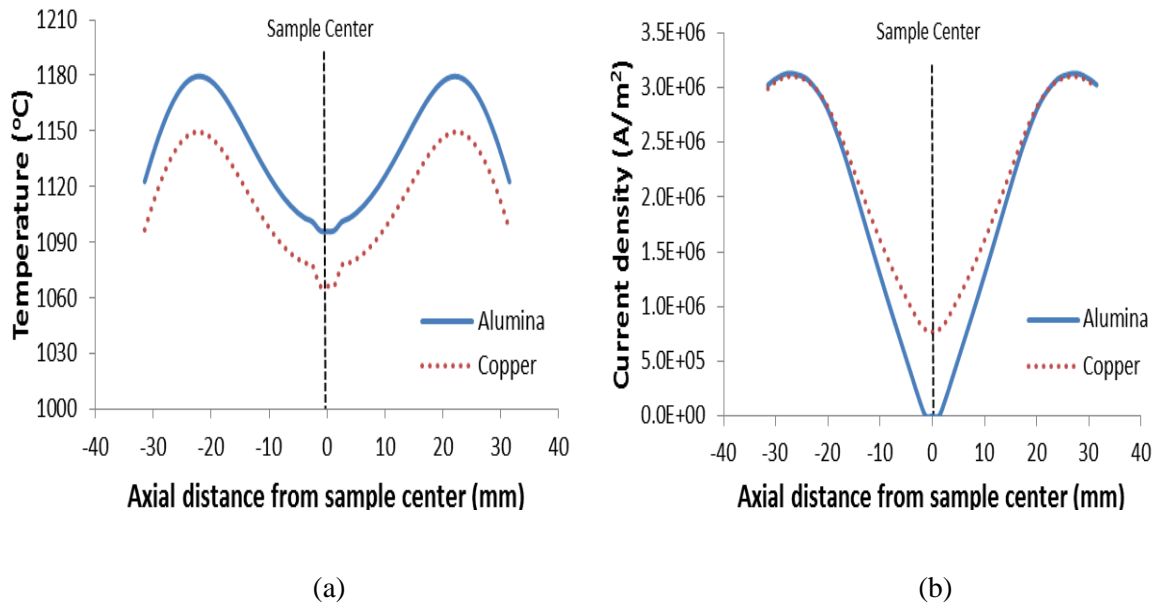


Fig. 2.42: (a) Temperature and (b) ECD distribution in punch-sample-punch for alumina and copper

2.5 Conclusion

In this chapter, a coupled thermal-electrical model was developed for SPS process. In order to determine the electrical and thermal contact resistance of the system, an integrated experimental-numerical methodology was followed. The accuracy of the model was evaluated for graphite cylinder and alumina powder sample. In both cases, the model showed very good agreement with the experimental results.

The developed model was implemented to analyze the temperature and current distribution in two different types of materials – non-conductive alumina and conductive copper. The material properties had great influence on the temperature distribution in the sample. It was seen that the temperatures in the sample as well as in the sintering tools were higher for non-conductive sample than for conductive sample. The non-conductive alumina sample had large temperature gradients which could result in non-uniform property in it. Temperature gradient in radial direction was more severe than in axial direction. Difference in thermal properties such as conductivity and specific heat as well as electric current flow path in the two samples was the main reasons for their temperature difference. In case of the alumina sample, the current did not pass through the sample rather followed a tortuous path through the die unlike the copper sample where high density current flowed through it. Joule heating inside both the samples was low and samples mainly got heated by heat conducted from the punch. Highest temperature in the system was always generated in the punch, and the die surface temperature was always lower than the sample. The developed model gives a great insight to temperature distribution and evolution in the SPS system. This developed model will be utilized in Chapter 3 to determine the importance of the process parameters on the temperature distribution in the sample in SPS system.

CHAPTER III

IMPORTANCE OF THE PROCESS PARAMETERS IN SPS

3.1 Introduction

In the literature, most of the numerical studies predominantly attempted to develop a reliable sintering model for temperature and current distribution only. In chapter 2, we developed a coupled thermal-electric model for spark plasma sintering (SPS) process and validated the model experimentally. We found that the material properties played a key role in temperature and current distributions. The tool geometry and process control parameters can also play an important role in those distributions. However, the importance of SPS tool geometry and process control parameters was not studied with importance in the literature. In this chapter, we utilize our developed model to study the importance of tool geometry and process control parameters on temperature and current distributions in SPS process. Different sizes (both height and diameter) of samples, punches, and dies are considered. The importance of the symmetric position of the punch and die on sample temperature distribution is also studied. In addition to that, how the different process control parameters such as sintering temperature, input current, and the use of graphite insulation around the die can influence the temperature distribution are also discussed. The results of this study can be used for SPS system design and process optimization for different kinds of materials according to the needs. This study could also prove very useful for the production of large size sintered samples with controlled and tailored properties.

3.2 Method

In chapter 2, we did the experimental validation of our model with some specific sample and tool geometry (Table 2.1). In this chapter, we have taken that geometry as our reference and varied the dimensions of the sample and the tools around those reference values. We varied the parameters in a limited range to investigate the influence of different parameters on temperature and current distributions. In a few cases, some of the parameters are interrelated. As an example, die thickness is usually changed with the sample diameter to give the die sufficient physical strength. Thus, the changes in sample diameter and die thickness are closely related. However, in order to find the effect of each parameter individually, we changed one parameter while keeping the others unchanged. Three different values of each parameter were chosen to show the effect of both increasing and decreasing the parameter. Table 3.1 shows all the values of the parameters along with the reference values chosen for this study. The importance of tool geometry and process control parameters on temperature and current distributions was studied for both alumina and copper samples. The input current for all the cases was taken as 1000 A; except the case where the effect of different input current was studied. The contact resistances and all other initial and boundary conditions were the same as those used in chapter 2. Mesh density and solution technique were also unchanged.

Table 3.1: Studied parameters influencing temperature and current distribution

Process parameters	Reference value	Studied values
Sample diameter	20 mm	10 mm, 20mm, 30 mm
Sample thickness	3 mm	3 mm, 6 mm, 9 mm
Punch length	30 mm	25 mm, 30mm, 35 mm
Die thickness	15 mm	10 mm, 15 mm, 20 mm
Die height	40 mm	35 mm, 40mm, 45 mm
Relative position of punch-die	Symmetric	Symmetric, die moved 2mm upward, die moved 4 mm upward
Upper punch length	30 mm	30 mm, 27 mm, 24 mm
Input current	1000 A	1000 A, 1100A, 1200 A

3.3 Results and discussion

3.3.1 Effect of sample diameter:

One of the first considerations while making samples by SPS is the sample diameter. With the change of sample diameter, other parameters like, punch diameter and die internal diameter also change. Usually, the die thickness is changed with the change in sample diameter to give the die sufficient physical strength. Thus, the changes in sample diameter and die thickness are closely related. However, to find the effect of changing the sample diameter only, we kept the die thickness the same (15 mm) for all the cases considered here while changing the die inner and outer diameter to match with the sample diameter. The sample diameters considered here were 10 mm, 20 mm and 30 mm.

As the sample diameter was reduced from 20 mm to 10 mm, there was drastic change in system temperature. All the parts – sample, punch, and die showed rapid increase in temperature (Fig. 3.1-3.3, 3.5). Maximum sample temperature increased by about 764° C in alumina and 790° C in copper sample (Fig. 3.1). The maximum temperature of the alumina sample (1870° C) was higher than that of the copper sample (1856° C) as expected. Axial temperature gradients of 10° C and 0.8° C were found in the alumina and copper samples respectively (Fig. 3.1). The temperature gradients in radial direction inside the alumina sample increased greatly due to the reduction in sample diameter although the change of radial temperature gradient in the copper sample was not very substantial (Fig. 3.2). A radial temperature gradient of 69° C was found in the alumina sample, which was 4° C in the copper sample. Fig. 3.3 shows the temperature distribution in sample-die for the alumina and copper samples respectively. Large temperature gradient (around 450° C) existed in sample-die assembly along the radial direction when sample diameter was 10 mm. The current density distribution in sample-die is shown in Fig. 3.4 as a function of sample diameter. Fig. 3.4(b) shows an extremely high current density in the 10 mm diameter copper sample which drops sharply in the die portion. On the other hand, the current density near the sample-die interface of the 10 mm alumina sample is quite high which compensates for zero current flow in the alumina sample (Fig. 3.4(a)).

The increase in punch temperature was relatively higher than other parts (Fig. 3.5). The maximum temperature in punch rose up to 2793° C and 2780° C for the 10 mm diameter alumina and copper samples respectively, which was about 1600° C greater than the highest temperature in punch for the 20 mm diameter samples. Another difference observed here was the position of maximum temperature in punch, which moved close to the punch-spacer interface for the 10 mm diameter samples. As the diameter was reduced from 20 mm to 10 mm, the cross sectional area reduced by a factor of 4 and since the total applied current was still the same, it created very high current density at the exposed areas of the punch. In addition to that, the current crowding at the

spacer-punch interface was also extremely high (Fig. 3.6). All these are responsible for extremely high temperature at punch. High heat generation in punch also increased the temperature in sample and die.

On the other hand, when the sample diameter was increased to 30 mm, the overall temperature in the system went down (Fig. 3.1-3.3, 3.5). The maximum temperature in the system was generated at the sample-punch interface, which were 634° C for the alumina sample and 593° C for the copper sample (Fig. 3.5). Temperature gradient in the whole system reduced to some extent. Even for the alumina sample, there was almost no temperature gradient (only 1° C) in radial direction inside the sample, which was about 28° C for the 20 mm diameter sample (Fig. 3.2). This time the temperature at the sample edge (635° C) was slightly higher than sample center (634° C). However, there was no such change in the case of the copper sample; the sample center was always hotter than the edge. Similar incident was observed by Munoz *et al.* [114] when they increased their non-conductive and conductive sample diameter above 30 mm. The temperature difference between the sample center and die surface also decreased for both the conductive and non-conductive samples. This temperature difference between the sample center and die surface was 14° C for the alumina and 26° C for the copper samples (Fig. 3.3).

A comparatively uniform temperature distribution was found both in axial and radial direction as a result of increasing the sample diameter. When the sample diameter is increased, punch diameter is also increased. This results in low current density in the punch area and consequently lower heat joule heat generation in punch. The external punch and die surface areas exposed to radiation also increase with the increase in sample-punch diameter, which allows more heat loss to the vacuum by radiation. All these factors result in overall low temperature and small gradient in the system.

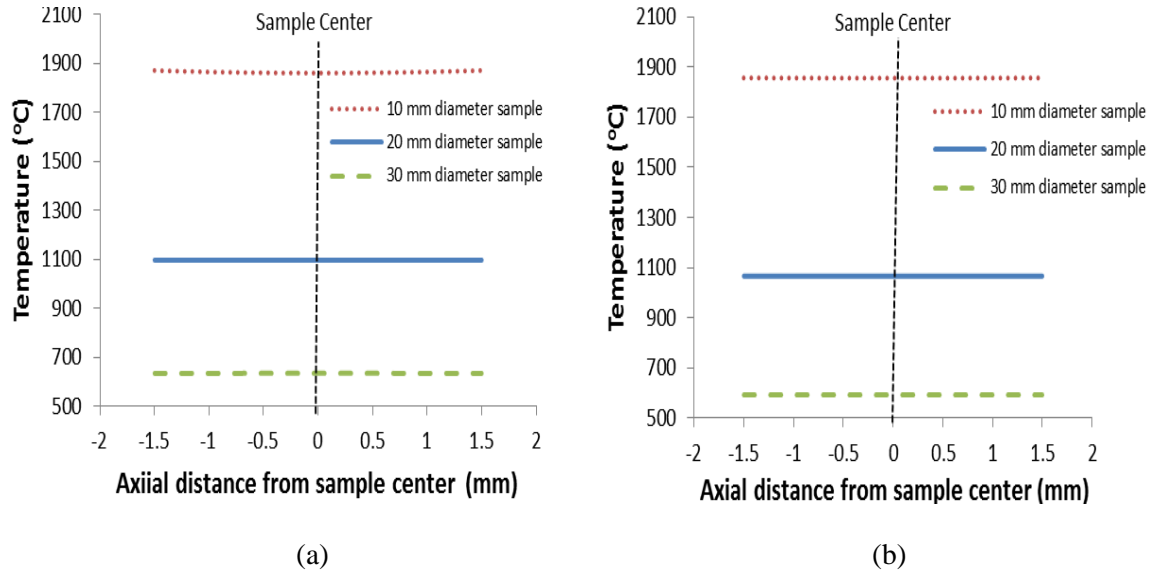


Fig. 3.1: Temperature distribution in axial direction as a function of sample diameter: (a) alumina and (b) copper

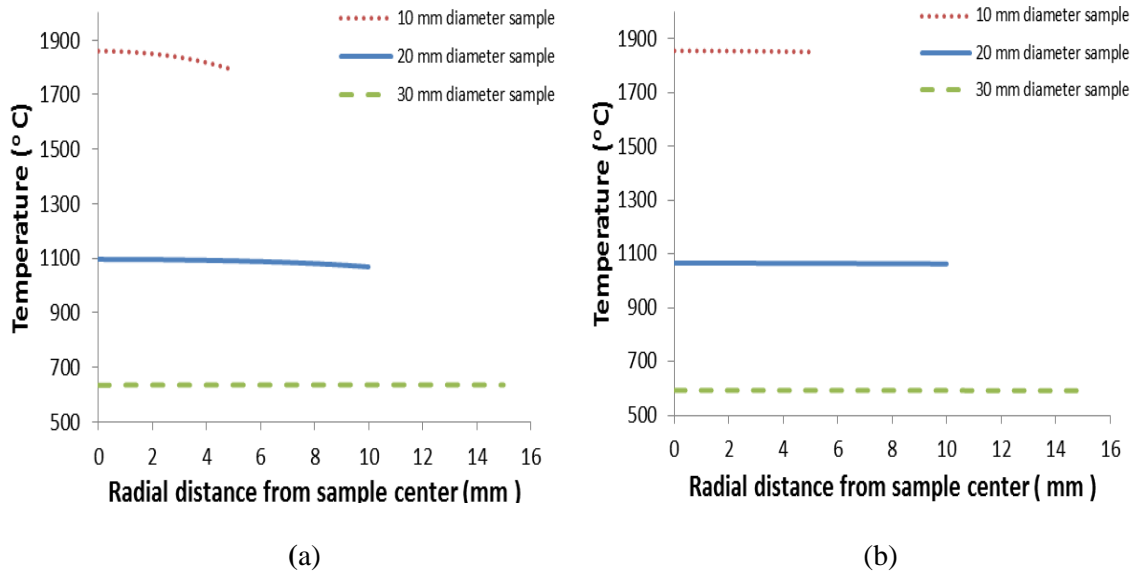
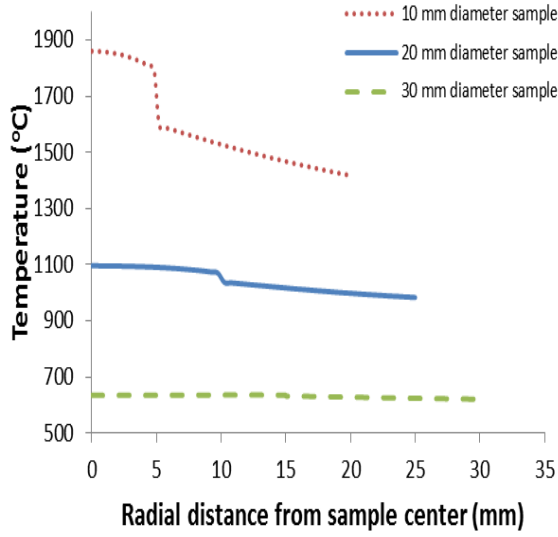
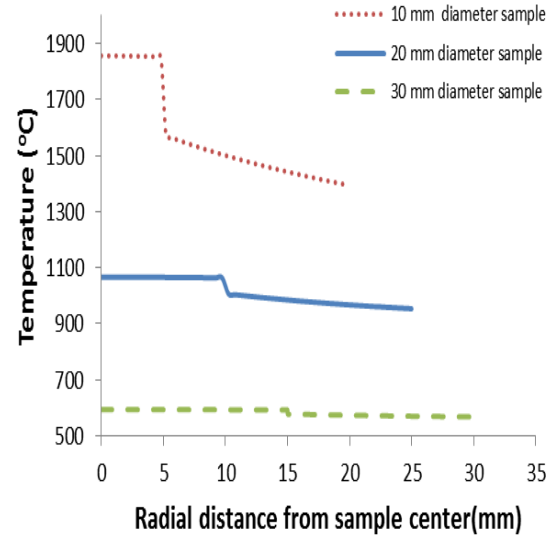


Fig. 3.2: Temperature distribution in radial direction as a function of sample diameter: (a) alumina and (b) copper

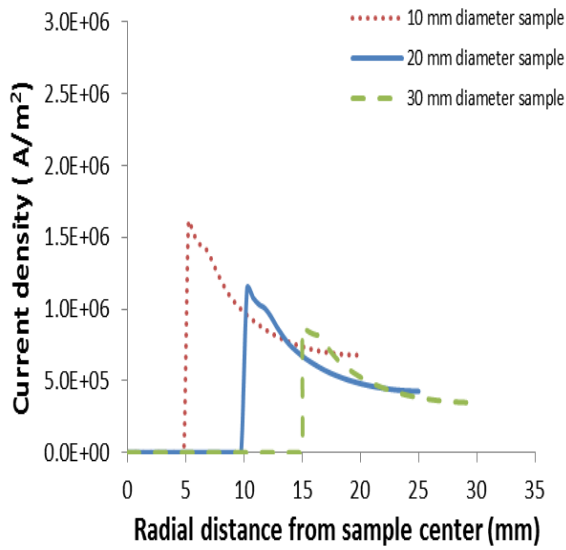


(a)

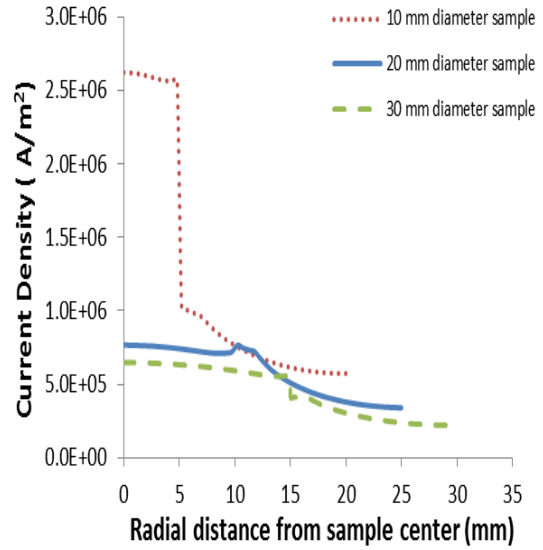


(b)

Fig. 3.3: Temperature distribution in sample-die as a function of sample diameter: (a) alumina and (b) copper



(a)



(b)

Fig. 3.4: Electric current density distribution in sample-die as a function of sample diameter: (a) alumina and (b) copper

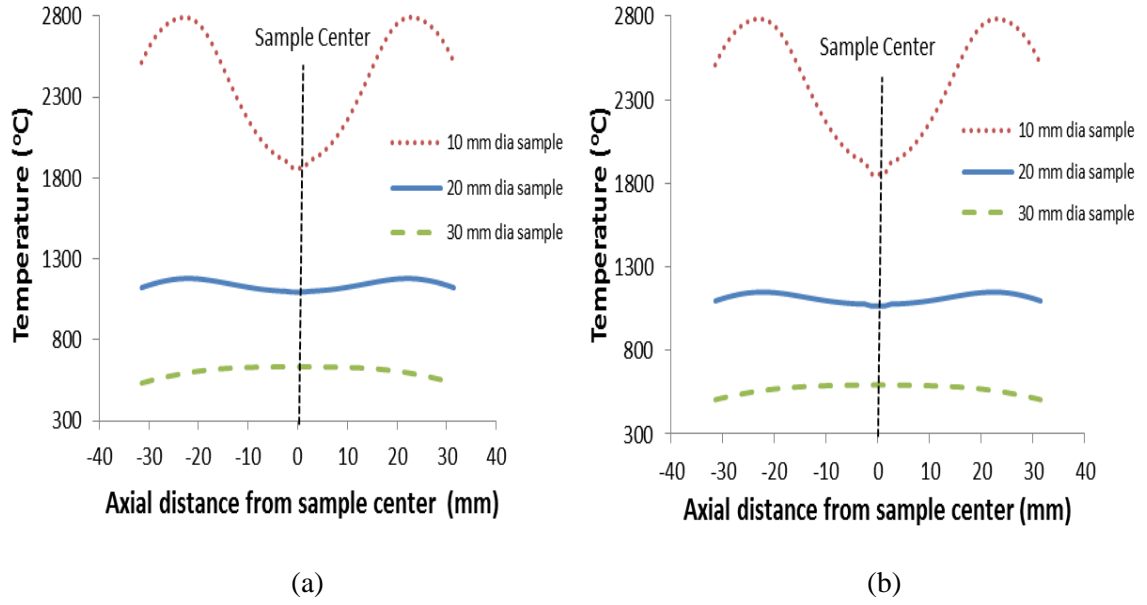


Fig. 3.5: Temperature distribution in punch-sample-punch as a function of sample diameter: (a) alumina and (b) copper

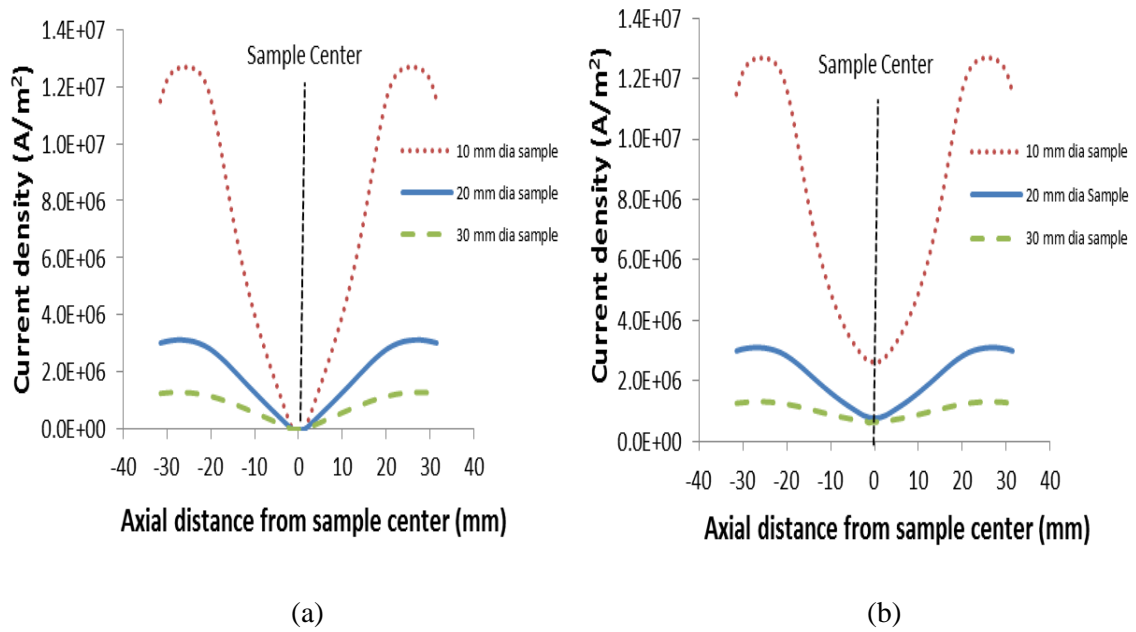


Fig. 3.6: Electric current density distribution in punch-sample-punch as a function of sample diameter: (a) alumina and (b) copper

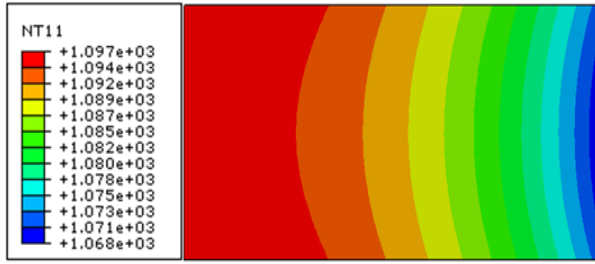
3.3.2 Effect of sample thickness

Although the sample volume is very small compared with other parts in the SPS system, small change in the sample thickness can significantly alter the temperature and current distribution in the system. Fig. 3.7 shows the temperature contour plot inside the sample for different sample thicknesses (3mm, 6mm and 9mm) for both alumina and copper samples. There was an increase in maximum temperature in sample with the increase in sample thickness. For an increase of sample thickness from 3 mm to 9 mm, the maximum temperature in alumina sample increased by 38° C whereas for the same increase of copper sample thickness, the maximum temperature in sample increased by 11° C. As it is seen from the Fig. 3.7, the temperature distribution also became more non-uniform with the increase of sample thickness. Temperature gradients were seen both in axial and radial direction (Fig. 3.8-3.9). It should be noted here that axial temperature gradient was very much negligible for both alumina and copper when the thickness is 3 mm. When the sample thickness was increased from 3mm to 9 mm, the axial temperature gradient increased from 1° C to 12° C for alumina. There was a temperature gradient of only 1° C in the axial direction inside the copper sample when the thickness was increased to 9 mm (Fig. 3.8). However, radial temperature gradient was not affected to a noticeable extent for the change of sample thickness for both conducting and non-conducting sample (Fig. 3.9). It happened as no change in dimension or any other system property was made in the radial direction. The radial temperature gradient mostly results from radiation heat loss from the die surface, which did not change with the change in sample thickness. On the other hand, the axial temperature gradient is attributed to electrical and thermal response of the sample. The difference between maximum and minimum temperature inside the alumina sample increased from 27° C to 42° C when the sample thickness was increased from 3 mm to 9 mm. Although the temperature non-uniformity increased with sample thickness in the copper sample, the difference between maximum and minimum temperature in the copper sample did not change (Fig. 3.7). Another

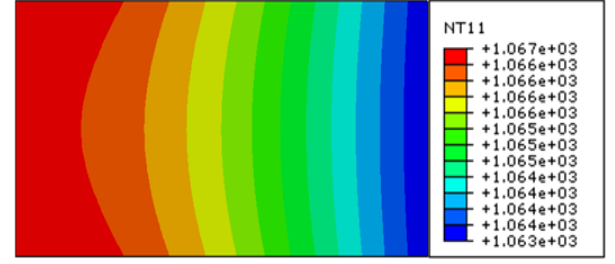
important observation is that the maximum temperature in the sample was no longer found in sample center when the thickness was increased, rather it was found at the center of top and bottom surface (Fig. 3.7). This happened because most of the heat flows into the sample from the punches through the sample top and bottom surfaces. As the thickness increases, the distance between the sample center and sample outer surfaces increases and as a result, the temperature at the center of thicker samples is less than the sample outer surfaces.

Fig. 3.10 and 3.11 show the temperature and current density distributions in sample-die for various thicknesses of the two samples. There was an increase in die surface temperature with the increase in sample thickness (Fig. 3.10). As the sample thickness increases, the exposed surface area of the punch increases. This part of the punch in the SPS system has the smallest diameter and consequently, it is the main joule heat generation site. The length of this part increases with the increase in thickness that causes an overall increase in temperature of the system. The current density distribution along the radial direction in sample-die reveals some interesting facts (Fig. 3.11). The current passing through the conducting copper sample increased sharply with the increase in sample thickness. Average current density in the copper sample increased by 27% when the thickness was increased from 3mm to 9 mm. As more current passed through the sample, the current density in the die decreased in this case. On the other hand, there was no noticeable change of electrical property inside the alumina sample. Although the total amount of current passing through the die did not change, the current density in the die near the die-sample interface decreased while this current density increased further away from the interface with the increase of sample thickness. Current crowding occurs near the top surface of the sample inside the die because of sudden change in current path. This current crowding along with contact resistances influences the current density near the interface. As the sample thickness increased, the distance from the die center sections (the section from where data points are taken) to the location where the current crowding occurs increased. This could be a reason why there

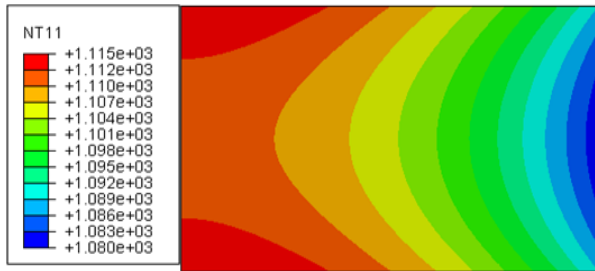
was a decrease in current density near the interface with the increase in sample thickness. The temperature difference between the sample center and die surface did not change significantly with the change in sample thickness. Surprisingly this difference in temperature between the two points decreased a bit for both samples. Fig. 3.12 and 3.13 show the temperature and current density distribution in punch-sample-punch for the three sample thicknesses considered here. The maximum temperature in the punch increased by about 50° C and 40° C respectively for the alumina and copper samples as the thickness was increased from 3 mm to 9 mm. As mentioned earlier, this increase in temperature was due to the increase in exposed punch area where majority of the joule heat is generated.



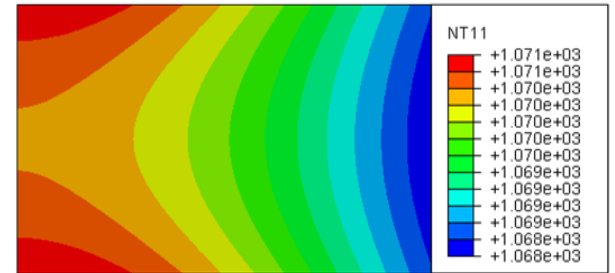
(a) 3 mm alumina sample



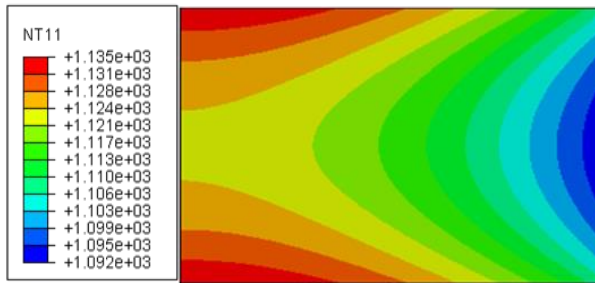
(d) 3 mm copper sample



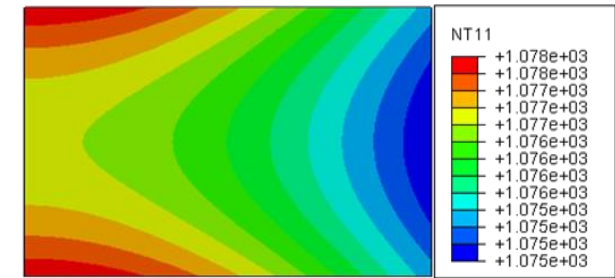
(b) 6 mm alumina sample



(e) 6 mm copper sample



(c) 9 mm alumina sample



(f) 9 mm copper sample

Fig. 3.7: Temperature contour plot in samples as a function of sample thickness: (a-c) alumina, and (d-f) copper

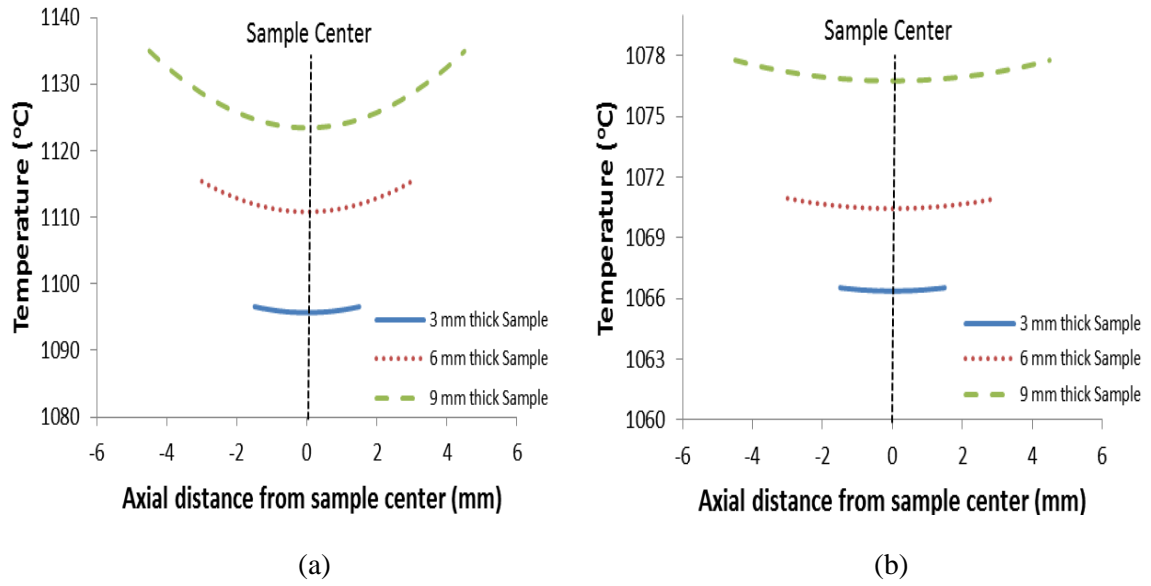


Fig. 3.8: Temperature distribution in axial direction in the sample as a function of sample thickness: (a) alumina and (b) copper

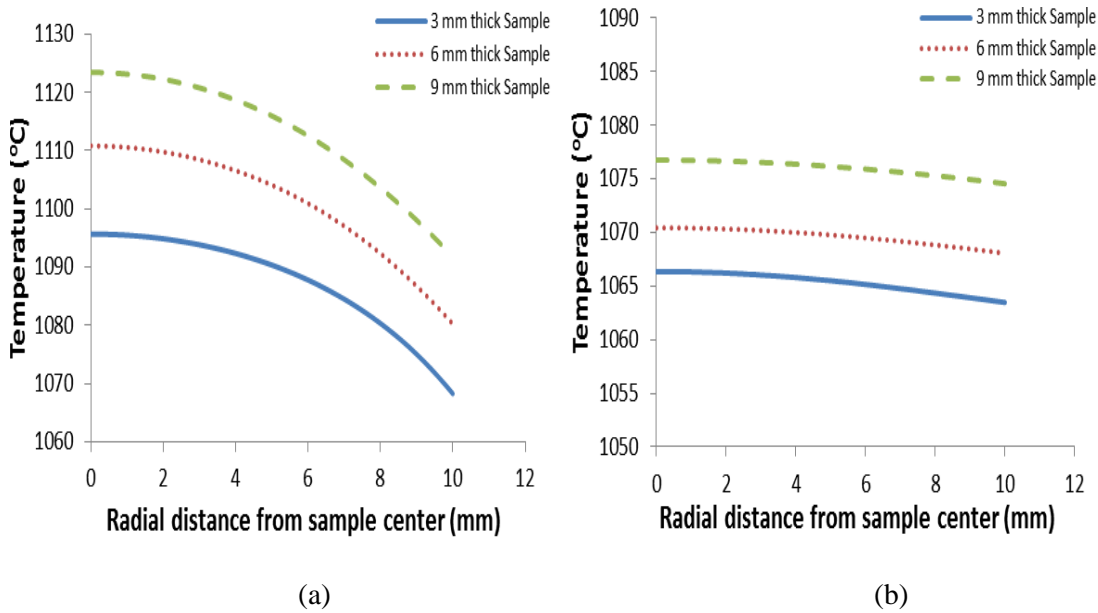


Fig. 3.9: Temperature distribution in radial direction in the sample as a function of sample thickness: (a) alumina and (b) copper

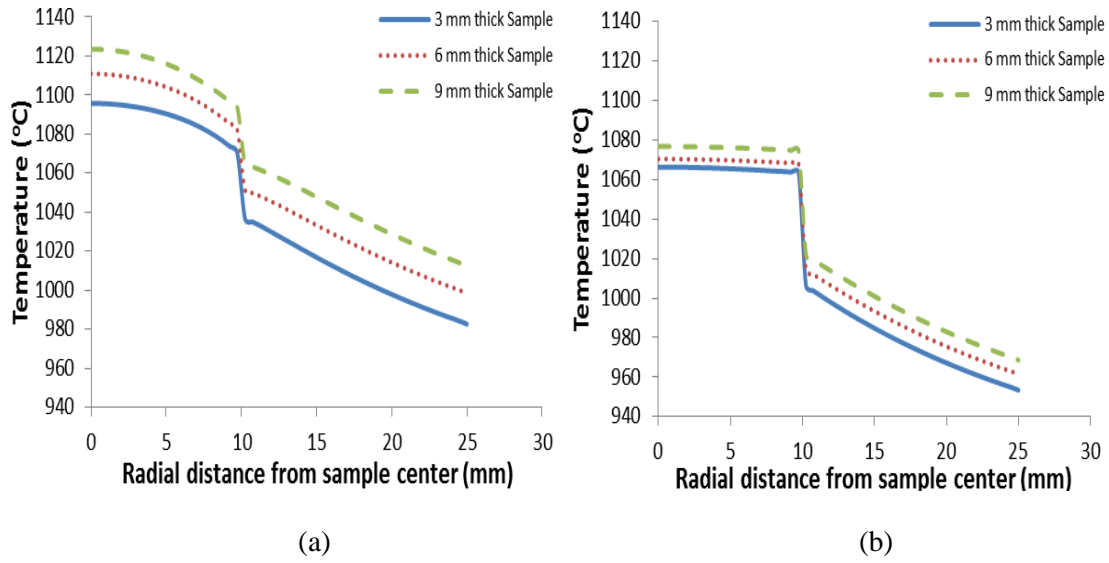


Fig. 3.10: Temperature distribution in sample-die as a function of sample thickness: (a) alumina and (b) copper

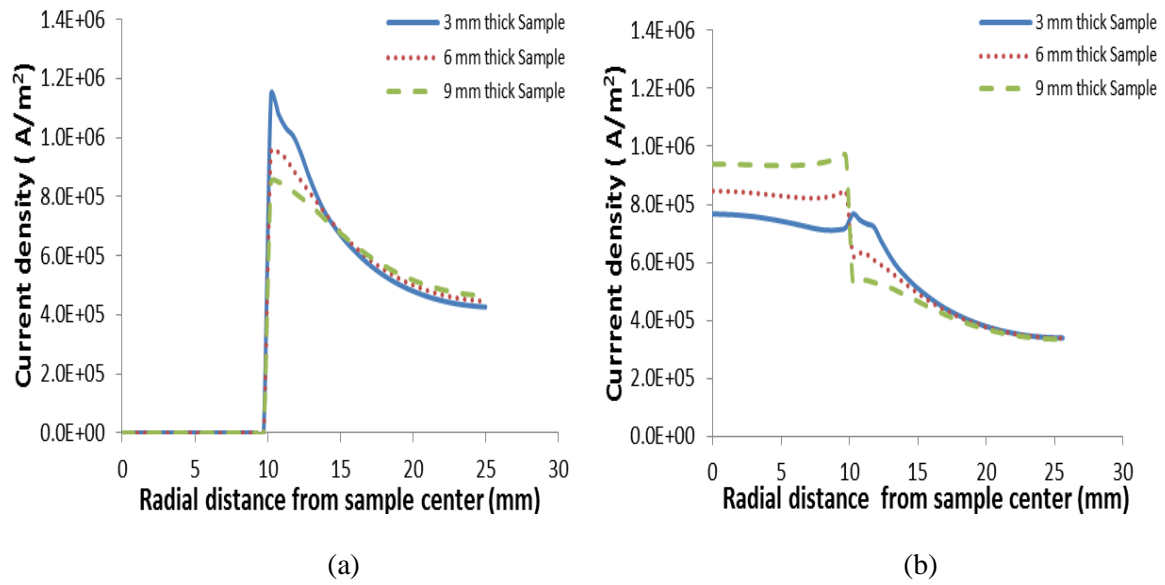


Fig. 3.11: Electric current density distribution in sample-die as a function of sample thickness: (a) alumina and (b) copper

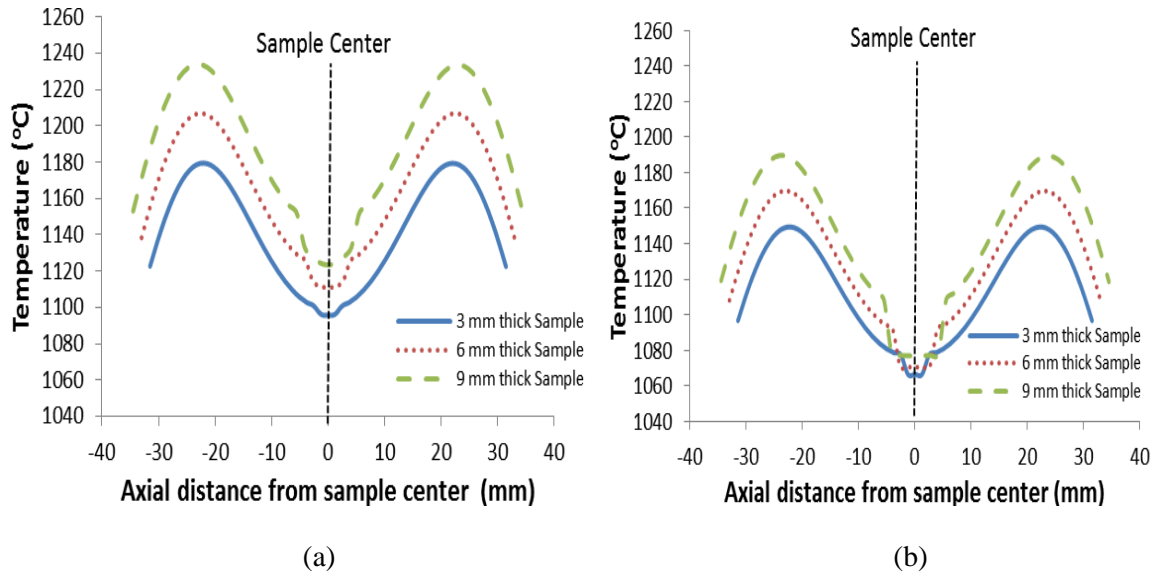


Fig. 3.12: Temperature distribution in punch-sample-punch as a function of sample thickness: (a) alumina and (b) copper

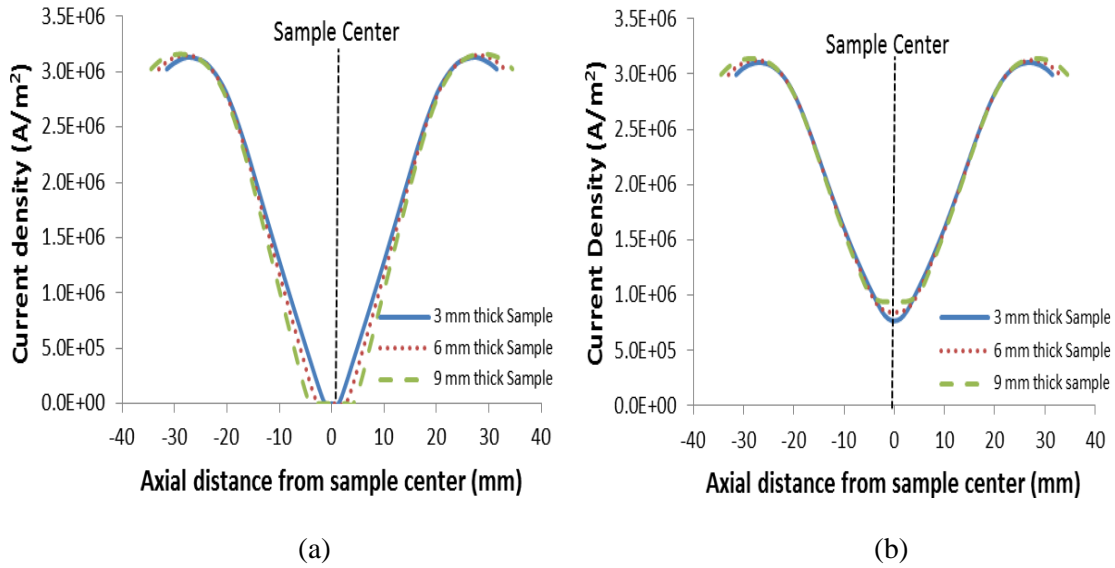


Fig. 3.13: Electric current density distribution in punch-sample-punch as a function of sample thickness: (a) alumina and (b) copper

3.3.3 Effect of die thickness

Die dimensions could also play an important role in temperature distribution of the SPS setup. First, the influence of die thickness is considered. Three different die thicknesses- 10mm, 15mm and 20 mm are studied. As the heat from the sample and punch are taken away by the die, the die thickness influences the temperature distribution in the whole system by increasing or decreasing the amount of radiation from its surfaces. An increase in die wall thickness means an increase in external die surface area, which can radiate the heat away to the vacuum chamber. There will be more radiation heat loss, which would decrease the temperature in sample and punch.

Temperature distributions in axial and radial direction in the alumina and copper samples as a function of die thickness are shown respectively in Fig. 3.14 and 3.15. The maximum temperature in sample decreased by 119° C and 116° C respectively for the alumina and copper samples as a result of increasing the die thickness from 10 mm to 20 mm. Although the temperatures increased or decreased because of decreasing or increasing the die thickness, its effect on axial or radial temperature gradient is minimal. The radial temperature gradient in the alumina sample increased from 24.5° C to 30° C as the die thickness increased from 10 mm to 20 mm whereas the radial temperature gradient in the copper sample increased from 2.8° C to 3° C for the same change in die thickness. The temperature gradient in axial direction was even more negligible.

The temperature and current profile in sample-die assembly for the alumina and copper samples are shown in Fig. 3.16 and 3.17 respectively. The temperature decreased more in the die outer surface than in the sample and punch as the die thickness was increased. A temperature drop of about 150° C was observed for both the alumina and copper samples as the die thickness was increased from 10 mm to 20 mm. However, the difference in temperatures between the

sample center and die outer surface increased as the die got thicker (Fig. 3.18). This change was more significant for the alumina sample (95° C to 135°C) than the copper sample (100° C to 129° C). In the case of alumina, which is a non-conductive sample, all the current flows through the die and as a result, an increase in die thickness caused a reduction in current density through the die as shown by Fig. 3.17. This reduces the joule heat generation in the die. In the case of the conductive copper sample, the current distribution is slightly different. Here, current flows through both the sample and die. The change in the die thickness did not change the current density inside the sample significantly. Since copper is a better conductor, majority of the current had flown through it and the rest through the die. The change in current density inside the die was more evident than that of inside the copper sample. For the 10 mm thick die, near the die-sample interface there was sudden increase in the current density inside the die. This surprising change could be because of significant current crowding near the interface for the thinner copper sample.

The temperature and current profile in punch-sample-punch assembly for the alumina and copper samples are shown respectively in Fig. 3.19 and 3.20. The punch temperature went down as the die got thicker due to increased heat loss from the punch to die. However, there was no noticeable change in the current density distribution in punch-sample-punch assembly with the change in die thickness.

In addition, it was also found that the overall system resistance decreased with an increase in die thickness (Table 3.2). This happened because the increased die thickness added some parallel resistances (alternate path to current flow) to the already existing sample-punch resistance and as a result, the overall system resistance decreased. Lower system resistance results in reduced joule heat generation and consequently lower temperature in the system. Hence, the reduction in temperature with increase in die thickness was due to two reasons- increased radiation heat loss from the die surface and reduced system resistance.

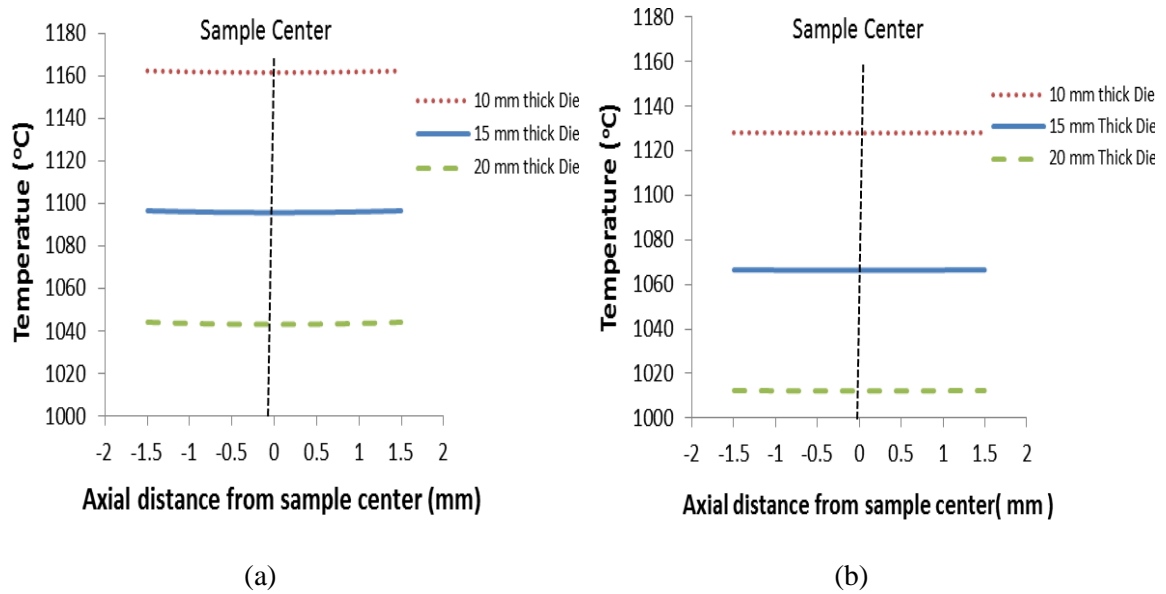


Fig. 3.14: Temperature distribution in axial direction in the sample as a function of die thickness: (a) alumina and (b) copper

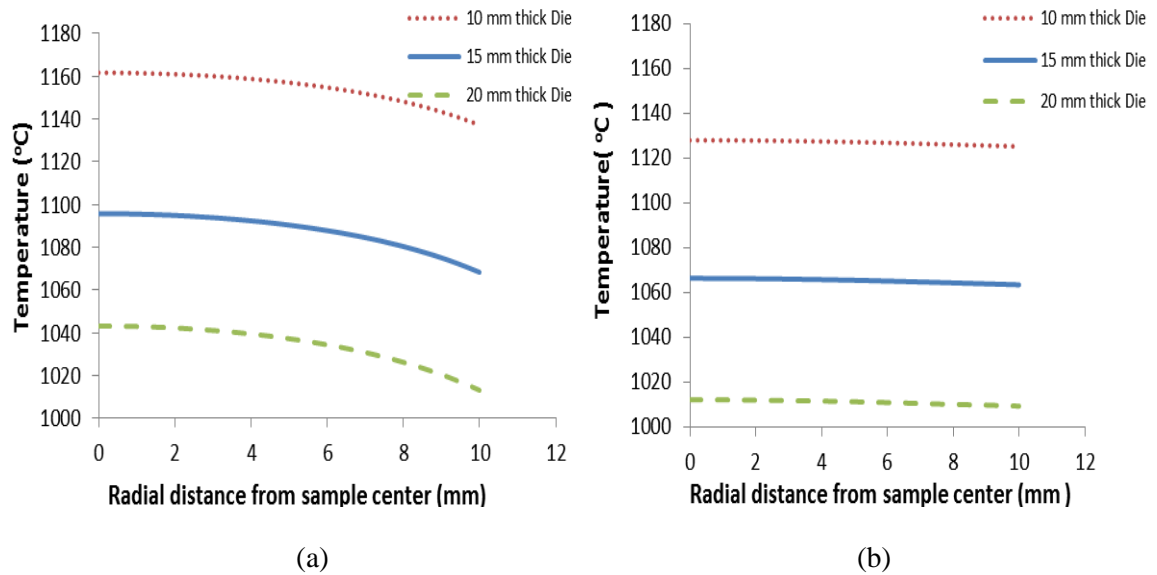
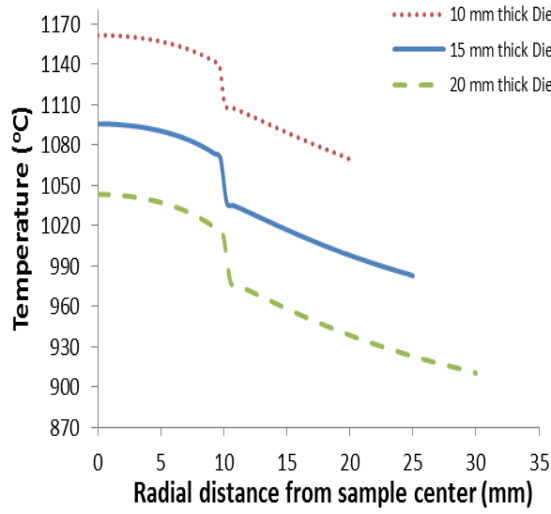
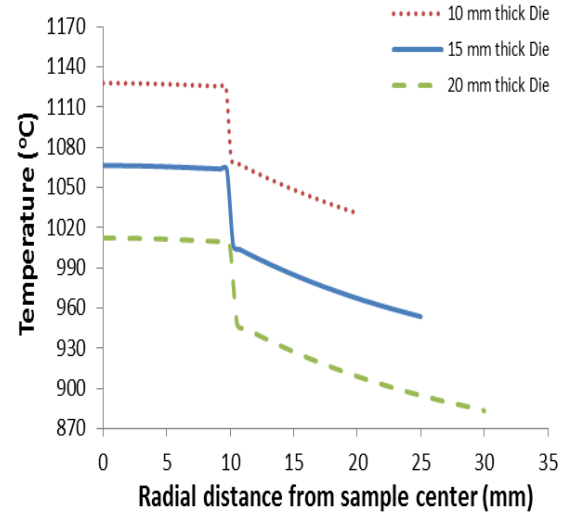


Fig. 3.15: Temperature distribution in radial direction in the sample as a function of die thickness: (a) alumina and (b) copper

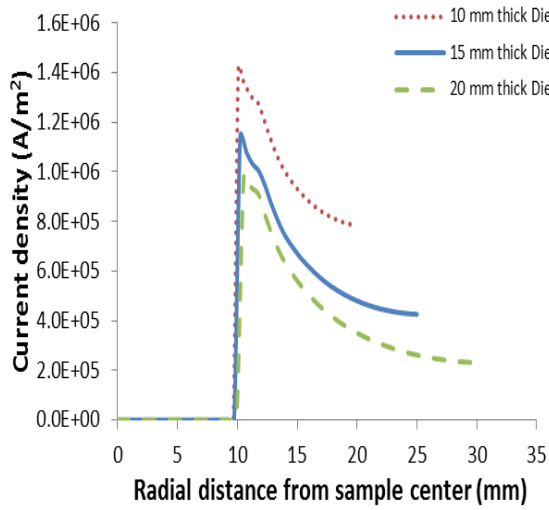


(a)

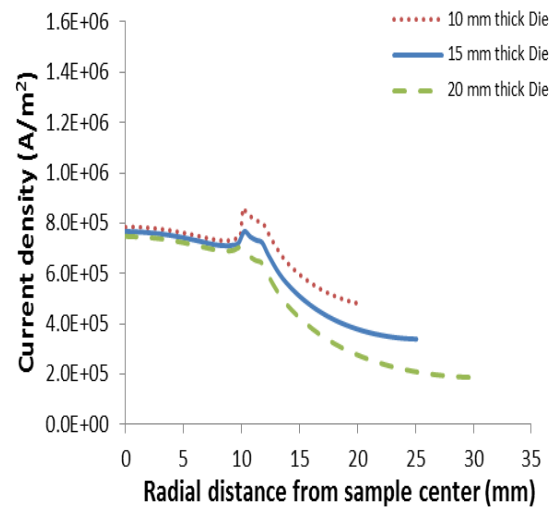


(b)

Figure 3.16: Temperature distribution in sample-die as a function of die thickness: (a) alumina and (b) copper



(a)



(b)

Figure 3.17: Electric current density distribution in sample-die as a function of die thickness: (a) alumina and (b) copper

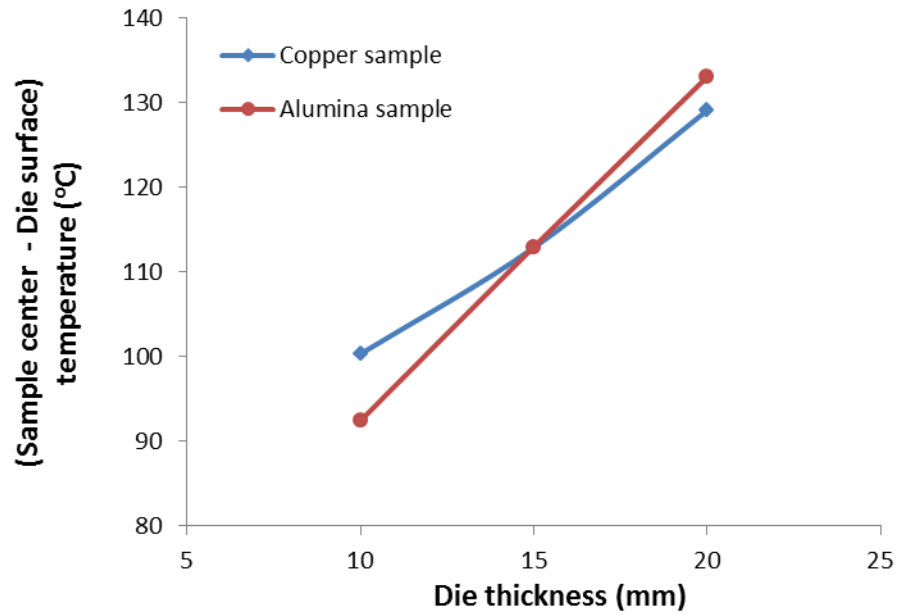


Figure 3.18: Temperature difference between sample center and die surface as a function of die thickness

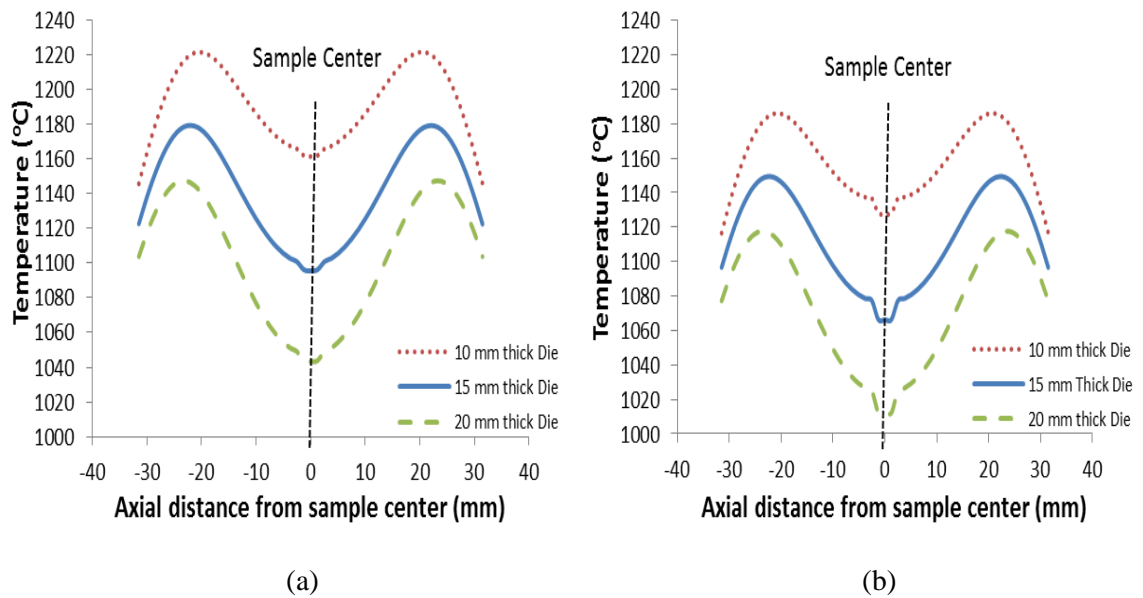


Figure 3.19: Temperature distribution in punch-sample-punch as a function of die thickness: (a) alumina and (b) copper

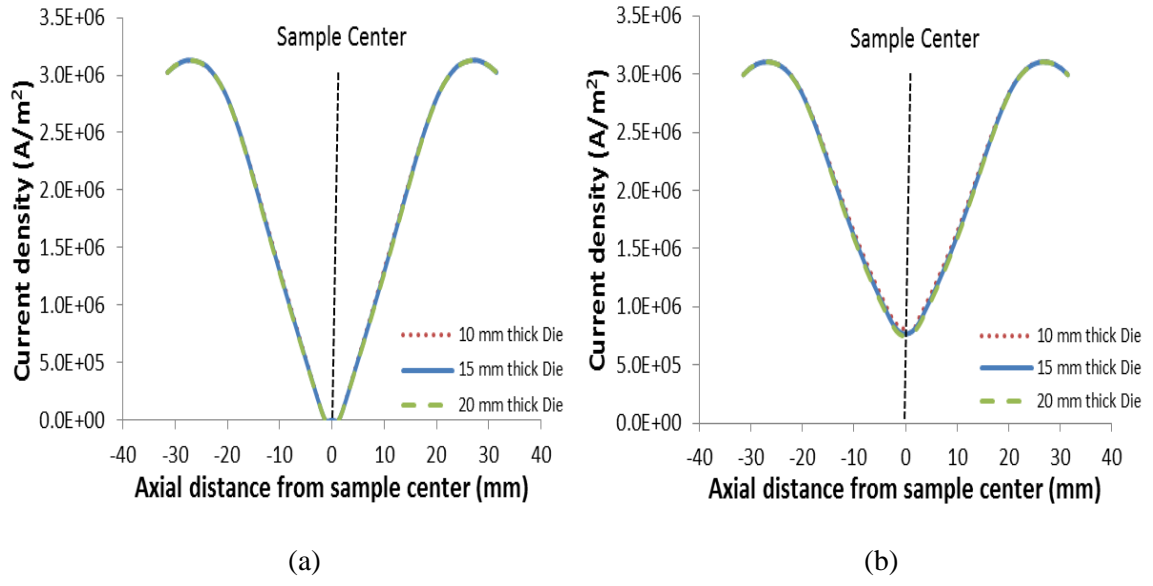


Figure 3.20: Electric current density distribution in punch-sample-punch as a function of die thickness: (a) alumina and (b) copper

Table 3.2: System resistance for different die thickness

Die thickness	System resistance (mΩ)	
	alumina sample	copper sample
10 mm	3.32	3.19
15 mm	3.28	3.16
20 mm	3.23	3.13

3.3.4 Effect of die height

The importance of the die height is not considered that much in common practice. However, height of the die could actually influence the temperature distribution in the system. To study the importance of die height on the temperature distribution in SPS system, three different die heights – 35 mm, 40 mm and 45 mm were studied.

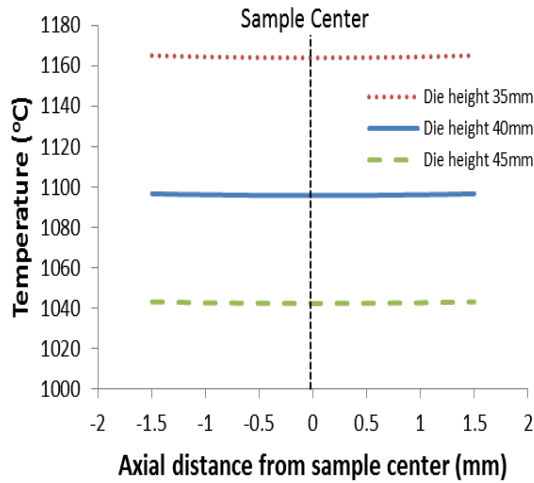
Fig. 3.21 and 3.22 show the temperature distributions in the sample in axial and radial directions respectively for both the alumina and copper samples. The temperature in the sample decreased with an increase in the die height. The maximum temperature in the alumina sample decreased from 1165° C to 1045° C and in the copper sample, it decreased from 1122° C to 1016° C as the die height was increased from 35 mm to 45 mm. There was also a reduction in the temperature gradient both in the axial and radial directions. This change in the temperature gradient inside the sample due to the change in die height is more significant than the change in temperature gradients due to the change in die thickness. The radial temperature gradient in the alumina sample decreased from 34° C to 22° C and in the copper sample from 4° C to 2° C for the aforementioned change in the die height. The temperature gradients in the axial direction also decreased slightly.

Fig. 3.23 and 3.24 show the temperature and current distributions respectively in sample-die as a function of die height. Although there was no change in sample or die diameter, a change in current density is observed with the change in die height. This change was more evident in the conducting sample. When the die height is small, the parallel path for current flow through the sample and the die is also small. For the conductive copper sample, more current tends to pass through the sample. This results in an increase in current density for the shorter die. At the same time, there is more current crowding near the interface of sample-die. As a result, the current density near the sample-die interface for the smaller die is also higher and this current density

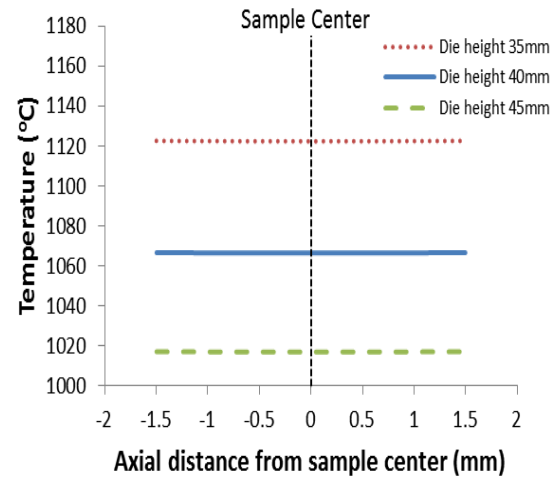
tends to get lower towards the outer surface. Similar incident takes place in the case of the non-conductive sample; however, the change in current distribution for the alumina sample is not significant since all the current passes through the die only (Fig. 3.23).

The difference in temperature between sample center and die surface with the change in die height is shown in Fig. 3.25 for both the alumina and copper samples. It is quite interesting to note that the difference between the two temperatures for both the samples was very much similar for different die heights. In both cases, with an increase of die height from 35mm to 45mm, the temperature difference between sample center and die surface decreased from about 140° C to 90° C. Temperature and current distribution in punch-sample-punch are shown in Fig. 3.26 and 3.27. Higher temperature is found in the punch for the die with smaller height. However, the current density in the punch-sample-punch was not affected substantially by the change of die heights.

Like the increase in the die thickness case, the increase in die height also reduced the overall system resistances (Table 3.3). As the die height is increased, the alternate path for current flow through the die comes into existence earlier, which means current flowing only through the portion of the punch is reduced and the remaining portion of the punch, which is paralleled with the die, is increased. This decreases the overall system resistance and thus the overall joule heat generation. In addition, there will be more heat loss by radiation due to increase in the die surface area, which also accounts for lower temperatures in the system.

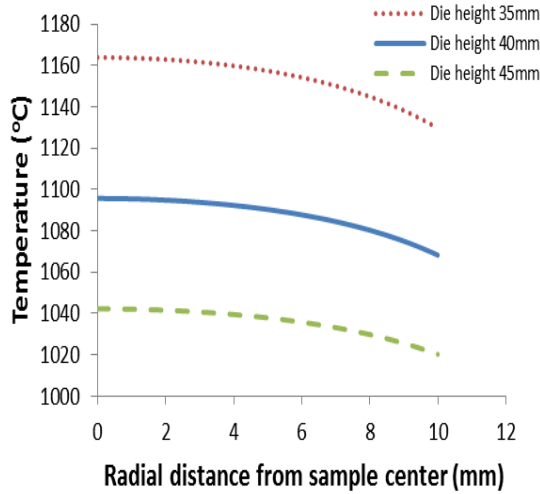


(a)

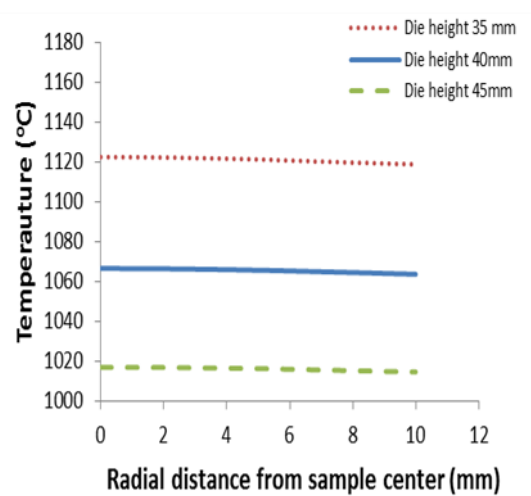


(b)

Fig. 3.21: Temperature distribution in axial direction in the sample as a function of die height: (a) alumina and (b) copper

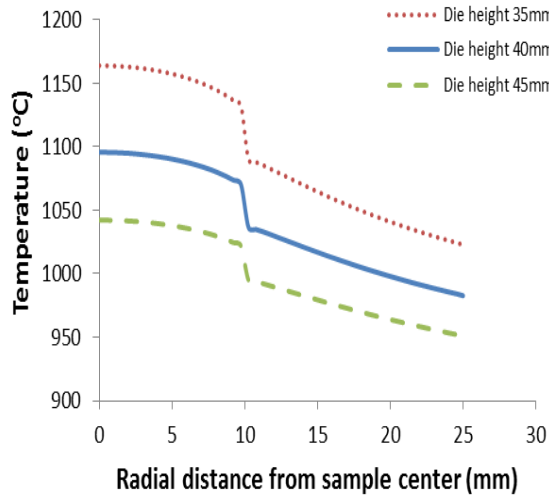


(a)

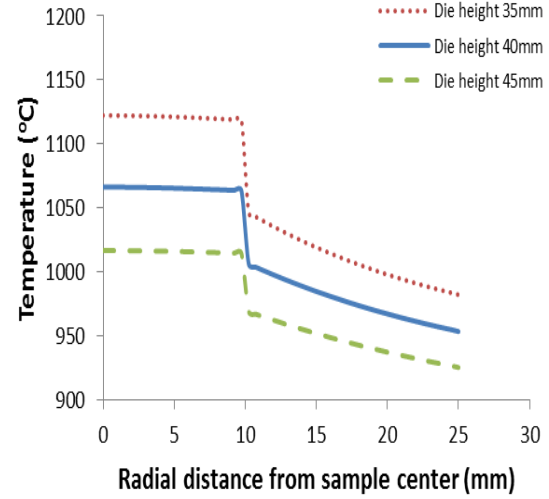


(b)

Fig. 3.22: Temperature distribution in radial direction in the sample as a function of die height: (a) alumina and (b) copper

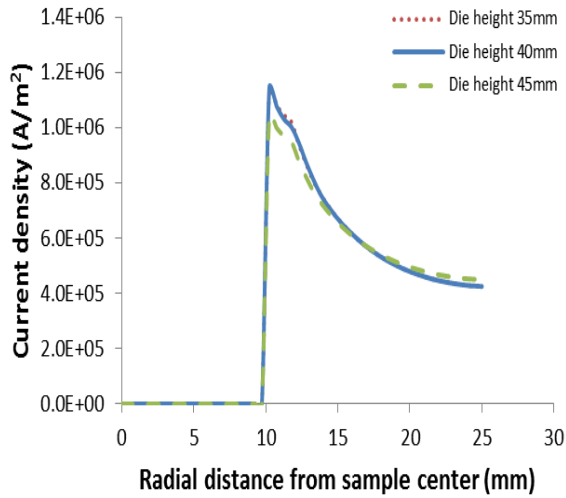


(a)

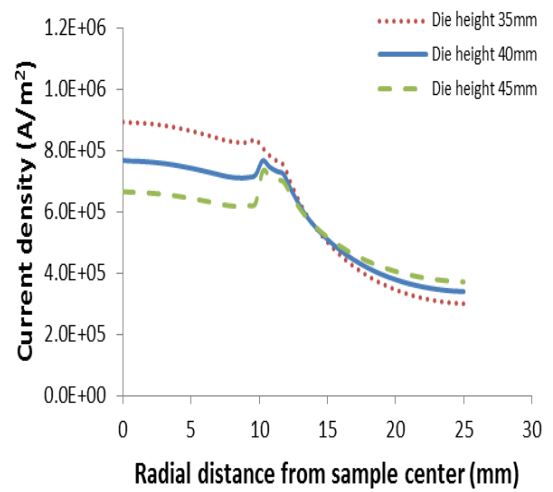


(b)

Fig. 3.23: Temperature distribution in sample-die as a function of die height: (a) alumina and (b) copper



(a)



(b)

Fig. 3.24: Electric current density distribution in sample-die as a function of die height: (a) alumina and (b) copper

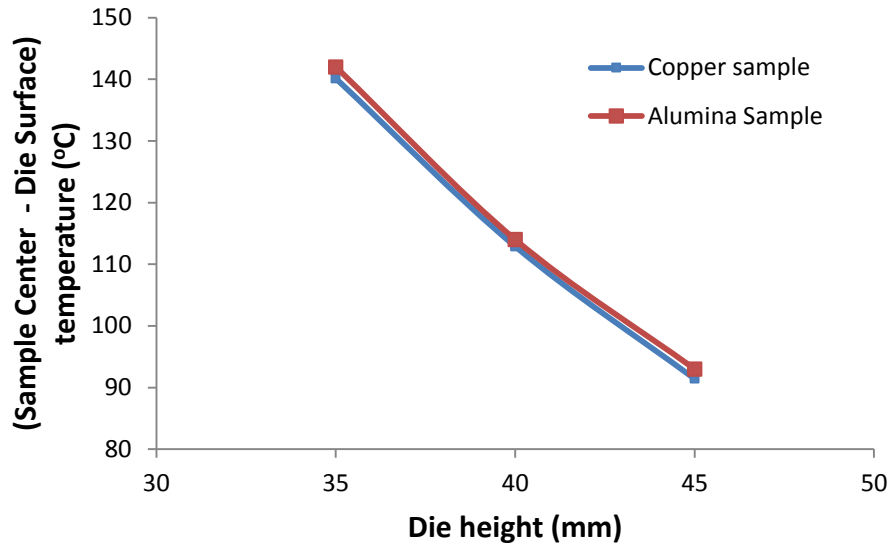


Fig. 3.25: Temperature difference between sample center and die outer surface as a function of die height

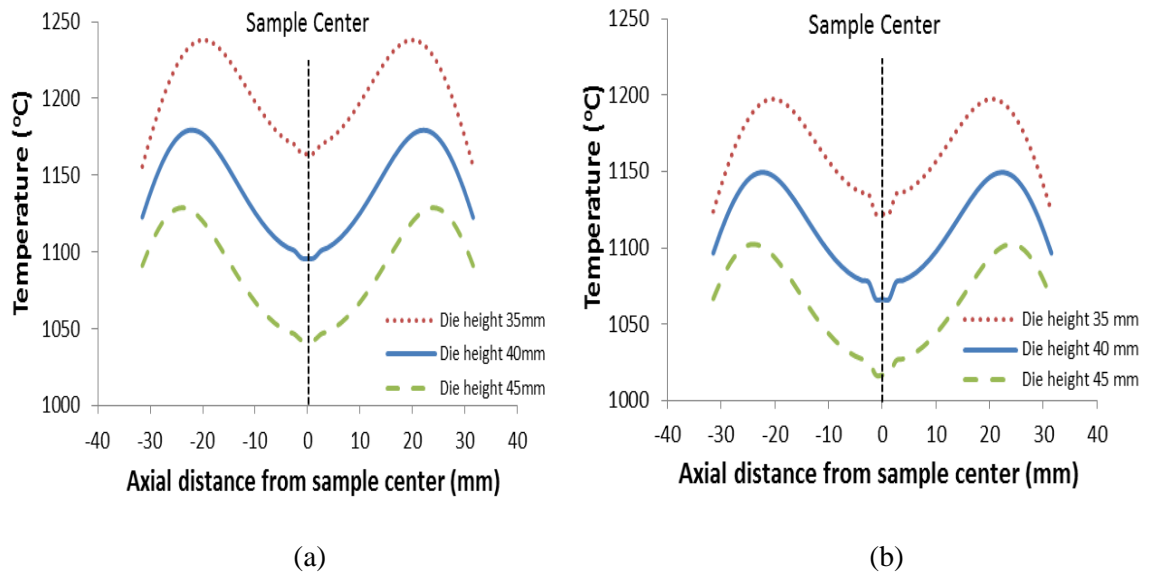


Fig. 3.26: Temperature distribution in punch-sample-punch as a function of die height: (a) alumina and (b) copper

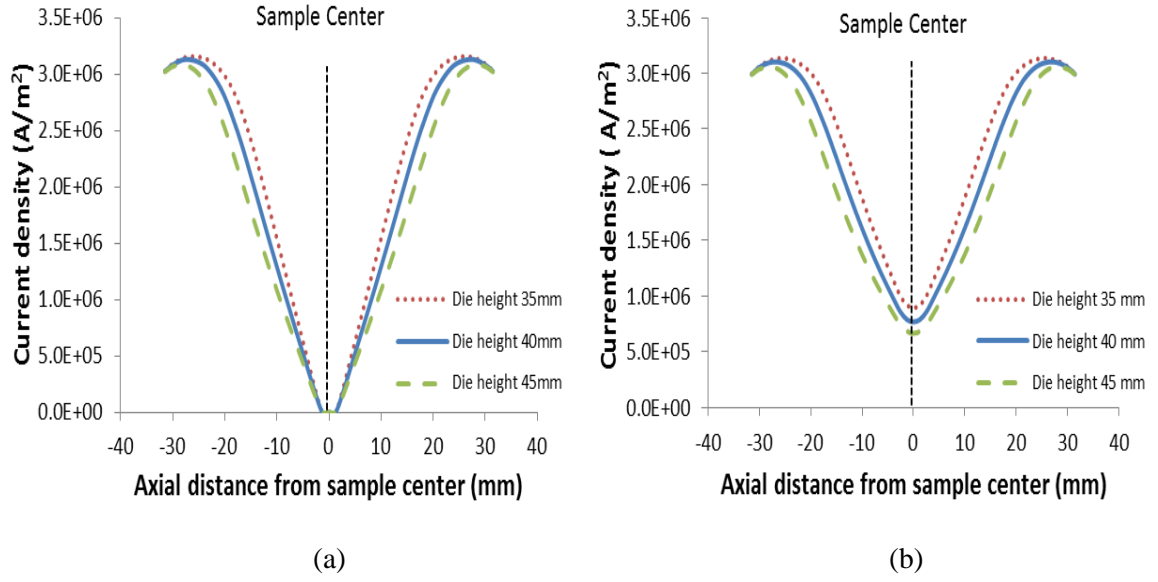


Fig. 3.27: Electric current density distribution in punch-sample-punch as a function of die height:
(a) alumina and (b) copper

Table 3.3: System resistance for different die heights

Die height	System resistance (mΩ)	
	alumina sample	copper sample
35 mm	3.44	3.27
40 mm	3.28	3.16
45 mm	3.17	3.06

3.3.5 Effect of punch length

Punch length is another important factor that could affect the temperature distribution in SPS system. The effect of punch length on temperature distribution in SPS system was studied for three different punch lengths- 25mm, 30mm and 35 mm for both the alumina and copper samples. Punch in the SPS system has the smallest diameter and consequently the highest resistance. Since joule heating is the only mechanism for heat generation, punch is the main source of heating. With the increase in punch length, there is an increase in overall system resistance; the difference coming from the difference in lengths of the punches. This is shown in Table 3.4. This leads to higher temperature in the overall system. An increase in punch length also increases exposed portion of the punch, which can radiate heat to the chamber. However, the heat generation in the punch due to joule heating is much more than heat loss by radiation from the exposed punch area.

Fig. 3.28 and 3.29 show the temperature distribution inside the sample in the axial and radial directions respectively for both the samples. With an increase of punch length from 25mm to 35mm, the maximum temperature in the sample increased from 1060° C to 1128° C for the alumina and 1028° C to 1094° C for the copper sample. The change in punch length, however, did not have great impact on the temperature gradient inside the sample. The axial temperature gradient was not affected by the change in punch length. Even in the radial direction, the temperature difference between sample center and edge changed slightly from 24° C to 30° C for the alumina sample when the punch length was increased from 25 mm to 35 mm. However, the radial temperature gradient in the copper sample increased by only 0.5° C for the same change in punch length.

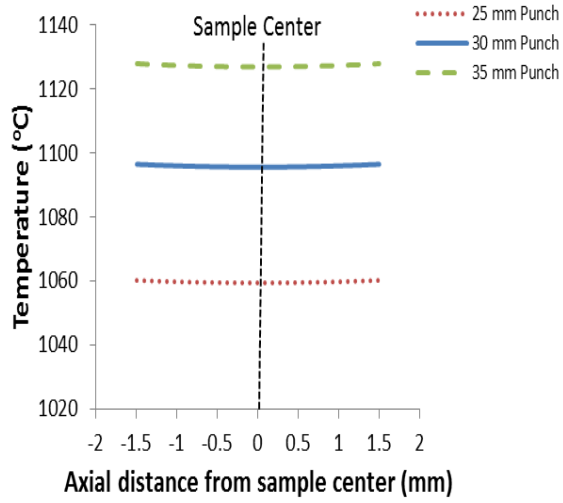
Fig. 3.30 and 3.31 show the temperature and current distributions in the sample-die assembly for different punch lengths. With an increase of punch length, the die surface

temperature increased like all other parts of SPS; however, the temperature difference between sample center and die surface did not change by a great amount (Fig. 3.30). This temperature difference between sample center and die outer surface increased by 11° C for alumina and 7° C for copper sample when the punch length was changed from 25 mm to 35 mm. However, there was no change in current distribution in the sample-die with the change in punch length (Fig. 3.31).

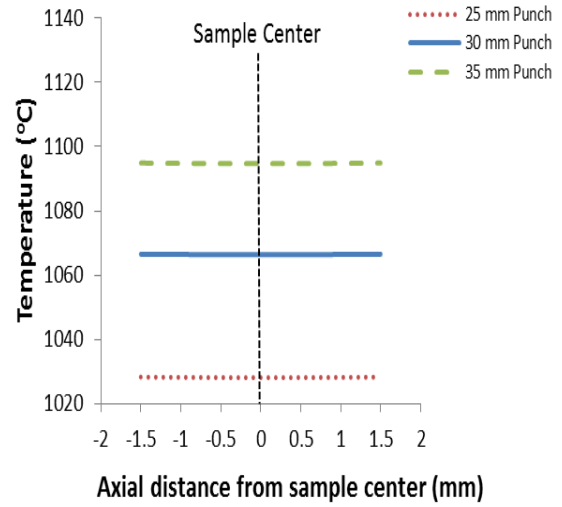
The temperature and current distributions in the punch-sample-punch assembly for different punch lengths are shown in Fig. 3.32 and 3.33 respectively. The maximum temperatures in the system were generated in the punches, which were 1110.43° C, 1179.25° C and 1239.99° for the alumina sample and 1080.55° C, 1149.37° C and 1209.29° C for the copper sample for punches of lengths 25 mm, 30 mm and 35 mm respectively (Fig. 30). An increase in punch length from 25 mm to 35 mm resulted in an increase in maximum punch temperature by about 130° C for both the samples. It is obvious that increase in punch length can cause excessive high temperature in punch. For high temperature sintering (>2000°C), the maximum punch temperature could rise up to 2500° C which is the temperature at which graphite begins to creep.

Table 3.4: System resistance for different punch lengths

Punch length	System resistance (mΩ)	
	alumina sample	copper sample
25 mm	3.05	3.01
30 mm	3.28	3.16
35 mm	3.55	3.36



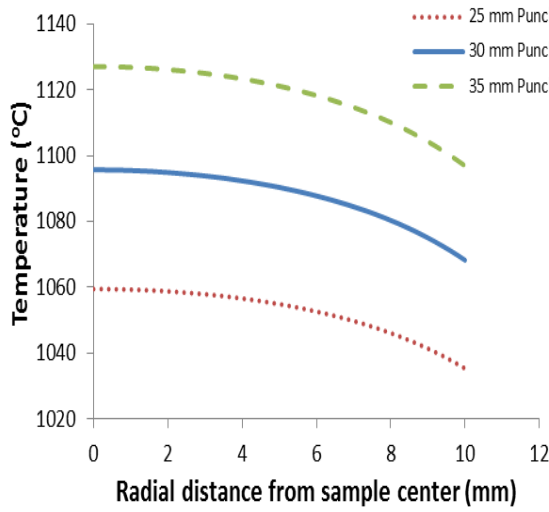
(a)



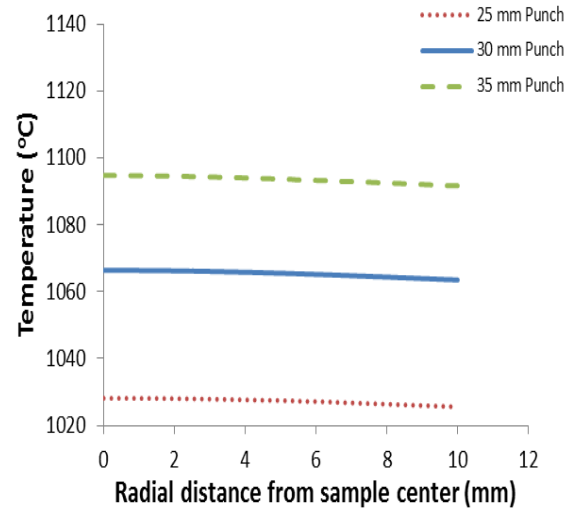
(b)

Fig. 3.28: Temperature distribution in axial direction in the sample as a function of punch length:

(a) alumina and (b) copper



(a)



(b)

Fig. 3.29: Temperature distribution in radial direction in the sample as a function of punch length: (a) alumina and (b) copper

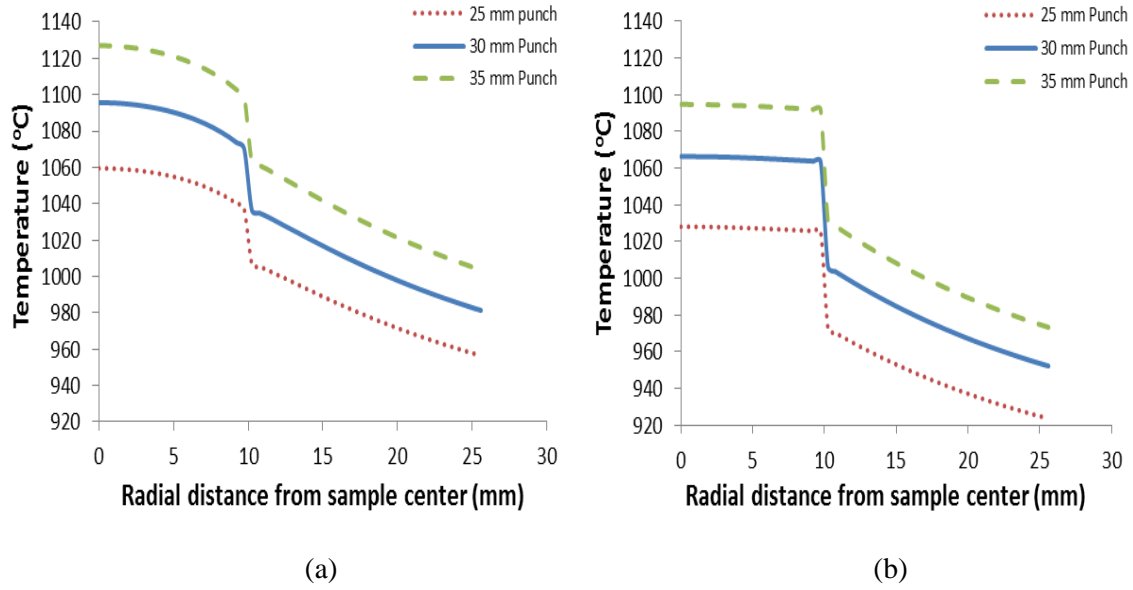


Fig. 3.30: Temperature distribution in sample-die as a function of punch length: (a) alumina and (b) copper

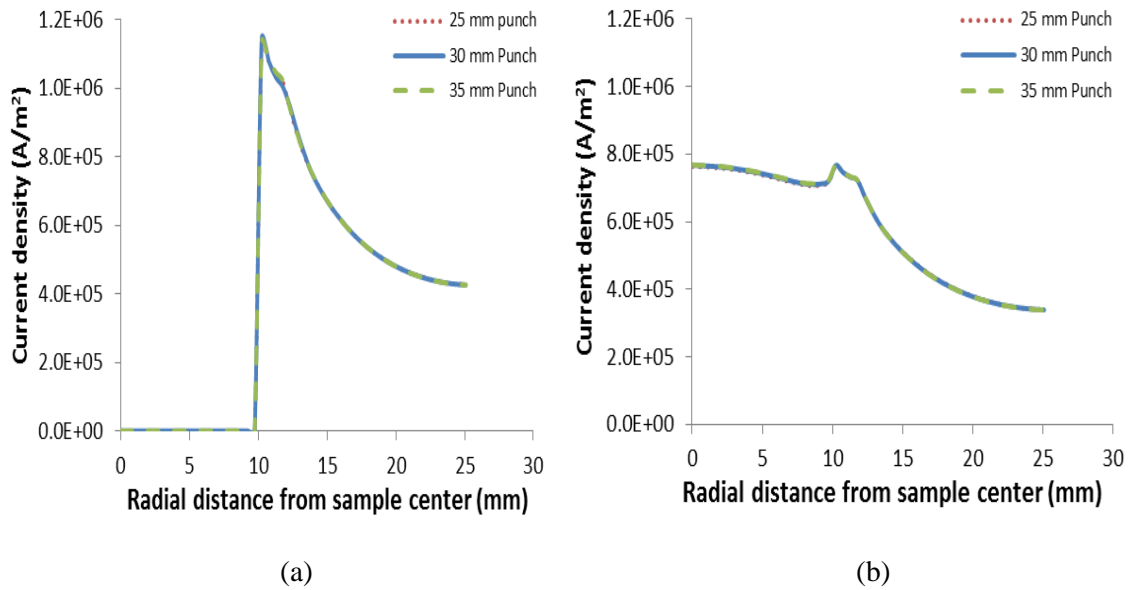
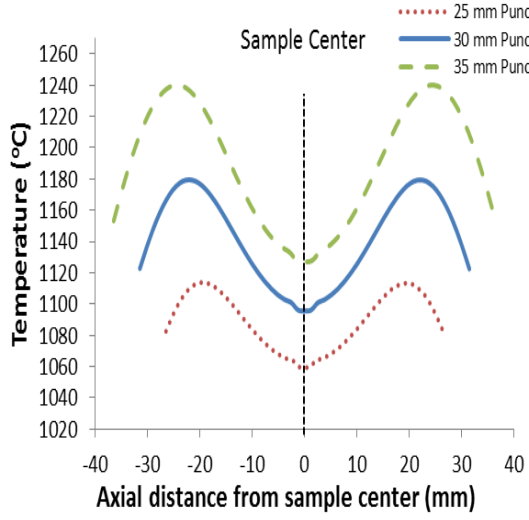
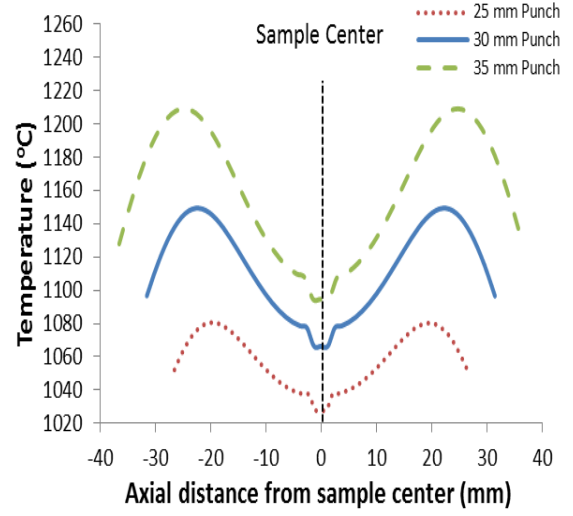


Fig. 3.31: Electric current density distribution in sample-die as a function of punch length: (a) alumina and (b) copper

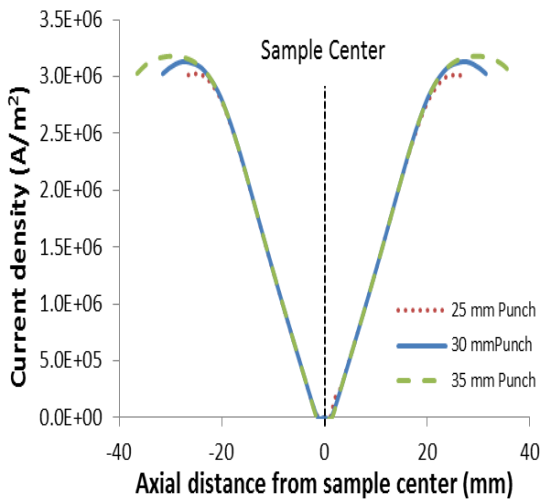


(a)

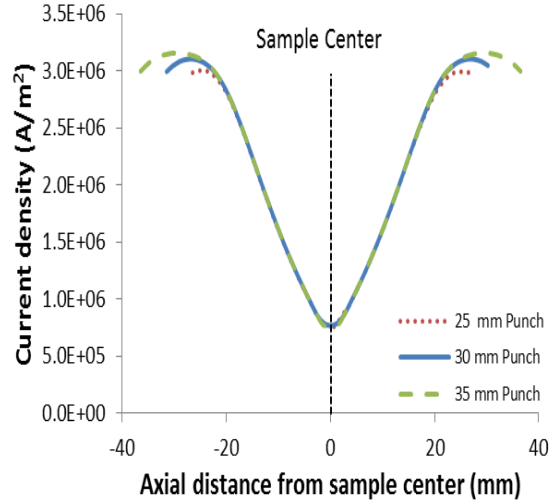


(b)

Fig. 3.32: Temperature distribution in punch-sample-punch as a function of punch length: (a) alumina and (b) copper



(a)



(b)

Fig. 3.33: Electric current density distribution in punch-sample-punch as a function of punch length: (a) alumina and (b) copper

3.3.6 Effect of asymmetric punch-die position

One common incident that happens while lining up sample, punch and die in a SPS setup is asymmetric positioning of the punches in the die. This could happen because of lack of attention or because of differences in sliding friction between the interfaces at the initial stage of sintering. The significance of this incident is always overlooked, but in our simulation, it was found that such situation could result in axial temperature gradient in the sample in addition to the existing radial gradient. A case study was done where the die shifted slightly upward causing asymmetric punch-die assembly. Three cases were considered - (a) die positioned symmetrically (b) die moved 2 mm upward and (c) die moved 4 mm upward.

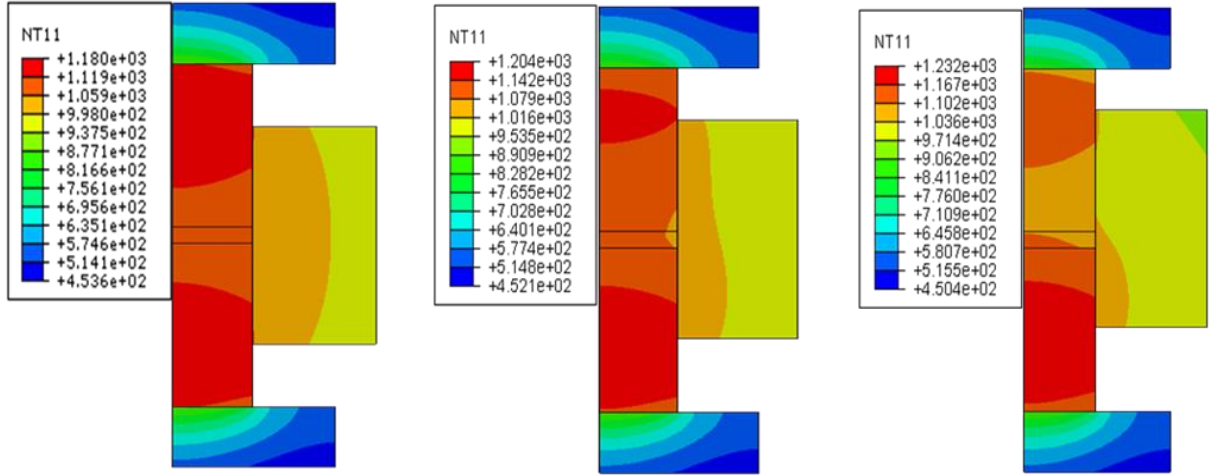
Fig. 3.34 and 3.35 show the temperature contours inside the SPS setup and sample respectively for the alumina and copper samples for the three cases studied here. It is evident that the temperature distribution is much more non-uniform in Fig. 3.34 (c) than in Fig. 3.34 (a). The maximum temperature in the alumina sample in Fig. 3.35 (c) is 1117° C, which is 20° C higher than that in Fig. 3.35 (a). This 1117° C temperature was found in the bottom surface of the sample at the center axis of symmetry. Similar kind of temperature distribution with lower magnitude was found in copper sample (Fig. 3.35 (a)-(c)).

The axial temperature distributions along the axis of symmetry in the sample for the three different cases studied here are shown in Fig. 3.36. There was hardly any temperature gradient in case (a) for both alumina and copper, but a temperature difference of about 17° C existed between sample top and bottom surface in case (c) for the alumina sample. However, the temperature difference between the sample top and bottom surface for the copper sample in case (c) was only 0.7° C. Fig. 3.37 shows the temperature distribution in radial direction in the alumina and copper samples for different positions of the die. Temperature inside the sample increased as the die was shifted from the center position; however, the radial temperature gradient was not affected by this

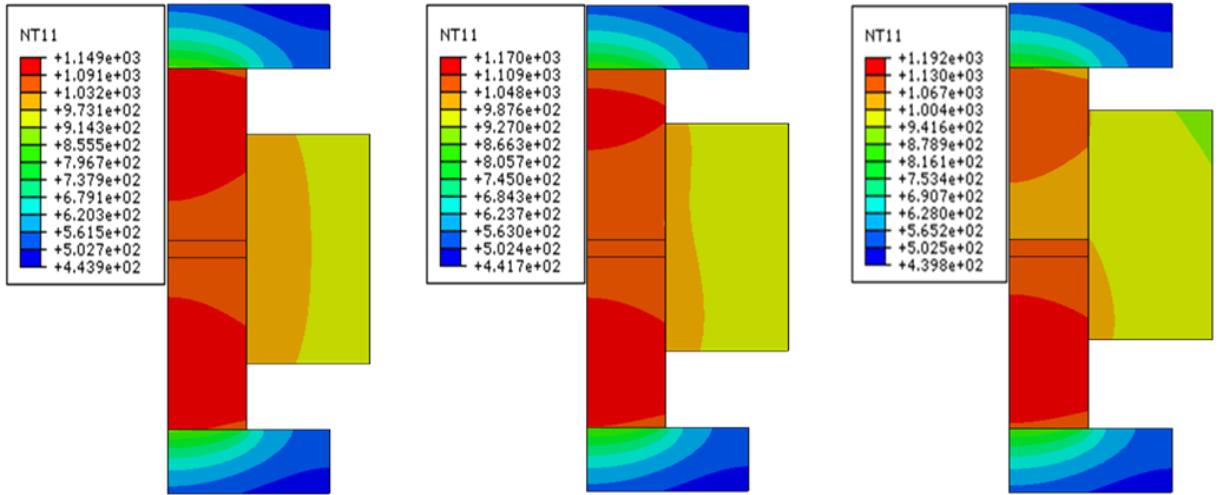
change in die position. Fig. 3.38 shows a linear relationship between axial shift of die and temperature difference between the top and bottom surface of the alumina sample. This axial temperature gradient can cause variation in material properties, which could be very significant for large and thick samples.

The difference in temperature between the sample center and the die outer surface did not increase that rapidly for moving the die upward (Fig. 3.39). It increased slightly from 114° C for case (a) to 122° C for case (c) for the alumina sample. Fig. 3.40 shows the electric current distribution in sample-die for all the three cases. The temperature distribution in punch-sample-punch assembly is shown in Fig. 3.41. When the die was moved upward, the temperature in the lower punch became greater than the temperature in the upper punch. A very asymmetric temperature distribution was found between the two punches for both the samples. The difference between the maximum temperatures in the upper and lower punches when the die was moved upward by 4 mm was about 100° C for the alumina sample and 90° C for the copper sample. The current distribution in the punch-sample-punch assembly is shown in Fig. 3.42 which was also asymmetric for case (b) and (c).

All these changes in temperature distribution are due to fact that, as the die was moved upward, the upper punch was covered more by the die, which could take more heat away from it. On the other hand, the lower punch was less covered by the die and as a result got hotter. In addition, the resistance in the upper punch was also reduced as the exposed portion of the upper punch became less, which is the main source of joule heat generation. The opposite incident happened in the lower punch.

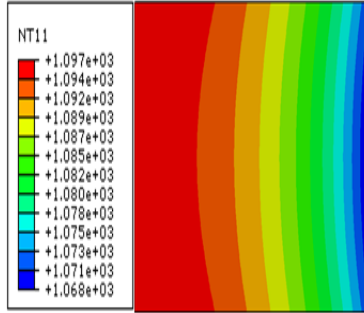


(a) Symmetric die position (b) Die moved 2 mm upward (c) Die moved 4 mm upward

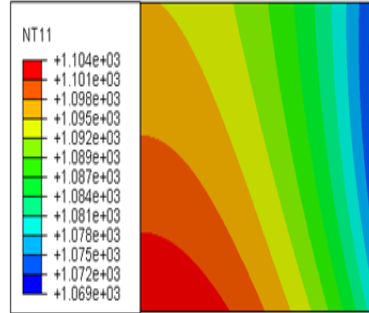


(d) Symmetric die position (e) Die moved 2 mm upward (f) Die moved 4 mm upward

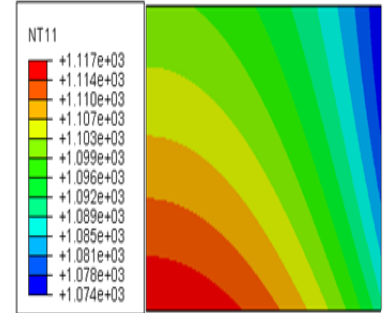
Fig. 3.34: Temperature contour plots in the SPS systems for different die positions: (a-c) alumina, and (d-f) copper



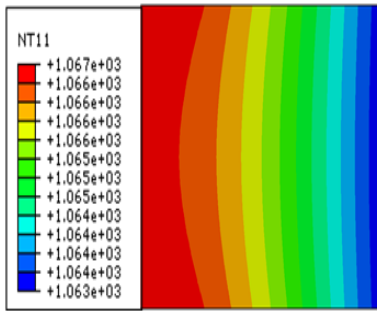
(a) Symmetric die position



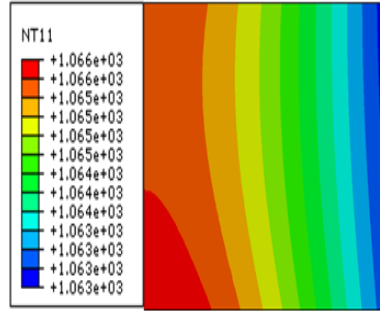
(b) Die moved 2 mm upward



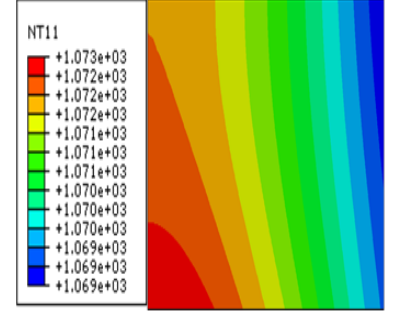
(c) Die moved 4 mm upward



(d) Symmetric die position

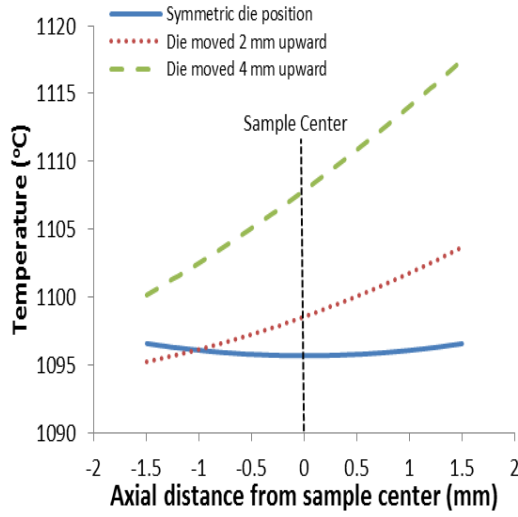


(e) Die moved 2 mm upward

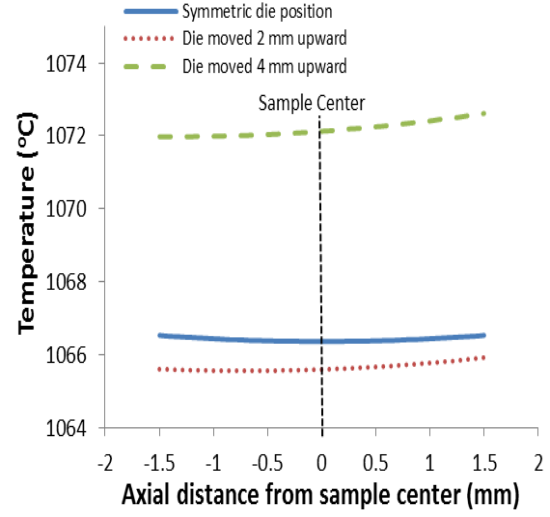


(f) Die moved 4 mm upward

Fig. 3.35: Temperature contour plots of the samples for different die positions: (a-c) alumina, and (d-f) copper

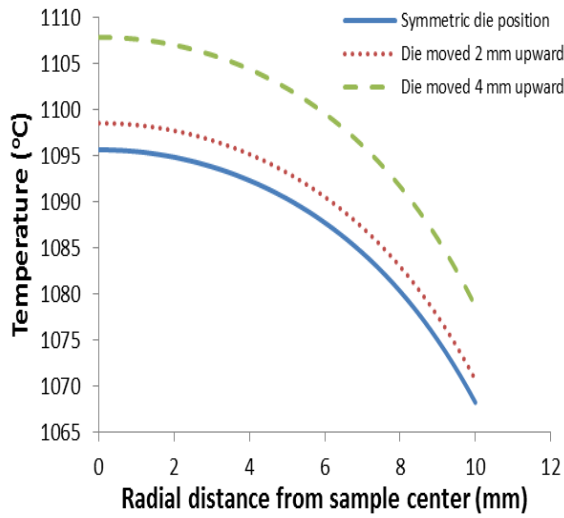


(a)

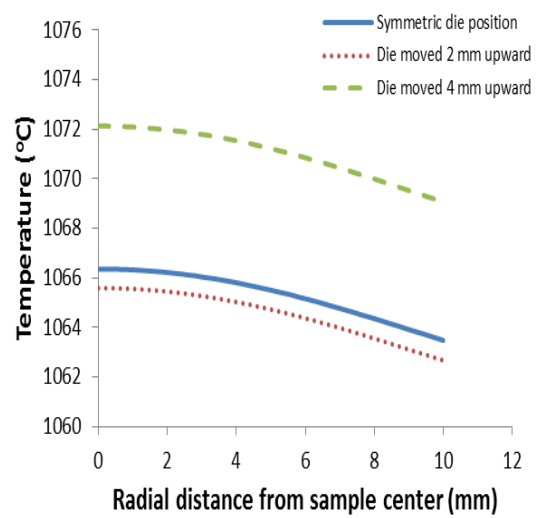


(b)

Fig. 3.36: Temperature distribution in axial direction in the sample for different die positions: (a) alumina and (b) copper



(a)



(b)

Fig. 3.37: Temperature distribution in radial direction in the sample for different die positions: (a) alumina and (b) copper

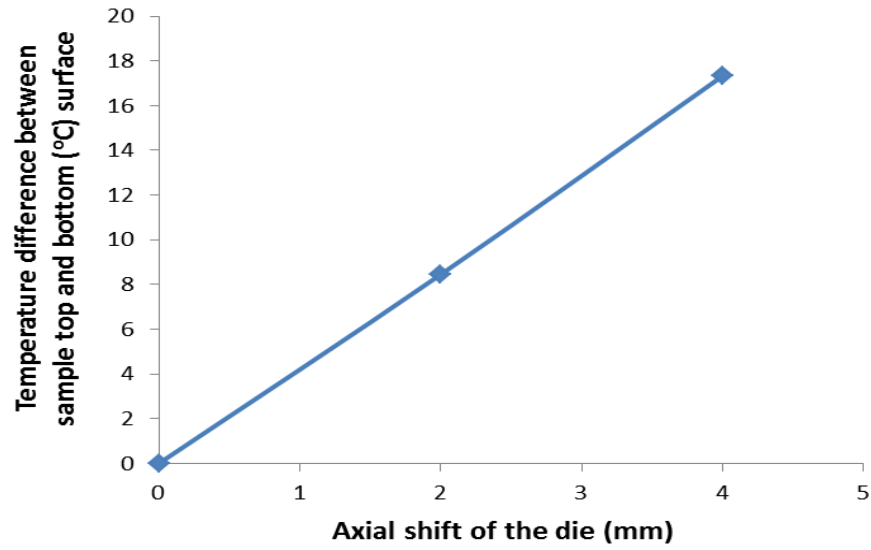


Fig. 3.38: Temperature difference between the sample top and bottom surfaces as a function of axial shift of die

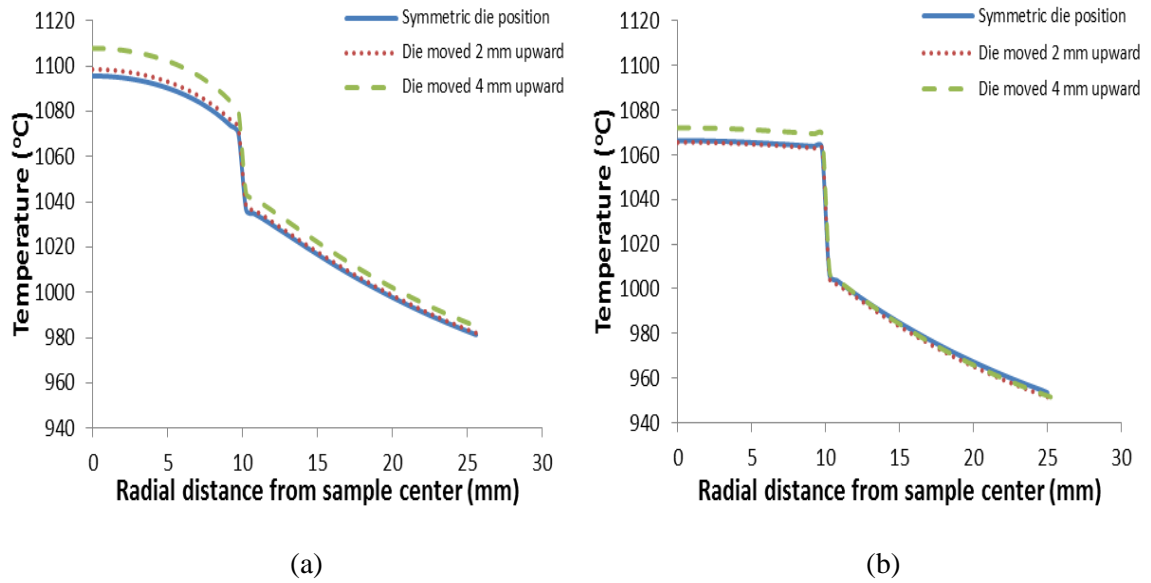


Fig. 3.39: Temperature distribution in sample-die for different die positions: (a) alumina and (b) copper sample

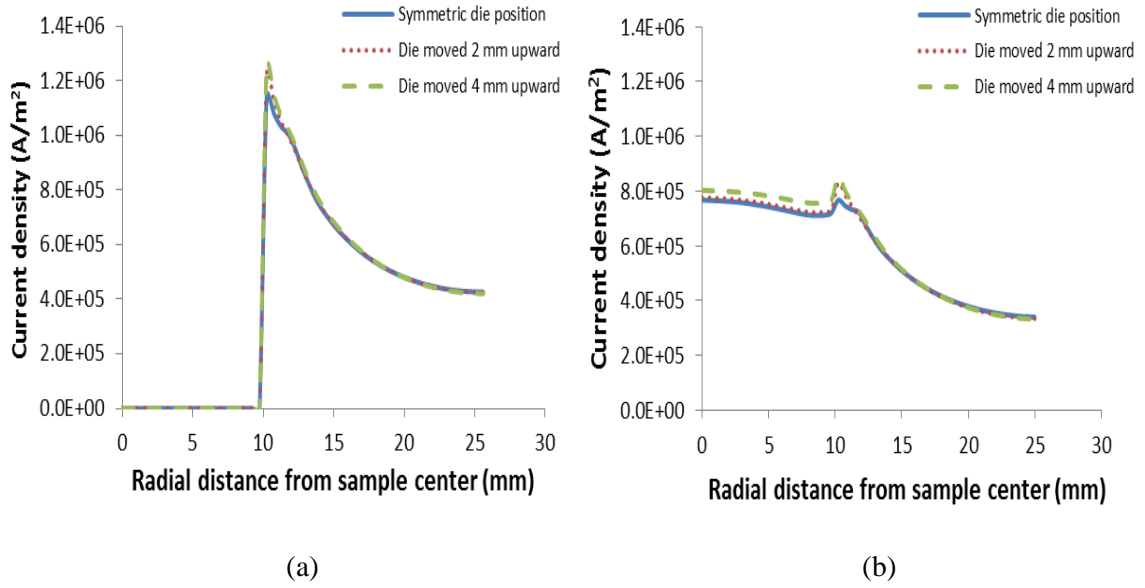


Fig. 3.40: Electric current density distribution in sample-die for different die positions: (a) alumina and (b) copper sample

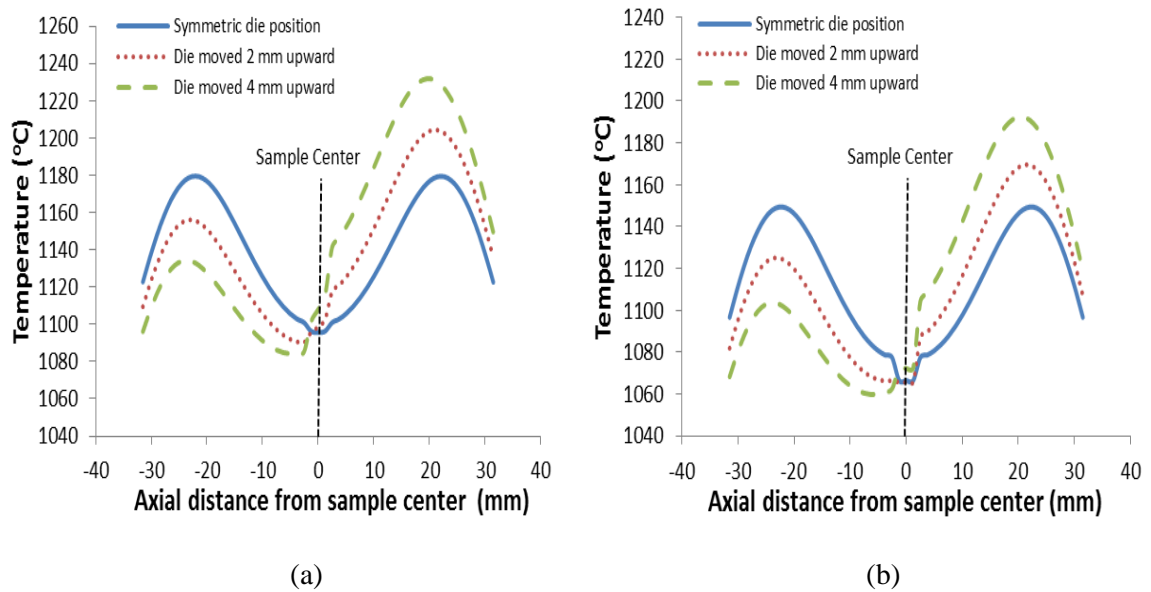


Fig. 3.41: Temperature distribution in punch-sample-punch for different die positions: (a) alumina and (b) copper

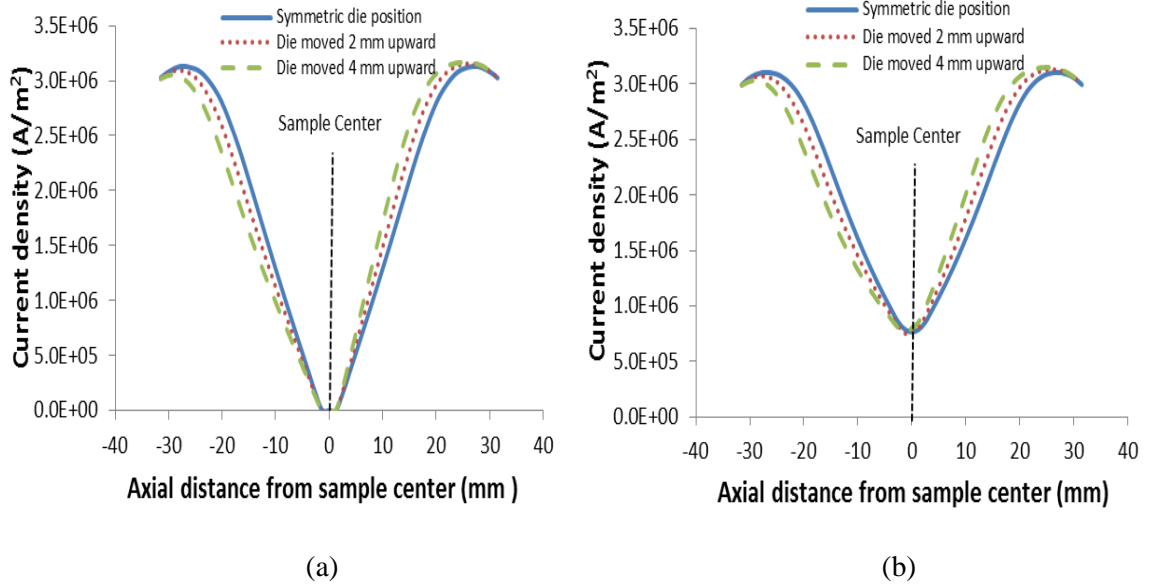


Fig. 3.42: Electric current density distribution in punch-sample-punch for different die positions:
(a) alumina and (b) copper sample

3.3.7 Effect of using unequal punch length

Another incident that is quite often overlooked in SPS is the use of unequal length of punch. This incident can also cause temperature gradients inside the sample. To find out the significance of using equal length of punches, three cases were considered – (a) both the punches are 30 mm long, (b) the upper punch is 30 mm while the lower one is 27mm and (c) the upper punch is 30mm and the lower one is 24mm.

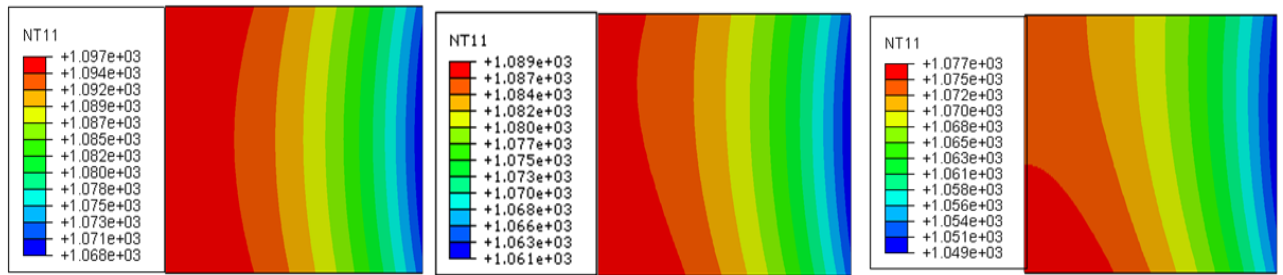
It was seen that the temperature profile in the sample and other parts have changed as the punches of different lengths were used together. The overall temperature distribution in the system became asymmetric. Fig. 3.43 shows the temperature contour inside the sample for different lengths of upper punch for both the alumina and copper samples. The temperature in the upper portion of the sample was lower than the lower portion. Non-uniformity in temperature distribution increased as the upper punch length was decreased. Fig. 3.44 and 3.45 show the axial

and radial temperature distributions inside the alumina and copper samples respectively. As the upper punch length was reduced, the maximum temperature in the system as well as inside the sample decreased. Maximum temperature in the alumina sample decreased by 20° C and in the copper sample by 13° C when the upper punch length was reduced from 30 mm to 24 mm. The axial and radial temperature gradients were also affected, particularly in the axial direction for the alumina sample. A temperature difference of about 4° C existed between the top and bottom surface in the alumina sample when the upper punch length was reduced to 24 mm. However, the temperature gradient in radial direction decreased slightly for both the alumina and copper samples, respectively by 2° C and 0.1° C.

Fig. 3.46 shows the temperature distribution in sample-die for alumina and copper sample. As expected, the die surface temperature decreased with the decrease in upper punch length. As the upper punch length was reduced from 30 mm to 24 mm, die surface temperature decreased in alumina by 21° C and in copper by 13° C. However, the temperature difference between sample center and die surface was hardly affected. This temperature difference between sample center and die surface decreased by 7° C for the alumina and by 2° C for the copper sample as the upper punch length was reduced from 30 mm to 24 mm. There was no change in the current distribution in the sample-die assembly as evident in Fig. 3.47.

There was considerable change in the punch temperature as the upper punch length was reduced (Fig. 3.48). The lower punch temperature remained very much the same; while the upper punch temperature went down rapidly. The difference between the maximum temperature in upper and lower punch was nearly 70° C and 60° C for alumina and copper sample respectively when the upper punch length was reduced to 24mm. Fig. 3.49 shows the current distribution in the punch-sample-punch assembly for the three cases considered here.

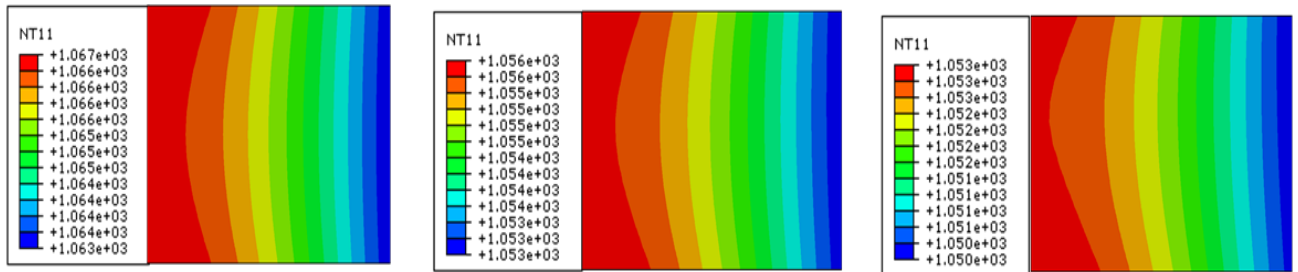
The differences in temperature with the change in upper punch length were caused by the fact that the total resistance in the upper part was reduced with the decrease in upper punch length and as a result, there was less joule heating in upper part. Moreover, as the die size and position were not changed, it enclosed major portion of the upper punch and took the heat away from it through conduction, which caused the temperature of the upper part to go down. There was no such change in lower punch and its temperature remained very much the same.



(a) 30 mm upper punch

(b) 27 mm upper punch

(c) 24 mm upper punch

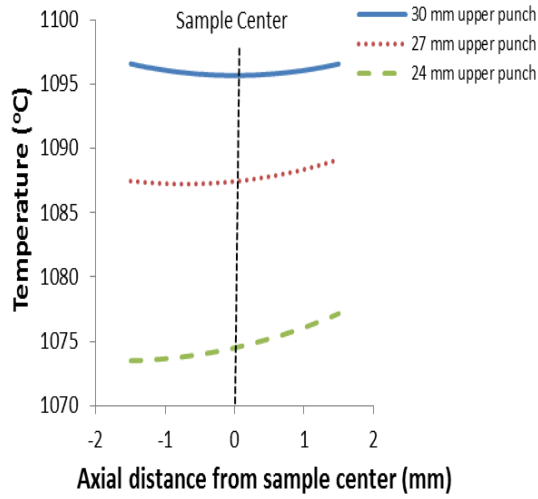


(d) 30 mm upper punch

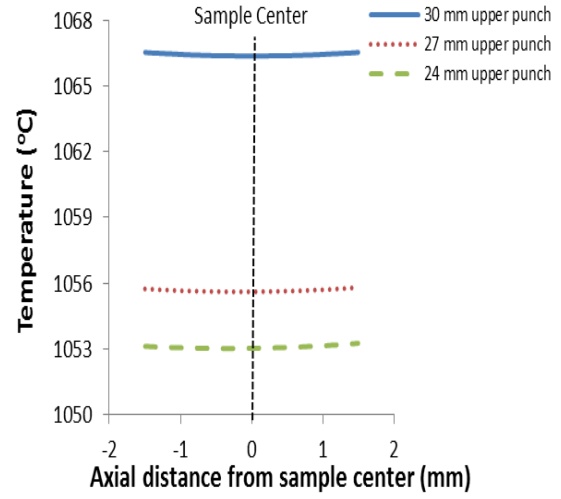
(e) 27 mm upper punch

(f) 24 mm upper punch

Fig. 3.43: Temperature contour plot in the sample for different lengths of upper punch: (a-c) alumina, and (d-f) copper

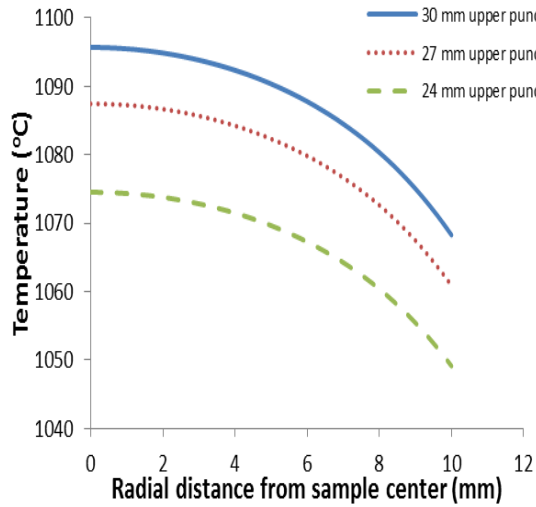


(a)

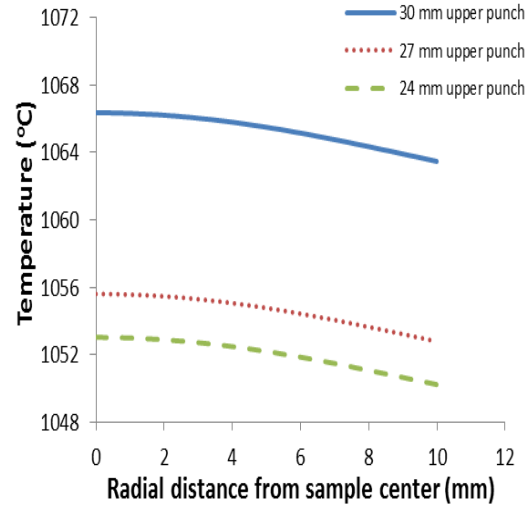


(b)

Fig. 3.44: Temperature distribution in axial direction in the sample for different lengths of upper punch: (a) alumina and (b) copper

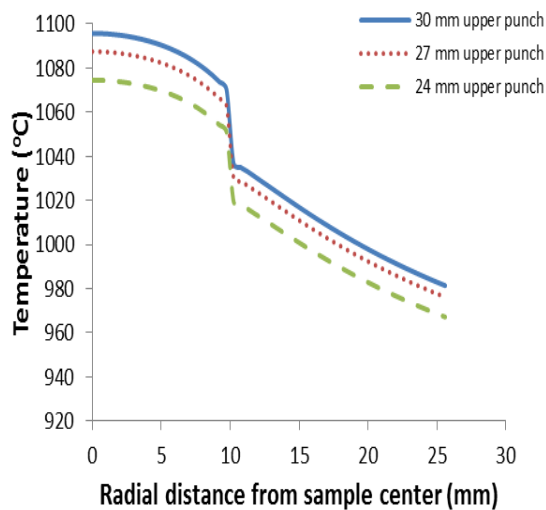


(a)

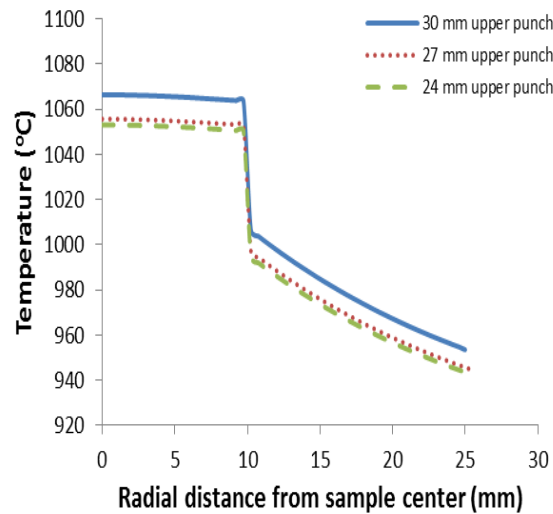


(b)

Fig. 3.45: Temperature distribution in radial direction in the sample for different lengths of upper punch: (a) alumina and (b) copper

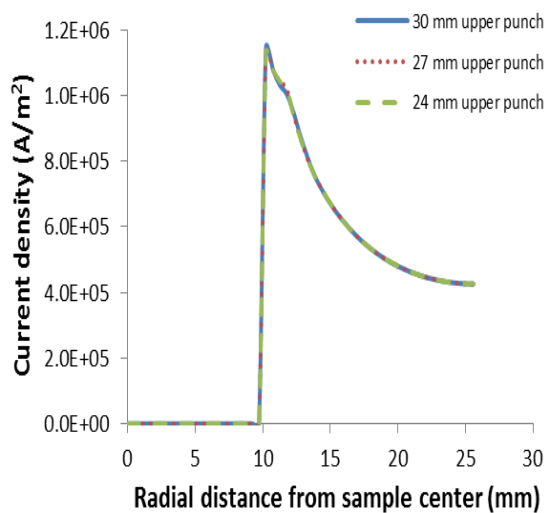


(a)

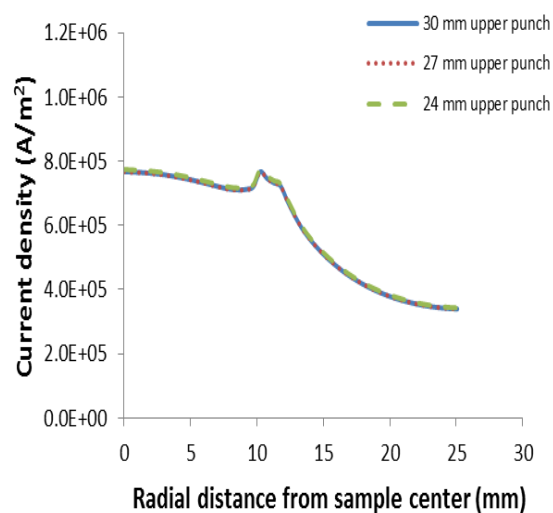


(b)

Fig. 3.46: Temperature distribution in sample-die for different length of upper punch: (a) alumina and (b) copper



(a)



(b)

Fig. 3.47: Electric current density distribution in sample-die for different length of upper punch: (a) alumina and (b) copper

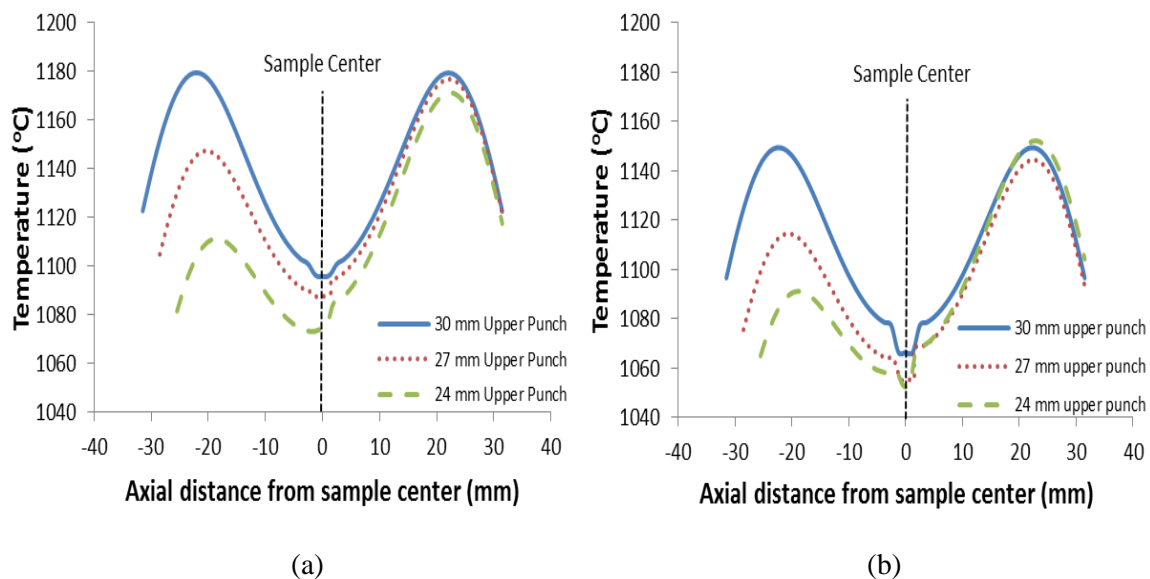


Fig. 3.48: Temperature distribution in punch-sample-punch for different lengths of upper punch: (a) alumina and (b) copper

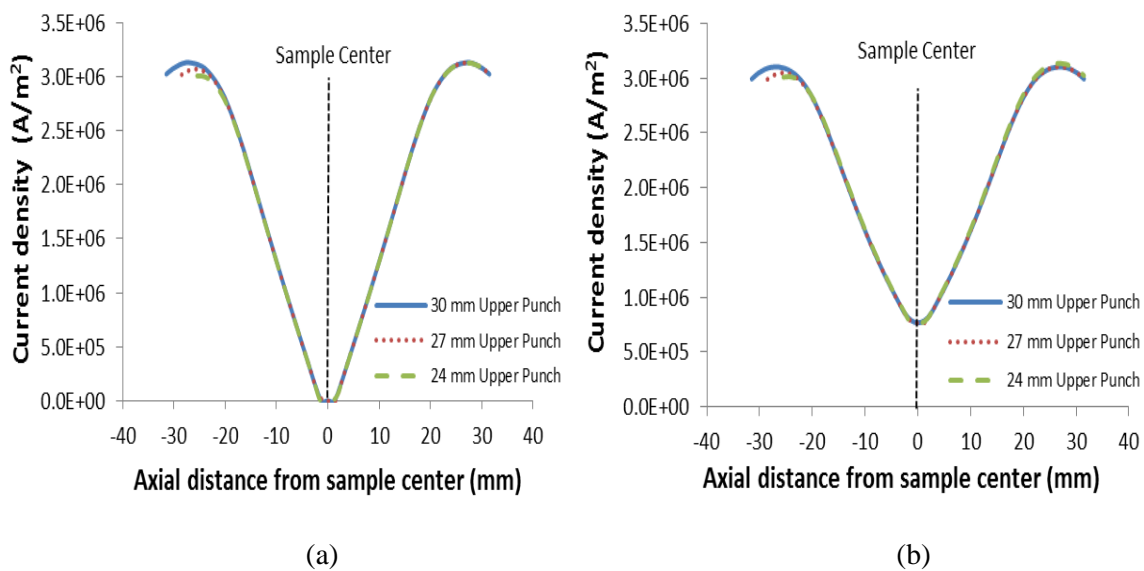


Fig. 3.49: Electric current density distribution in punch-sample-punch for different lengths of upper punch: (a) alumina and (b) copper

3.3.8 Effect of input current

In the actual sintering experiment, a temperature is set for a particular point in the system; most often at the die surface. Since we cannot set a target temperature for coupled thermal-electric simulation in the current version of ABAQUS and PID controlling system is also unavailable in this version of our software, we rather input a certain amount of current as the load in our model. In order to find the effect of higher setting temperature, we did the analysis by varying the input current. The study was done for three different input currents of 1000 A, 1100 A and to 1200 A for both the alumina and copper samples.

Fig. 3.50-3.55 show the temperature and current distributions in the sample, punch and die for three different input currents for both the alumina and copper samples. The melting temperature of copper is 1085° C, which was exceeded for 1200 A case. However, we still show the results here for comparing the temperatures in two systems. There was no noticeable change in the current or temperature distribution pattern with the increase of input current. As expected, the higher current resulted in higher temperature throughout the system. Higher current provides more heating energy and consequently higher temperature. The rise in temperature was more rapid in punch than any other part of the system (Fig. 3.54). There was also an increase in temperature difference between sample center and sample edge (Fig. 3.51) and also between sample center and die outer surface (Fig. 3.52) with the increase in input current.

As we have found an increase in temperature gradient with increase in input current, we have done simulation for a very high input current of 1800 A for the alumina sample and compared it with the results of 1000 A to see the variations. For 1800 A current input, a temperature gradient of 35° C was found in the axial direction which was less than 1° C for 1000 A input current (Fig. 3.56 (a)). The temperature difference between the sample center and sample edge rose up to 100° C for 1800 A (Fig. 3.56 (b)). Another interesting observation for this high

input current was the temperature difference between the sample center and die surface which became 420°C ; about 300°C higher than that for 1000 A current (Fig. 3.57 (a)). The punch temperature was also extremely high and the maximum temperature (2488°C) in the punch as well as in the system was found at the punch-spacer interface (Fig. 3.57 (b)). Fig. 3.58 and 3.59 show the change in temperature difference between sample center and edge, and between sample center and die outer surface respectively with change in input current for the alumina sample only. In both cases, as the input current increases, the temperature difference between the studied points increases non-linearly. For very high input current (in the case of high set temperature), this temperature gradient inside the sample will cause highly non-uniform property. At the same time, because of large temperature difference between the sample center and the die outer surface, SPS experiment controlled against a set temperature on die surface will be very inaccurate.

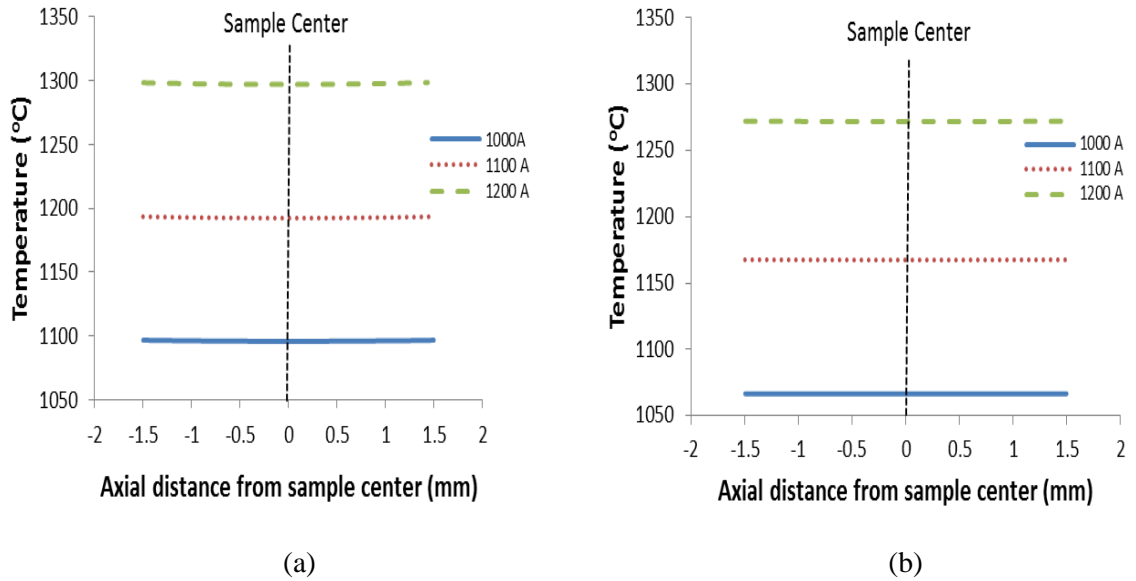
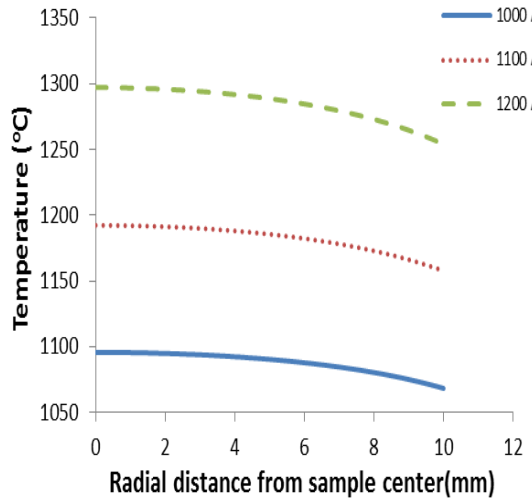
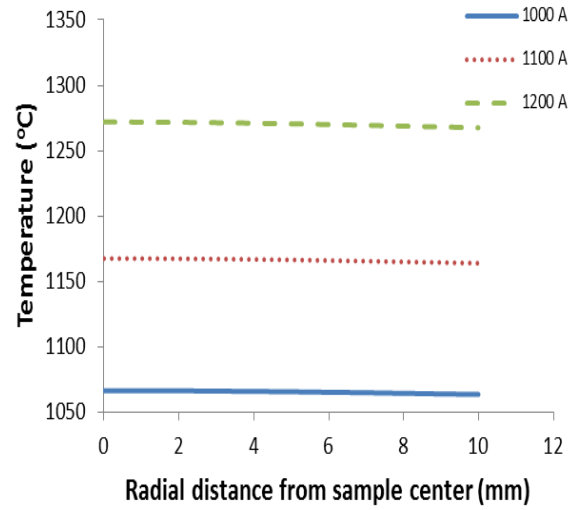


Fig. 3.50: Temperature distribution in axial direction in the sample as a function of input current:

(a) alumina and (b) copper



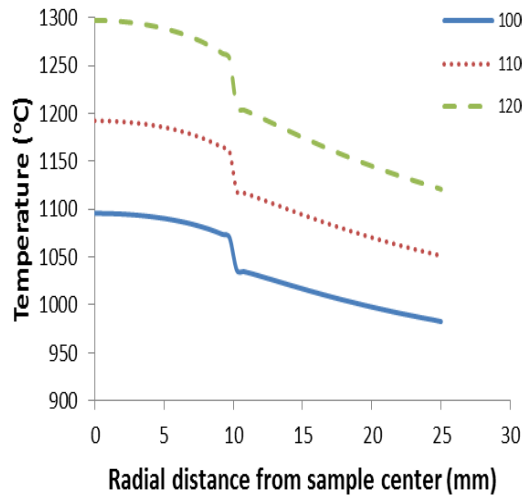
(a)



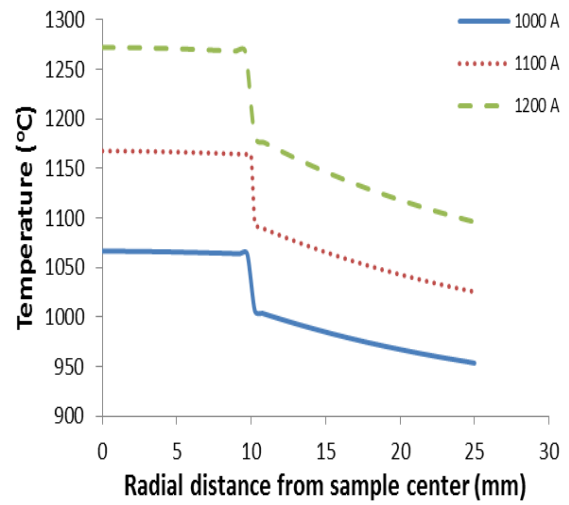
(b)

Fig. 3.51: Temperature distribution in radial direction in the sample as a function of input current:

(a) alumina and (b) copper



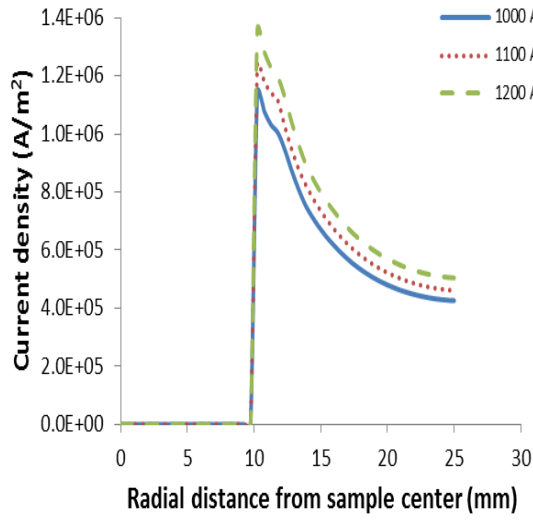
(a)



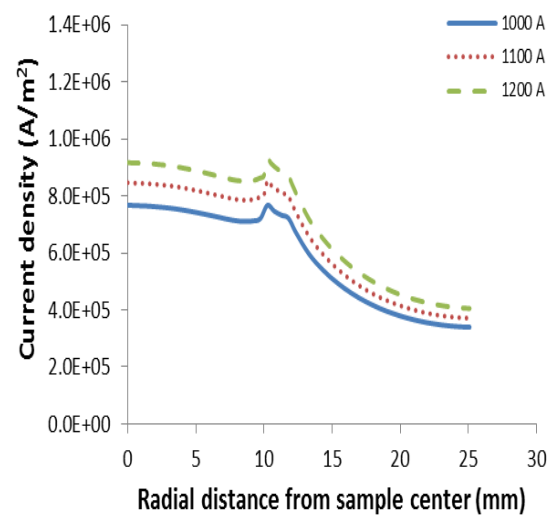
(b)

Fig. 3.52: Temperature distribution in sample-die as a function of input current: (a) alumina and

(b) copper

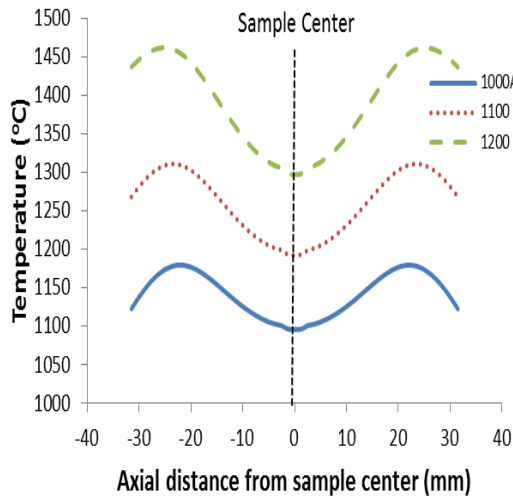


(a)

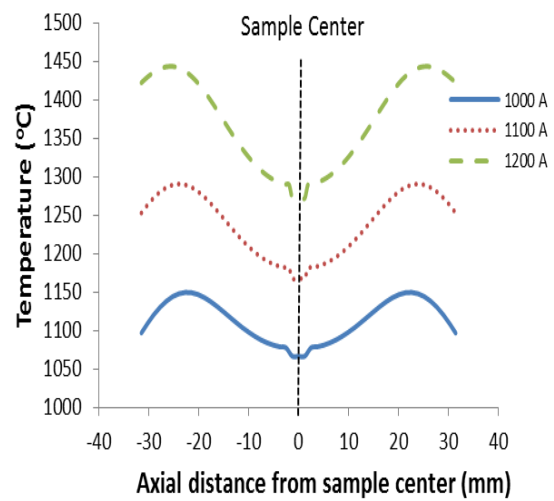


(b)

Fig. 3.53: Electric current density distribution in sample-die as a function of input current: (a) alumina and (b) copper



(a)



(b)

Fig. 3.54: Temperature distribution in punch-sample-punch as a function of input current: (a) alumina and (b) copper

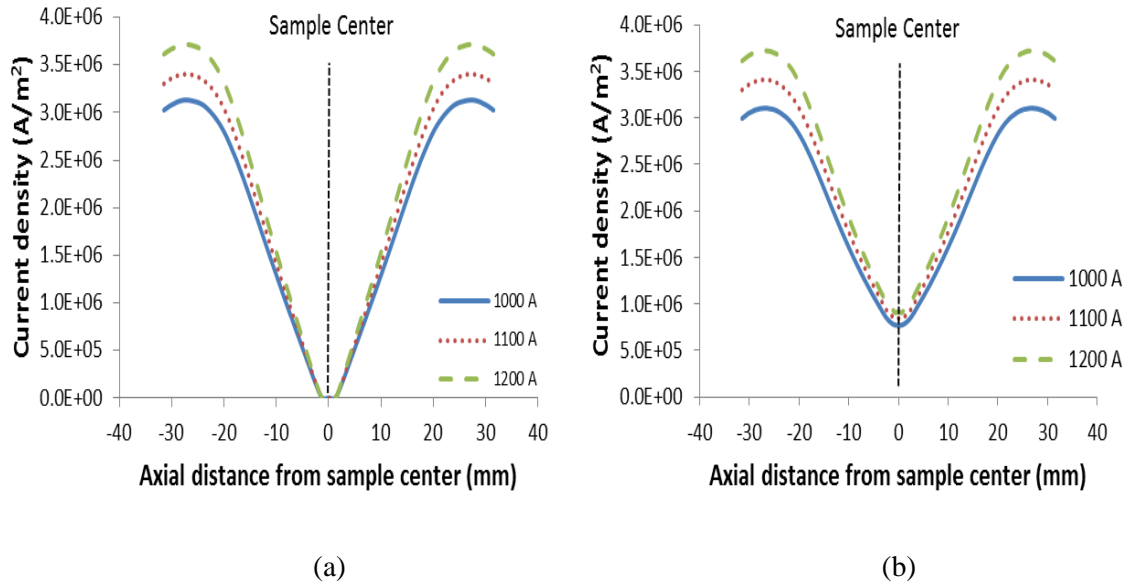


Fig. 3.55: Electric current density distribution in punch-sample-punch as a function of input current: (a) alumina and (b) copper

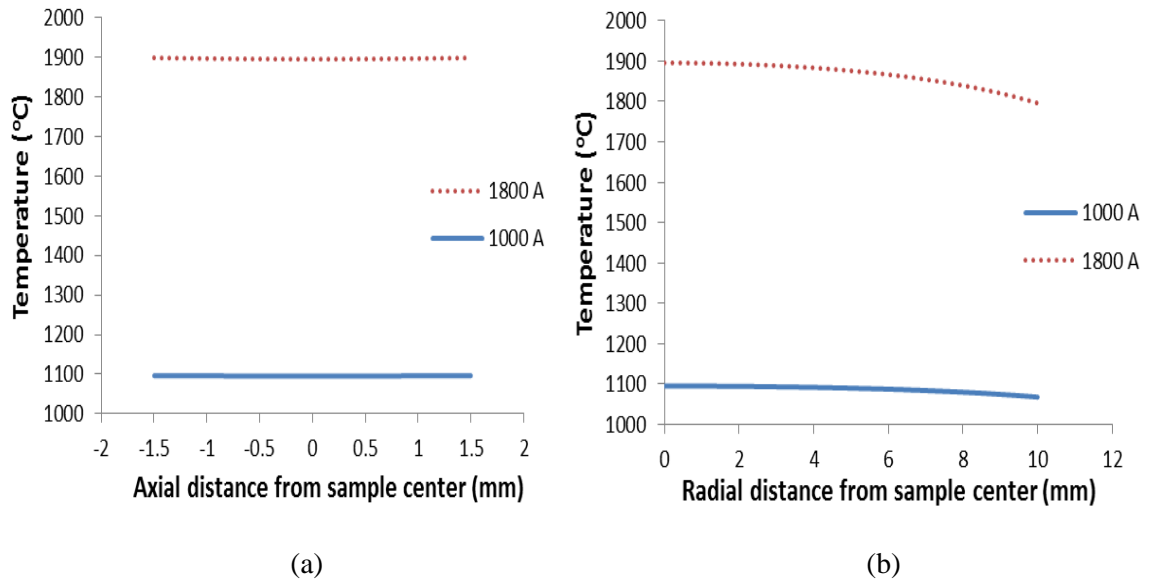


Fig. 3.56: Temperature distribution in the alumina sample as a function of input current (1000 A and 1800 A): (a) axial and (b) radial direction

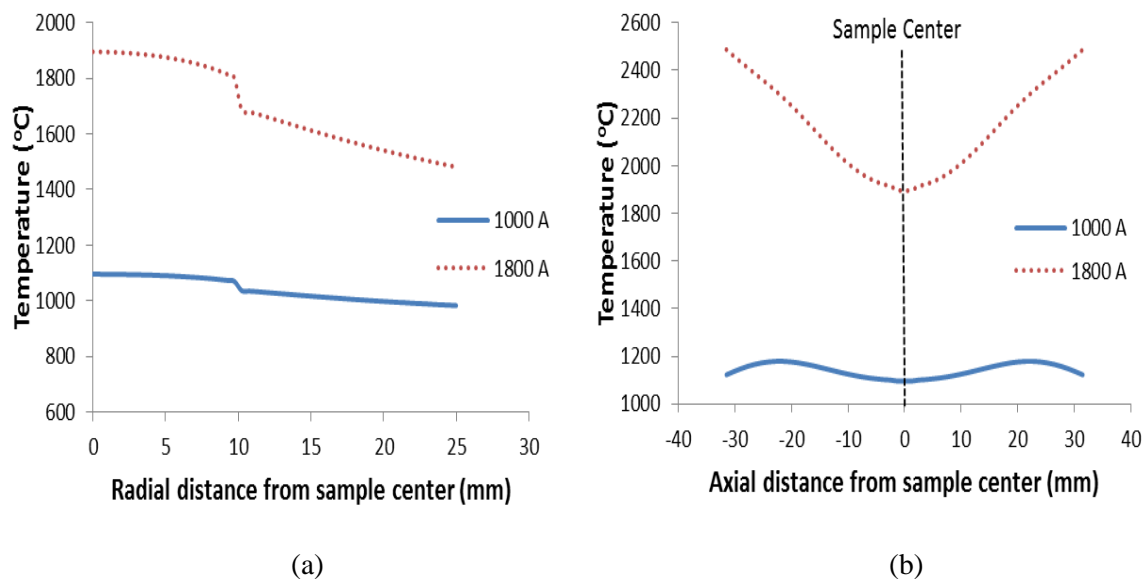


Fig. 3.57: Temperature distribution for the alumina sample as a function of input current (1000 A and 1800 A): (a) sample-die and (b) punch-sample-punch

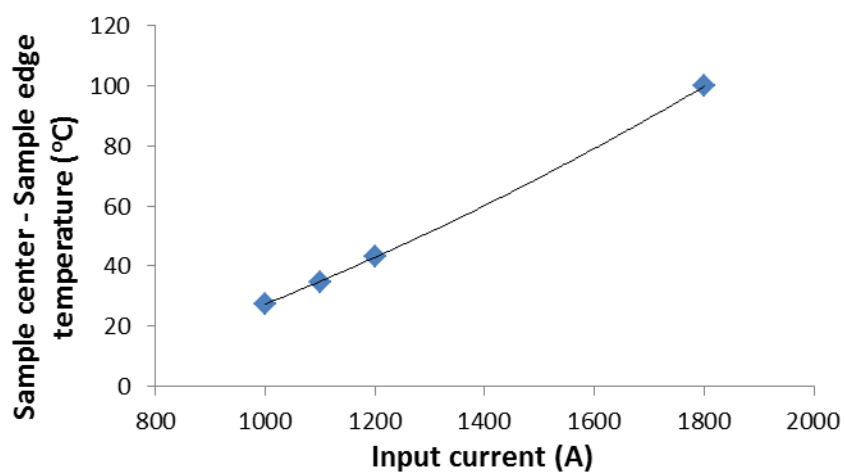


Fig. 3.58: Temperature difference between sample center and sample edge for different input currents

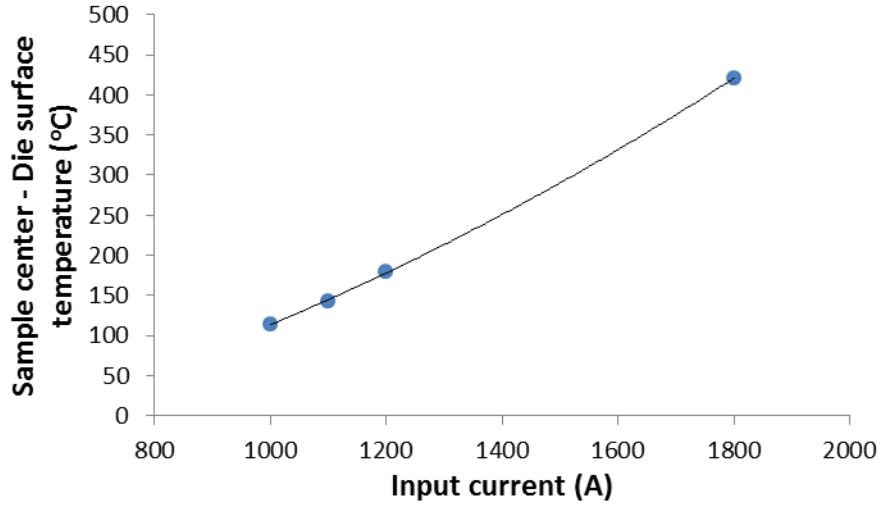


Fig. 3.59: Temperature difference between sample center and die outer surface for different input currents

3.3.9 Effect of using insulating layer around the die

It is a common practice amongst the SPS users to enclose the die outer surface with an insulating layer. Most often, graphite felt is used to make this insulation. It is thought that this insulation prevents radiation from the die outer surface and reduces temperature gradient inside the sample. To see the effect of this insulation, we did SPS simulation with slight modification in our model and then compared with our original model. In our already built model, we considered cavity radiation from all the exposed external surfaces in the system. We considered an emissivity coefficient of $\varepsilon = 0.8$ for that case. In our new configuration, we inhibited radiation from the external vertical die surfaces only. In order to do that, we considered an emissivity coefficient of $\varepsilon = 0$ on those surfaces. However, the remaining external surfaces in the configuration had unaltered radiation condition i.e. $\varepsilon = 0.8$. We did our analysis for both alumina and copper sample.

Fig. 3.60 shows the temperature contour plot of the whole without the thermal insulation for the alumina and copper samples. Comparing this figure with Fig. 2.35, we can see some notable differences. The difference was evident in case of both of the samples. Temperatures in punch, sample and die became more uniform as a result of using the insulating layer around the die. The maximum temperature in the system developed in the punch near the punch-sample interface, which was lower than the maximum temperature in the punch without the insulation. However, the average temperature in the die and sample increased due to the use of insulation. At the same time, the temperature gradients inside these parts reduced to some extent. The effect of the insulating layer can be more clearly understood by analyzing Fig. 3.61-3.66.

The axial and radial temperature gradients inside the alumina and copper sample with and without the thermal insulation are shown in Fig. 3.61 and 3.62. The maximum temperature in the alumina sample increased from 1096.58° C to 1162.13° C whereas for the copper it increased from 1066.5° C to 1101.98° C after preventing radiation by insulation. There was almost no temperature gradient in the axial direction for both the samples (Fig. 3.61). Even, the radial temperature gradient decreased significantly after using the insulation. The temperature difference between the alumina sample center and edge was 27° C, which reduced to 7° C after using the insulation around the die. Similarly, there was a reduction of the temperature gradient in the copper sample (Fig. 3.62). However, the effect of insulation on the temperature gradient in the copper sample was less evident as the sample already had low temperature gradient even without insulating layer.

Fig. 3.63 shows the temperature distribution in sample-die assembly for the alumina and copper samples respectively. Temperature at the die surface increased by 133° C and 81° C for the alumina and copper samples respectively for using the thermal insulation. However, the temperature difference between the sample center and the die outer surface decreased significantly. A temperature difference of around 112° C was found between the sample center

and the die outer surface for both the alumina and copper samples when no insulation was used. This temperature difference reduced to 46° C and 66° C for the alumina and copper samples respectively after using the insulation. Fig. 3.64 shows the current distribution in sample-die assembly for both the samples. There was no change in current distribution after using the insulation since neither the electrical properties nor the tool geometry changed due to the addition of insulating layer.

Fig. 3.65 shows the temperature distribution in the punch-sample-punch assembly with and without insulation. The maximum temperature in the punch decreased by 17° C and 43° C for alumina and copper sample respectively after using the insulation. The location of maximum temperature moved very close to the punch-sample interface. The temperature near the spacer was lower and it gradually increased up to punch-sample interface. Fig. 3.66 shows the current distribution in punch-sample-punch assembly, which did not show any difference in current distribution after using the insulation.

It is quite evident that the insulating layer around the die has a significant role in the temperature distribution in the whole system. Proper insulation can result in more uniform temperature distribution in the sample. However, it is not possible to prevent radiation from the external die surfaces completely in real SPS experiments. In order to insert the thermocouple inside the die, a hole is made in the graphite felt, which exposes some part of the die to radiation. Despite that partial radiation from the die, we assume that the insulation by graphite felt would still be effective in reducing temperature inhomogeneity in the sample; especially in non-conductive samples. One alternative could be doing the SPS experiment against the punch temperature so that whole die could be insulated.

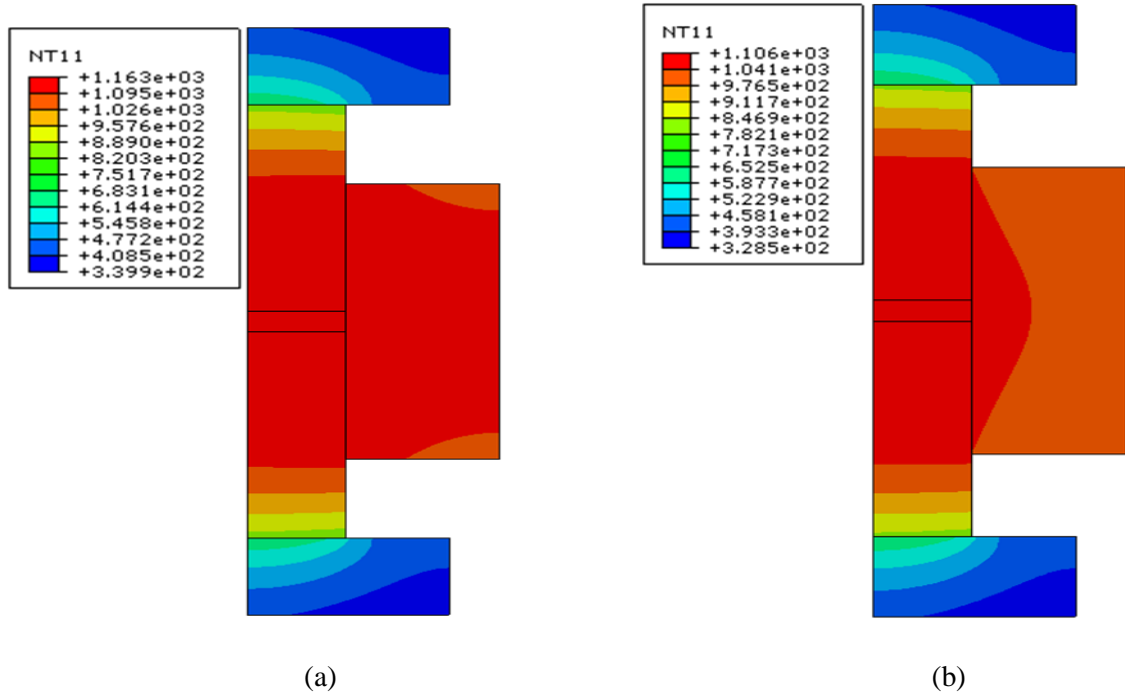


Fig. 3.60: Temperature contour plot in the whole SPS system with insulating layer around the die: (a) alumina and (b) copper

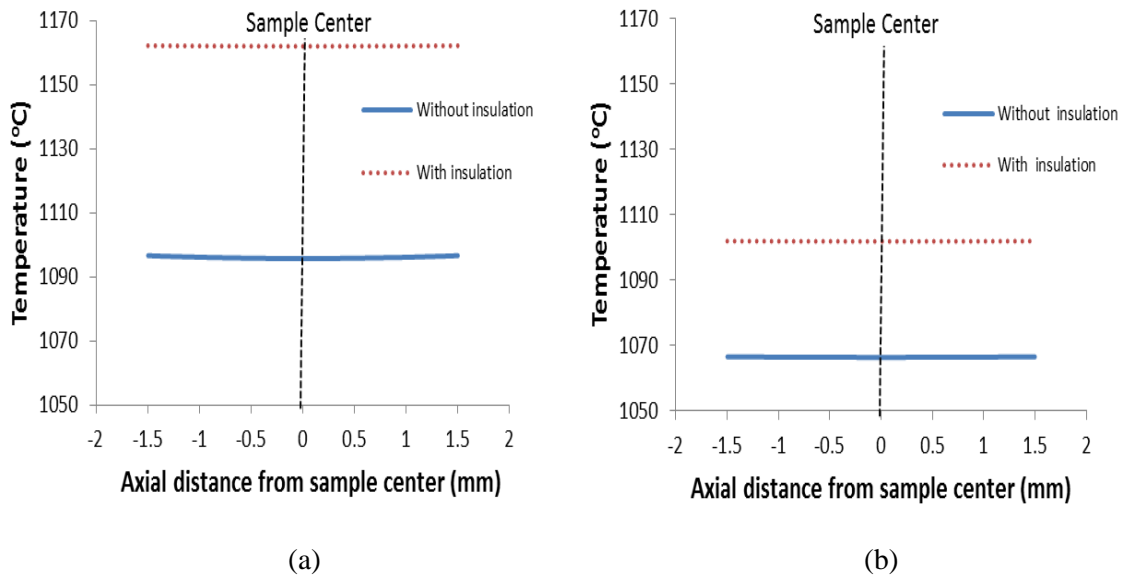
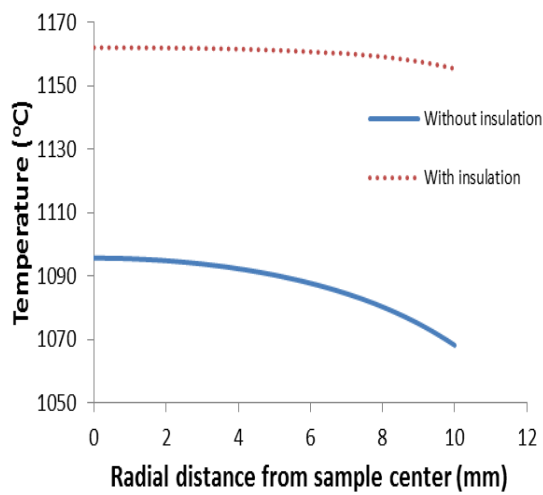
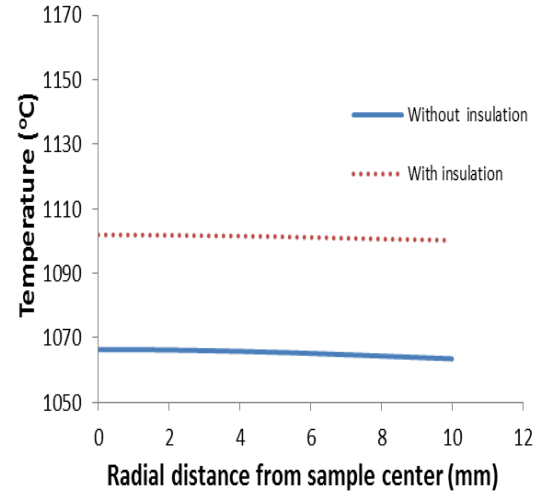


Fig. 3.61: Temperature distribution in the sample in axial direction with and without the insulating layer around the die: (a) alumina and (b) copper

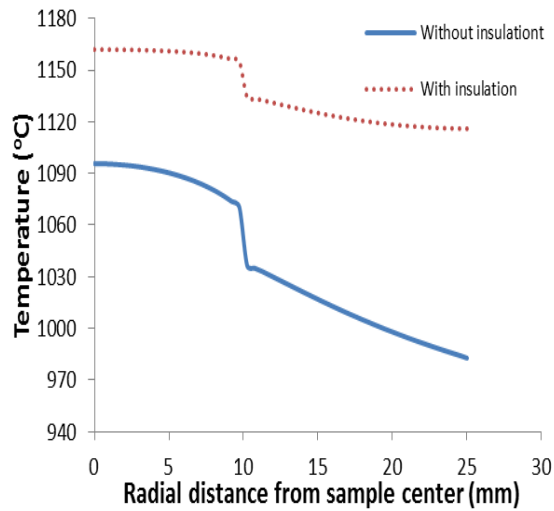


(a)

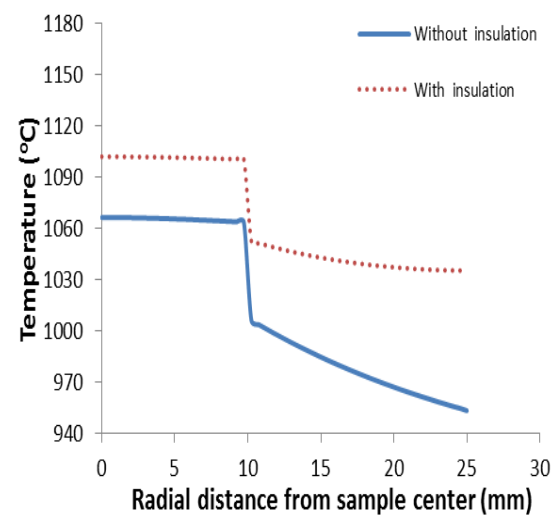


(b)

Fig. 3.62 Temperature distribution in the sample in radial direction with and without the insulating layer around the die: (a) alumina and (b) copper



(a)



(b)

Fig. 3.63: Temperature distribution in sample-die with and without insulating layer around the die: (a) alumina and (b) copper

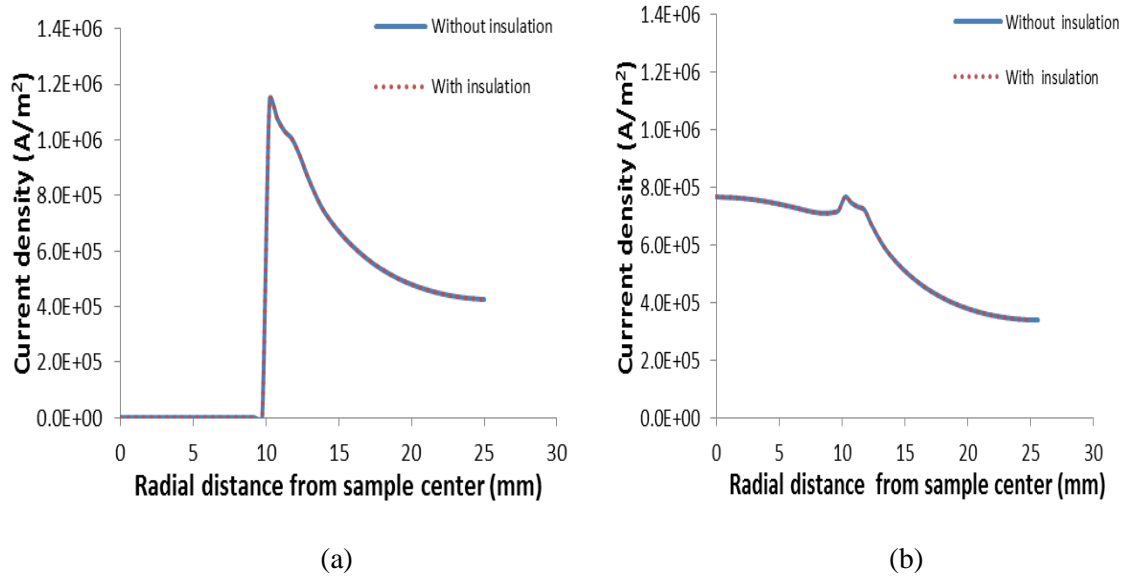


Fig. 3.64: Electric current density distribution in sample-die with and without the insulating layer around the die: (a) alumina and (b) copper

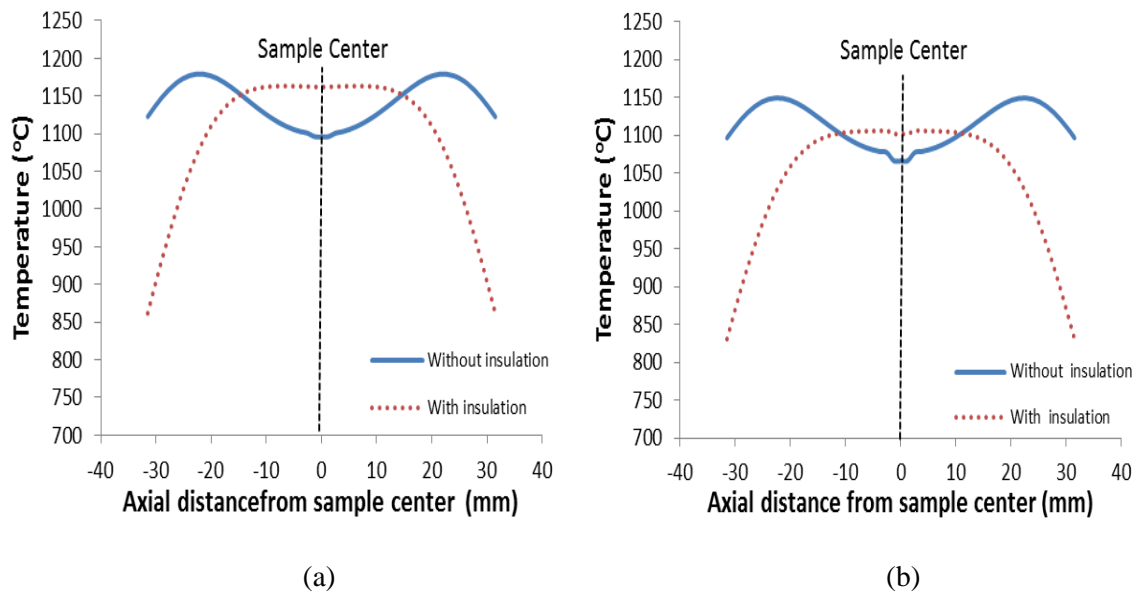


Fig. 3.65: Temperature distribution in punch-sample-punch with and without the insulating layer around the die: (a) alumina and (b) copper

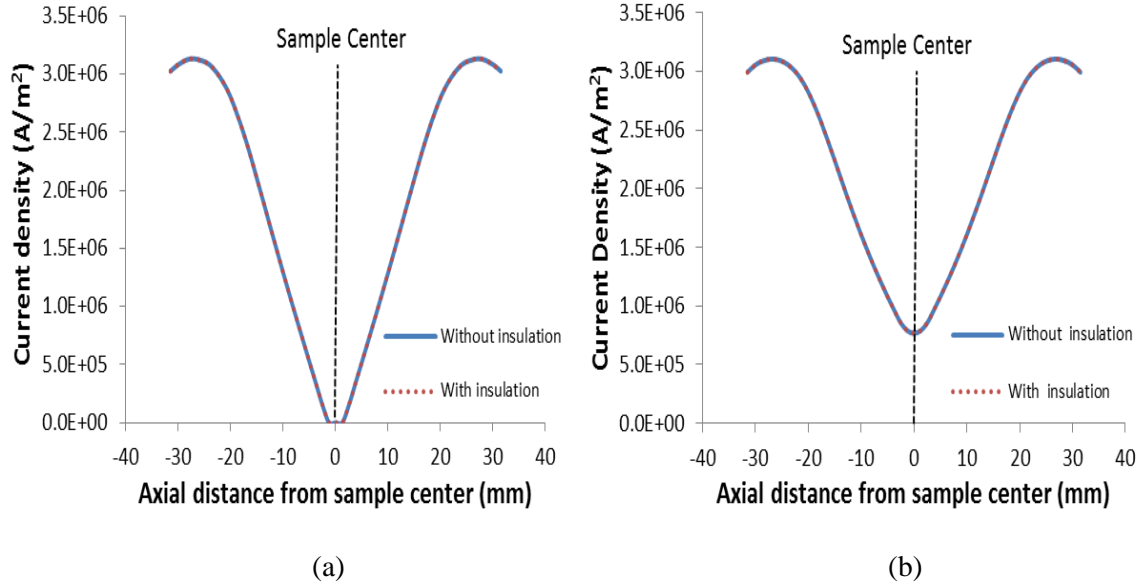


Fig. 3.66: Electric current density distribution in punch-sample-punch with and without the insulating layer around the die: (a) alumina and (b) copper

3.4 Conclusion

In this chapter, we utilized our coupled thermal-electrical model to study the importance of different process parameters on the temperature distribution inside the sintered sample. The importance of sample and tool geometry, punch and die position, input current and insulating layer around the die have been systematically analyzed. Some notable findings of this study are:

- The sample diameter can affect the temperature distribution to a great extent. Small diameter samples result in very high temperatures in the sample, die and punch. Temperature gradients are found inside the sample in both axial and radial directions. The punch temperature could be very high which could exceed the safe operating temperature of punch. On the other hand, large diameter samples have lower temperature and cause small temperature gradient in the system.

- With the increase in sample thickness, an axial temperature gradient is developed in the sample and overall temperature distribution in the sample becomes more non-uniform.
- The die dimensions play a very important role in temperature distributions. Both larger die thickness and die height reduce the temperature in sample. The temperature gradient inside the sample decreases with an increase in die height, but it increases with an increase in die thickness. Similarly, the temperature difference between sample center and die outer surface decreases with die height while it increases with die thickness.
- Although the punch length can alter the temperature distribution in the system, its effect is less than the effect of die dimension.
- The position of the punch-die is also important. If the die moves up or down from the center axis, it can result in non-uniform temperature distribution in sample and comparatively higher temperature in one of the punches.
- Both the punches should have the same length. Unequal punch length results in larger temperature gradient.
- Higher current (higher target temperature) produces higher temperature gradient in the sample. For high temperature sintering, the temperature difference between the sample center and the die outer surface could be very high.
- An insulating layer around the die can reduce the temperature gradient in the sample to some extent.
- All the process parameters studied here showed greater influence on the non-conductive alumina sample than the conductive copper sample.

CHAPTER IV

CONCLUSION

A fully coupled thermal-electric FEM model for SPS process was developed for detailed understanding of the temperature distribution and other underlying phenomena of the system for two different types of materials, non-conductive alumina and conductive copper. An integrated experimental-numerical methodology was implemented to determine the system contact resistances accurately. Series of experiments were also performed to validate the model. The FEM model showed good agreements with the experimental results. Temperature and current distributions as well as their evolution in the sample and other parts of the SPS setup were analyzed numerically with the help of our model. Some notable findings from the simulation results are the following:

- Temperature distribution in SPS system depends on the current distribution. In case of non-conducting alumina, no current flows through the sample and all the current is forced through the die. On the other hand, high density current flows through the copper sample for its high conductivity.
- The maximum temperature in the system is always generated in the punch. There is considerable temperature difference between the sample center and the die outer surface.

- Higher temperature is found in the alumina sample. The temperature gradient in the alumina sample is also quite large compared to the copper and this gradient can cause non-uniformity in sample microstructure and property.

The developed SPS model was utilized to study the importance of different process parameters on the temperature distribution inside the sintered sample. Important revelations of this parametric study are as following:

- The sample diameter can affect the temperature distribution to a great extent. Small diameter samples result in very high temperature in the sample, die and punch. Temperature gradient is found inside the sample in both axial and radial direction. The punch temperature could be very high which could exceed the safe operating temperature of punch. On the other hand, large diameter samples have lower temperature and cause small temperature gradient in the system.
- With the increase in sample thickness, axial temperature gradient is developed in the sample and overall temperature distribution in sample becomes non-uniform.
- The die dimensions play a very important role in temperature distribution. Both greater die thickness and die height reduce the temperature in the sample. The temperature gradient inside the sample decreases with an increase in die height, but it increases with an increase in die thickness. Similarly, the temperature difference between sample center and die outer surface decreases with die height while it increases with die thickness.
- Although the punch length can alter the temperature distribution in the system, its effect is less than the effect of die dimension.
- The position of the punch-die is also important. If the die moves up or down from the center axis, it can result in non-uniform temperature distribution in sample and comparatively higher temperature in one of the punches.

- Both the punches should have the same length. Unequal punch length results in larger temperature gradient.
- Higher current (higher target temperature) produces higher temperature gradient in the sample. For high temperature sintering, the temperature difference between sample center and die surface could be very high.
- An insulating layer around the die can reduce the temperature gradient in the sample to some extent.
- The process parameters have more significant effects on the temperature distributions in the non-conductive sample than the conductive one.

CHAPTER V

FUTURE WORK

- The developed SPS model could be utilized to find the most suitable combination of punch, die, and sample to achieve uniform temperature distribution inside the sample. In order to do that, many more simulations with different combinations have to be run to find the best match.
- In this research, we worked with the pure alumina and copper samples only. The model can be modified and utilized for other kind of materials such as composites. We have already modified our SPS model for predicting temperature distribution in amorphous-crystalline laminated composite. Further calibration and experimental analysis of this model is now under study.
- In our model, the densification of the sample was not considered; rather we modeled with a fully dense sample. Densification model can be incorporated in our already built model to improve its accuracy.
- Along with the temperature gradient, stress gradients are also developed in sintered samples. A coupled thermal-electrical-mechanical sintering model will be capable of showing the stress distribution in the sample. However, it was not possible to model the stress distribution in our model as the current ABAQUS version doesn't have the coupled thermal-electrical-mechanical FEM codes for axisymmetric model. ABAQUS only has

coupled thermal-electrical-mechanical codes for 3d model. However, the 3d coupled thermal-electrical-mechanical model elements get excessively distorted under the high load applied during sintering. Moreover, the ALE adaptive mesh refinement does not work for thermal-electrical –mechanical elements available in ABAQUS. Hence, it was not possible to predict the stress distribution accurately even with the 3d model in ABAQUS 6.12. However, COMSOL could be a good alternative for doing stress analysis in SPS system.

- In our model, we did simulation against some set input current unlike real sintering experiments, which are done against a set temperature on the die surface. The thermal-electric model in ABAQUS does not have any option for doing the sintering simulation against a set temperature. A Proportional-Integral-Derivative (PID) algorithm could be integrated in our model in order to do the simulation against some set temperature.

REFERENCES

- [1] A.C.D. Chaklader, J.A. Lund, Sintering '91: Proceedings of the Fifth International Symposium on the Science and Technology of Sintering, Held in Vancouver on July 23-26, 1991, Trans Tech Publications, Limited, 1992.
- [2] Z.A. Munir, U. Anselmi-Tamburini, M. Ohyanagi, Journal of Materials Science 41 (2006) 763-777.
- [3] F.V. Lenel, Materials and Corrosion 8 (1957) 51-51.
- [4] R.L. Coble, Journal of the American Ceramic Society 41 (1958) 55-62.
- [5] R. German, Z. Munir, Metallurgical and Materials Transactions A 6 (1975) 2229-2234.
- [6] R. Orrù, R. Licheri, A.M. Locci, A. Cincotti, G. Cao, Materials Science and Engineering: R: Reports 63 (2009) 127-287.
- [7] Z.A. Munir, D.V. Quach, M. Ohyanagi, Journal of the American Ceramic Society 94 (2011) 1-19.
- [8] M. Tokita, Mechanism of spark plasma sintering, Proceeding of NEDO International symposium, 1999.
- [9] J.E. Garay, Current-Activated, Pressure-Assisted Densification of Materials, vol 40, 2010, pp. 12.11-12.24.
- [10] A.K. Singh, Spark plasma sintering of iron based amorphous alloys, composites, and coating, 2012.
- [11] S.P. Harimkar, T. Borkar, A. Singh, Materials Science and Engineering: A 528 (2011) 1901-1905.
- [12] J.H. H. U. Kessel, R. Kirchner, T. Kessel, FCT Systeme GmbH.
- [13] Spark Plasma Sintering, Thermal Technology LLC (Santa Rosa, CA, USA).
- [14] D.S. Perera, M. Tokita, S. Moricca, Journal of the European Ceramic Society 18 (1998) 401-404.

- [15] I.K. N. Tamari, T. Tanaka, M. Kawahara, M. Tokita, Y. Makino, S.Miyake, Journal of the Japan Society of Powder and Powder Metallurgy 46 (1999) 816-819.
- [16] T.T. N. Tamari, K. Tanaka, I. Kondoh, M. Kawahara, M. Tokita, Journal of the Ceramic Society of Japan 103 (1995) 740-742.
- [17] L. Gao, J.S. Hong, H. Miyamoto, S.D.D.L. Torre, Journal of the European Ceramic Society 20 (2000) 2149-2152.
- [18] L. Gao, Z. Shen, H. Miyamoto, M. Nygren, Journal of the American Ceramic Society 82 (1999) 1061-1063.
- [19] S.H. Risbud, J.R. Groza, M.J. Kim, Philosophical Magazine Part B 69 (1994) 525-533.
- [20] X.J. Chen, K.A. Khor, S.H. Chan, L.G. Yu, Materials Science and Engineering: A 374 (2004) 64-71.
- [21] K.R. Anderson, J.R. Groza, M. Fendorf, C.J. Echer, Materials Science and Engineering: A 270 (1999) 278-282.
- [22] G. Xie, O. Ohashi, N. Yamaguchi, A. Wang, Metallurgical and Materials Transactions A 34 (2003) 2655-2661.
- [23] D. Kusano, Y. Hori, Effects of PbTe Doping on the Thermoelectric Properties of $(\text{Bi}_2\text{Te}_3)_{0.2}(\text{Sb}_2\text{Te}_3)_{0.8}$, 21st International Conference on Thermoelectronics, Japan, 2002, pp. 13-16.
- [24] L.Y. Zhang M. , Euro. Patent No. EP1820224 (2006).
- [25] F.K. Konishi A. , US Patent No. 6,222,242 (2001).
- [26] B.E. Takeuchi T., Tabuchi M., Kageyama H., Kobayashi Y., Coats A., Morrison F., Sinclair D.C., West A.R., Journal of Materials Science 34 (1999) 917-924.
- [27] M.K. Zhan G., Kuntz D., Wan J., 2005 World Intellectual Property Publ. No. WO2005003036.
- [28] T.J. Shimada S. , JP Patent No. JP2000302545 (2000).

- [29] T.J. Shimada S. , JP Patent No. JP2000302546 (2006).
- [30] M. Yue, J. Zhang, Y. Xiao, G. Wang, T. Li, Magnetics, IEEE Transactions on 39 (2003) 3551-3553.
- [31] M.A. Fujita K., Inoue A., US Patent No. 6,172,589 (2001).
- [32] M.Y. Moro H. , US Patent No. 5,227,235 (1993).
- [33] K.H. Yoshida S., Mizushima T., Ikarashi K. ,Naito Y., US Patent No. 6,897,718 (2003).
- [34] K.J.D.a.M.A.K. Hulbert D M, US Patent No. 2007/0132154 (2007).
- [35] Z. Shen, H. Peng, M. Nygren, Advanced Materials 15 (2003) 1006-1009.
- [36] W.G.P. Seth B. B., Swartzbeck G. W., US Patent No. 6,384,365 (2002).
- [37] G.F. Taylor, Apparatus for Making Hard Metal Compositions, 1933.
- [38] G.F. Taylor, US Patent No. 1,896,854 (1933).
- [39] G.D. Cremer, Sintering together powder metals such as Bronze, Brass or Aluminium 1944.
- [40] K. Inoue, Electric Discharge Heat Treatment of Metals in Electrolytes, 1965.
- [41] K. Inoue, US Patent, No. 3,241,956 (1966).
- [42] K. Inoue, Electric Discharge Sintering, 1966.
- [43] S. Clyens, S.T.S. Al-Hassani, W. Johnson, International Journal of Mechanical Sciences 18 (1976) 37-40.
- [44] B.G.L. Raichenko A.I., Leshchinsky V.I., Physics sinter 5 (1976) 215-225.
- [45] Y.U.S.K. Y.A.E. Geguzin, A.A. Onoprienko, F.N. Zung, Sov. Phys. Solid State 17 (1975) 457-458.
- [46] O. Yanagisawa, T. Hatayam, and K. Matsugi, Materials Japan 33 (1994) 1489-1496.
- [47] M. Tokita, Journal of Japan society of powder and powder metallurgy 30 (1993) 790-804.

- [48] P. Lee, Y. Trudel, R. Iacocca, R. German, B. Ferguson, W. Eisen, K. Moyer, (1998).
- [49] M. Sukanuma, Y. Kitagawa, S. Wada, N. Murayama, *Journal of the American Ceramic Society* 86 (2003) 387-394.
- [50] J.A. Schneider, A.K. Mukherjee, K. Yamazaki, K. Shoda, *Materials Letters* 25 (1995) 101-104.
- [51] T.S. Srivatsan, B.G. Ravi, M. Petraroli, T.S. Sudarshan, *International Journal of Refractory Metals and Hard Materials* 20 (2002) 181-186.
- [52] D. Salamon, Z. Shen, *Materials Science and Engineering: A* 475 (2008) 105-107.
- [53] R.M. German, *Sintering Theory and Practice*, Wiley, 1996, p. 482.
- [54] L.A. Stanciu, V.Y. Kodash, J.R. Groza, *Metallurgical and Materials Transactions A* 32 (2001) 2633-2638.
- [55] Z. Shen, M. Johnsson, Z. Zhao, M. Nygren, *Journal of the American Ceramic Society* 85 (2002) 1921-1927.
- [56] C.L. Wang, L. Chen, T. Hirai, *Journal of Materials Research* 15 (2000) 982-987.
- [57] Y. Zhou, K. Hirao, Y. Yamauchi, S. Kanzaki, *Journal of the European Ceramic Society* 24 (2004) 3465-3470.
- [58] U. Anselmi-Tamburini, J. Garay, Z. Munir, A. Tacca, F. Maglia, G. Spinolo, *Journal of materials research* 19 (2004) 3255-3262.
- [59] W.-M. Guo, J. Vleugels, G.-J. Zhang, P.-L. Wang, O. Van der Biest, *Scripta Materialia* 62 (2010) 802-805.
- [60] G.G. Apak B., F.C. Sahin, Yosel O. , The effect of heating rate on the Magnesia doped alumina prepared by SPS, *Mechanical Properties and Performance of Engineering Ceramics and Composites V: Ceramic Engineering and Science Proceedings*, vol 31, 2010, pp. 3-7.
- [61] D.J. Chen, M.J. Mayo, *Journal of the American Ceramic Society* 79 (1996) 906-912.
- [62] Y.C. Wang, Z.Y. Fu, Q.J. Zhang, *Key Engineering Materials* 717-720.
- [63] D. Zhang, L. Zhang, J. Guo, W.-H. Tuan, *Journal of the American Ceramic Society* 89 (2006) 680-683.

- [64] W. Yu-cheng, F. Zheng-yi, W. Wei-ming, Z. Han-xiong, Journal of Wuhan University of Technology-Mater. Sci. Ed. 17 (2002) 19-21.
- [65] S.W. Wang, L.D. Chen, T. Hirai, Y.S. Kang, Journal of Materials Science Letters 18 (1999) 1119-1121.
- [66] U. Anselmi-Tamburini, J.E. Garay, Z.A. Munir, Scripta Materialia 54 (2006) 823-828.
- [67] O.O. Xie G., Yoshioka T., Song M., Mitsuishi K., Materials Transactions 42 (2001) 1846-1849.
- [68] S.Z. Chaim R, Nygren M., Journal of Materials Research 19 (2004) 2527-2531.
- [69] G. Skandan, H. Hahn, B.H. Kear, M. Roddy, W.R. Cannon, Materials Letters 20 (1994) 305-309.
- [70] A.I. Raichenko, Metalurgiya, Russia (1987).
- [71] G. Xie, O. Ohashi, K. Chiba, N. Yamaguchi, M. Song, K. Furuya, T. Noda, Materials Science and Engineering: A 359 (2003) 384-390.
- [72] W. Chen, U. Anselmi-Tamburini, J.E. Garay, J.R. Groza, Z.A. Munir, Materials Science and Engineering: A 394 (2005) 132-138.
- [73] U. Anselmi-Tamburini, J.E. Garay, Z.A. Munir, Materials Science and Engineering: A 407 (2005) 24-30.
- [74] H. Conrad, Materials Science and Engineering: A 322 (2002) 100-107.
- [75] T. Nagae, M. Yokota, M. Nose, S. Tomida, T. Kamiya, S. Saji, Materials Transactions 43 (2002) 1390-1397.
- [76] D.M. Hulbert, A. Anders, D.V. Dudina, J. Andersson, D. Jiang, C. Unuvar, U. Anselmi-Tamburini, E.J. Lavernia, A.K. Mukherjee, Journal of Applied Physics 104 (2008) 033305/1-7.
- [77] D.M. Hulbert, A. Anders, J. Andersson, E.J. Lavernia, A.K. Mukherjee, Scripta Materialia 60 (2009) 835-838.
- [78] H. Tomino, H. Watanabe, Y. Kondo, Journal of the Japan Society of Powder and Powder Metallurgy 44 (1997) 974-979.
- [79] O.J. Groza J., Field Effects in WC-Co Sintering, Advances in Powder Metallurgy and Particulate Materials, APMI International , Princeton, NJ, 1997, pp. 12.51-12.60.

- [80] K.K. K. Ozaki K., Nishio T. , Matsumoto A. , Suyiyama A., Journal of the Japan Society of Powder and Powder Metallurgy 47 (2000) 293-297.
- [81] A.I. Raichenko, E.S. Chernikova, Soviet Powder Metallurgy and Metal Ceramics 28 (1989) 517-519.
- [82] I.T. Yoneya M., Materials Transactions 42 (2001) 2165-2171.
- [83] W. Yucheng, F. Zhengyi, Materials Science and Engineering: B 90 (2002) 34-37.
- [84] K.Y.T. Jeon J. H., Auh K.H., Journal of Ceramic Processing Research 8 (2002) 195-200.
- [85] M.S. Mori K., Maeda K.,Osakada K., Simulation of Materials Processing: Theory, Methods and Applications, Balkema, Rotterdam,Netherlands, A.A. Balkema publishers, Old Post Road, Brookfield, VT 05036, USA, 1998, 517-522.
- [86] C.F.C. Fessler R.R. Fessler, B.D. Merkle B.D., Borton J.M., Goldberger W.M., Modeling the electroconsolidation® process,, International Conference on Powder Metallurgy and Particulate Materials, New York, May 30-June 3, 2000, pp. 1.129-121.138.
- [87] E.M. Heian, A. Feng, Z.A. Munir, Acta Materialia 50 (2002) 3331-3346.
- [88] K. Matsugi, H. Kuramoto, O. Yanagisawa, M. Kiritani, Materials Science and Engineering: A 354 (2003) 234-242.
- [89] K.H. Matsugi K., Hatayama T., Yanagisawa O., Journal of Materials Processing Technology 134 (2003) 225-232.
- [90] K. Matsugi, H. Kuramoto, T. Hatayama, O. Yanagisawa, Journal of Materials Processing Technology 146 (2004) 274-281.
- [91] J. Zhang, Numerical simulation of thermoelectric phenomena in field activated sintering, Department of Materials Science and Engineering. , Drexel University, 2004.
- [92] A. Zavaliangos, J. Zhang, M. Krammer, J.R. Groza, Materials Science and Engineering: A 379 (2004) 218-228.
- [93] K. Vanmeensel, A. Laptev, J. Hennicke, J. Vleugels, O. Van der Biest, Acta Materialia 53 (2005) 4379-4388.
- [94] W. Yucheng, F. Zhengyi, W. Weimin, Z. Jinyong, Journal of Wuhan University of Technology-Mater. Sci. Ed. 21 (2006) 126-128.

- [95] U. Anselmi-Tamburini, S. Gennari, J.E. Garay, Z.A. Munir, *Materials Science and Engineering: A* 394 (2005) 139-148.
- [96] E. Olevsky, L. Froyen, *Scripta Materialia* 55 (2006) 1175-1178.
- [97] B. McWilliams, *Numerical Simulation of Electric Field Assisted Sintering*, Drexel University, 2008.
- [98] A. Zavaliangos, B. McWilliams, Kyu C., R. J. Dowding, *JOM* 58 (2006) 67-71.
- [99] B. McWilliams, A. Zavaliangos, *Journal of Materials Science* 43 (2008) 5031-5035.
- [100] J. Räthel, M. Herrmann, W. Beckert, *Journal of the European Ceramic Society* 29 (2009) 1419-1425.
- [101] Z.D. Cai Y., Zhao X., Chen L., Jiang W., Zha P., *Materials Transactions* 50 (2009) 782-790.
- [102] J. Luo, Y. Sun, C. Zhang, Z. Zhao, *Journal of Wuhan University of Technology-Mater. Sci. Ed.* 27 (2012) 1120-1124.
- [103] D.L. Molenat G., Galy J., Couret A., *Journal of Metallurgy* 2010 (2010).
- [104] L.J. Cura M., Ritasalo R. , Syren J. , Lotta J., Soderberg O. , Ritvonen T. , Turunen E. , Hannula S., *Estonian Journal of Engineering* 15 (2009) 255-265.
- [105] D. Tiwari, B. Basu, K. Biswas, *Ceramics International* 35 (2009) 699-708.
- [106] A. Cincotti, A.M. Locci, R. Orrù, G. Cao, *AIChE Journal* 53 (2007) 703-719.
- [107] G. Maizza, S. Grasso, Y. Sakka, T. Noda, O. Ohashi, *Science and Technology of Advanced Materials* 8 (2007) 644-654.
- [108] G. Maizza, S. Grasso, Y. Sakka, *Journal of Materials Science* 44 (2009) 1219-1236.
- [109] X. Wang, S.R. Casolco, G. Xu, J.E. Garay, *Acta Materialia* 55 (2007) 3611-3622.
- [110] G.M. Guy Antou, Gilles Trolliard, and Alexandre Maitrea, *Journal of Materials Research* 24 (2009) 16.
- [111] C. Wang, L. Cheng, Z. Zhao, *Computational Materials Science* 49 (2010) 351-362.

- [112] Y. Song, Y. Li, Z. Zhou, Y. Lai, Y. Ye, *Journal of Materials Science* 46 (2011) 5645-5656.
- [113] E.A. Olevsky, C. Garcia-Cardona, W.L. Bradbury, C.D. Haines, D.G. Martin, D. Kapoor, *Journal of the American Ceramic Society* 95 (2012) 2414-2422.
- [114] S. Muñoz, U. Anselmi-Tamburini, *The International Journal of Advanced Manufacturing Technology* 65 (2013) 127-140.
- [115] D. Giuntini, E. Olevsky, C. Garcia-Cardona, A. Maximenko, M. Yurlova, C. Haines, D. Martin, D. Kapoor, *Materials* 6 (2013) 2612-2632.
- [116] S. Muñoz, U. Anselmi-Tamburini, *Journal of Materials Science* 45 (2010) 6528-6539.
- [117] S.S. Babu, M.L. Santella, Z. Feng, B.W. Riemer, J.W. Cohron, *Science and Technology of Welding & Joining* 6 (2001) 126-132.
- [118] H. R., *Electric Contacts : Theory and Applications*, Springer, New York, 1967.
- [119] S.Y. Grasso S., Maizza G., *Materials Transactions* 50 (2009) 2111-2114.
- [120] Inframat, alpha-Aluminium Oxide Data Sheet, Inframat @ Advanced Materials.

APPENDIX

Properties of graphite

$$\rho = 1850 \text{ Kg m}^{-3}$$

$$K = 65 - 0.0017 T \text{ (W m}^{-1} \text{ K}^{-1}\text{)}$$

$$R = (26 - 3 \times 10^{-2} T + 2 \times 10^{-5} T^2 - 6.4 \times 10^{-9} T^3 + 7.8 \times 10^{-13} T^4) 10^{-6} (\Omega \text{ m})$$

$$C_p = 310.5 + 1.7 T \text{ (J Kg}^{-1} \text{ K}^{-1}\text{)}$$

Properties of alumina

$$\rho = 3970 \text{ Kg m}^{-3}$$

$$K = 76.4488 - 0.18978 T + 1.9596 \times 10^{-4} T^2 - 8.9466 \times 10^{-8} T^3 + 1.4909 \times 10^{-11} T^4 \text{ (W m}^{-1} \text{ K}^{-1}\text{)}$$

$$R = 10^8 (\Omega \text{ m})$$

$$C_p = -126.5317 + 8.1918 T - 6.1058 \times 10^{-3} T^2 + 2.3104 \times 10^{-6} T^3 - 3.4204 \times 10^{-10} T^4 \text{ (J Kg}^{-1} \text{ K}^{-1}\text{)}$$

Properties of copper

$$\rho = 8960 \text{ Kg m}^{-3}$$

$$K = 420.66 - 0.07 T \text{ (W m}^{-1} \text{ K}^{-1}\text{)}$$

$$R = (-3.44 + 70.9 \times 10^{-3} T - 9.6 \times 10^{-6} T^2 + 9.77 \times 10^{-9} T^3) \times 10^{-9} (\Omega \text{ m})$$

$$C_p = 355.3 + 0.1 T \text{ (J Kg}^{-1} \text{ K}^{-1}\text{)}$$

where ρ = Density, K = Thermal conductivity, R = Resistivity, C_p = Specific Heat [109,111,116]

VITA

Redwan Jahid Chowdhury

Candidate for the Degree of

Master of Science

Thesis: NUMERICAL STUDY OF THE PROCESS PARAMETERS IN SPARK
PLASMA SINTERING (SPS)

Major Field: Mechanical and Aerospace Engineering

Biographical:

Education:

Completed the requirements for the Master of Science in Mechanical and Aerospace Engineering at Oklahoma State University, Stillwater, Oklahoma in December, 2013.

Completed the requirements for the Bachelor of Science in Mechanical Engineering at Bangladesh University of Science and Technology (BUET), Dhaka, Bangladesh in 2011.

Experience:

- 1 year and six months of working experience on numerical simulation and material processing by Spark plasma sintering
- Over two years of experience of working as Graduate Teaching Assistant for Material Science and Measurement and Instrumentation courses in OSU.
- Six months of working experience as a tutor for Mathematics and Physics in OSU.